Title

Modeling the evolution of coupled ice flow dynamics and subglacial hydrology for Petermann Glacier, Northern Greenland, on seasonal, inter-annual, and centennial time-scales

Author

Ehrenfeucht, Shivani

Publication Date

2023

Peer reviewed|Thesis/dissertation

UNIVERSITY OF CALIFORNIA,
IRVINE

Modeling the evolution of coupled ice flow dynamics and subglacial hydrology for Petermann Glacier, Northern Greenland, on seasonal, inter-annual, and centennial time-scales

DISSERTATION

submitted in partial satisfaction of the requirements
for the degree of

DOCTOR OF PHILOSOPHY

in Earth System Science

by

Shivani Ehrenfeucht

Dissertation Committee:
Professor Eric Rignot, Chair
Professor Mathieu Morlighem
Professor Francois Primeau

2023

DEDICATION

To my friends and family.

TABLE OF CONTENTS

LIST OF FIGURES

LIST OF TABLES

ACKNOWLEDGMENTS

I would like to extend my heartfelt gratitude to my PhD advisors, Dr. Mathieu Morlighem and Dr. Eric Rignot, for their continued support throughout this process. Their invaluable expertise, mentorship, and guidance have been instrumental in shaping my growth as a researcher. I am profoundly grateful for the opportunity to have worked with such remarkable scientists. I am especially grateful to Mathieu for continuing to work with and mentor me despite his move to Dartmouth College. His dedication and commitment to my success are deeply appreciated.

I would like to thank the third member of my thesis committee, Dr. Francois Primeau for his valuable advice, feedback, and thought provoking conversations.

My sincere appreciation goes to my co-authors, Dr. Christine Dow and Dr. Jeremie Mouginot, whose expertise and guidance was irreplaceable, particularly during the early stages of my research. The work presented here would not have been possible without your guidance.

I am grateful to the past and present members of both of my research groups for their friendship and support. In particular, I would like to thank Dr. Tyler Pelle, Dr. Emily Kane, and Dr. Youngmin Choi, all of whom have continued to answer an excessive number of questions and repeatedly offer their assistance years after moving on to new positions.

Special thanks to Dr. Bernd Scheuchl for his endless support, encouragement, and willingness to lend a listening ear on matters of science and beyond.

This work took place at the University of California, Irvine, with financial support from the National Aeronautics and Space Administration (NASA) Future Investigators in NASA Earth and Space Science and Technology (FINESST) program (no. 80NSSC20K1618), which supports graduate student-designed and performed research projects.

Chapter 2 and Appendix A are reprinted with permission from the American Geophysical Union (*Geophysical Research Letters*).

Shivani Ehrenfeucht

Vita

EDUCATION

University of Colorado **Boulder, Colorado**
B.A. in Environmental Studies; B.A. in Mathematics *September 2009 - May 2014*

Boston University **Boston, Massachusetts**
M.A. in Earth Science *September 2016 - July 2018*

University of California- Irvine **Irvine, California**
M.S. in Earth System Science *August 2018 - December 2020*

University of California- Irvine **Irvine, California**
Ph.D. in Earth System Science *December 2020 - Present*

PUBLICATIONS and PRESENTATIONS

S. Ehrenfeucht, M. Morlighem, E. Rignot, C. Dow, and J. Mouginot. Seasonal acceleration of Petermann Glacier, Greenland, from changes in subglacial hydrology. *Geophysical Research Letters*. 2023. 50(1), p.e2022GL098009.

H. Chen, E. Rignot, B. Scheuchl, **S. Ehrenfeucht**. Grounding Zone of Amery Ice Shelf, Antarctica, from Differential Radar Interferometry. *Geophysical Research Letters*. 2023. 50(6): e2022GL102430.

S. Ehrenfeucht, M. Morlighem, E. Rignot, C. Dow. Fully-coupled modeling of ice flow and subglacial hydrology applied to the future projections for a northern Greenlandic glacier. *2022 AGU Fall Meeting*. Chicago, IL, 12-16 Dec.

S. Ehrenfeucht, M. Morlighem, E. Rignot, C. Dow, and J. Mouginot. Seasonal acceleration of Petermann Glacier modeled from subglacial hydrology. *2021 AGU Fall Meeting*. New Orleans, LA, 13-17 Dec.

S. Ehrenfeucht, M. Morlightem, E. Rigot, C. Dow, P. Milillo, and J. Mouginot. Seasonal dynamics of Petermann Glacier, Greenland. *2020 AGU Fall Meeting*. Online, 1-17 Dec.

J. Mouginot, E. Rignot, B. Scheuchl, M. Romain, B. Anders, **S. Ehrenfeucht**, and A. Derkacheva. Ice-shelf and glacier changes in Northern Greenland. *2020 EGU General Assembly*. Online, 4-8 May.

S. Ehrenfeucht, M. Morlighem, E. Rignot, and J. Mouginot. Seasonal dynamics of North Greenland ice shelves. *2019 AGU Fall Meeting*. San Francisco, CA, 9-13 Dec.

S. Ehrenfeucht, D. Dennis, and D. Marchant. Experimental analysis of sublimation dynamics for buried glacier ice in Beacon Valley, Antarctica. *2017 AGU Fall Meeting.* New Orleans, LA, 11-16 Dec.

D. Dennis, **S. Ehrenfeucht**, and D. Marchant. Assessing the impact of sublimation on the stable water isotope signal of surface ice. *2017 AGU Fall Meeting.* New Orleans, LA, 11-16 Dec.

A. Concilio, J. Nippert, **S. Ehrenfeucht**, K. Cherwin, and T. Seastedt. Imposing antecedent global change conditions rapidly alters plant community composition in a mixed-grass prairie. *Oecologia.* 182(3):889-911, 2016. https://doi.org/10.1007/s00442-016-3684-4.

FELLOWSHIPS and GRANTS

Future Investigators in NASA Earth & Space Science Technology **2020 - 2023**
University of California-Irvine (Award #80NSSC20K1618; $135,000)

- Provided 3 years of graduate student support

Undergraduate Research Opportunities Program (UROP) **Summer 2013**
University of Colorado at Boulder ($2,000)

- Provided summer funding while conducting research internationally

TEACHING EXPERIENCE

GIS in Environmental Science: ESS 134 **Spring 2021**
Teaching Assistant *University of California- Irvine*

California Land and Climate: ESS 162 **Spring 2020**
Teaching Assistant *University of California- Irvine*

The Atmosphere: ESS 5 **Winter 2020**
Teaching Assistant *University of California- Irvine*

Introduction to Earth System Science: ESS 1 **Fall 2019**
Teaching Assistant *University of California- Irvine*

Introduction to Climate and Earth System Science: ES 107 **Fall 2017**
Teaching Fellow *Boston University*

Introduction to Quantitative Environmental Modeling: GE 375 **Spring 2017**
Assistant to Instructor *Boston University*

Oceanography: ES 104 **Spring 2016**
Teaching Fellow *Boston University*

Abstract Algebra: MATH 3140 **Fall 2013**
Assistant to Instructor *University of Colorado at Boulder*

OUTREACH

EmpowHer *September 2022 - Present*

- Mentor in program
- Empowering Women through High School Engagement and STEM Research: A mentoring program, paired with an in-person conference, designed to foster interest and increase accessibility of STEM careers to high school students who identify as women

CLEAN education group *September 2018 - Present*

- Program member, instructor
- Climate, Literacy, Empowerment and iNquiry (CLEAN) is a graduate student led educational and outreach organization with the explicit goals of improving the understanding of climate science at local public schools

First Gen Bees *October 2021 - Present*

- Program developer
- This program is actively being developed and expanded. Workshops provide assistance with the college application process and general advice for first-generation college bound and low-income high school students who are interested in STEM careers

Upward Bound *July 2019*

- Coding instructor
- Upward Bound provides first-generation college bound and low-income high school students with college prep classes

SERVICE

Member of the Inclusive Excellence Committee *September 2020 - Present*

- Meets monthly to discuss ways promote and improve diversity, equity, and inclusion within the department

Unlearning Racism in GeosciencE (URGE) *January 2021 - Present*

- NSF-funded national program with the goals of improving knowledge of racism within the geoscience community and developing anti-racist policies and strategies within departments
- Member of UCI-ESS URGE pod since establishment of the program

DECADE Representative *September 2019 - September 2021*

- Graduate student representative of the Diverse Education Community and Doctoral Experience (DECADE) for the Earth System Science department at UCI
- DECADE aims to increase the participation and retention of women and under-represented minorities in academia
- Organized outreach and culture-building events for my departments
- Coordinated multiyear anonymous polling of the grad and postdoc communities with regards to mental health and general well-being
- Successfully petitioned the department to stop requiring the GRE for Ph.D. applications

AWARDS

Outstanding Contributions to the Department **2021-2022**
University of California-Irvine: School of Physical Sciences

Earth System Science Inclusive Excellence Award **2020-2021**
University of California-Irvine: Department of Earth System Science

PROFESSIONAL DEVELOPMENT

Diversity in STEM Seminar *2020-Present*
- This course is designed to examine how diverse, intersectional identities shape the STEM experience, with a focus on the geosciences. Topics address the current state of systemic racism in higher education, impacts on diversity, and evidence-based approaches to increase diversity in geoscience.

Inclusive Excellence Certificate Program *2021-2022*
- A 2 term program developed for faculty, staff, and students to learn and recognize how diversity, equity, inclusion, and free speech intersect, and how to apply strategies to advance the success of all members of the campus community

Mentoring Excellence Certificate Program *Winter 2022*
- A 6 week certificate program which provides evidence-based training developed for grad students and postdocs to develop effective mentoring skills

Black Thriving Initiative Modules *Fall 2021*
- A series of 3 short courses, 5 weeks each, which act to examine anti-Black racism in the United States through a journal club style series of lectures and discussions

Ice and Climate Karthaus Summer School *September 2019*
- Two week short course for Ph.D. students working on climate research within glaciology

Inclusive Instruction Working Group *May 2019*
- This was a graduate student led and organized 5-week series focused on cultivating habits of accessible teaching practices

Ph.D. ADVISORS

Dr. Eric Rignot
Donald Bren and Chancellor's Professor
University of California - Irvine; Department of Earth System Science

Dr. Mathieu Morlighem
Evan's Family Distinguished Professor of Earth Sciences
Dartmouth College; Department of Earth Sciences

ABSTRACT OF THE DISSERTATION

Modeling the evolution of coupled ice flow dynamics and subglacial hydrology for Petermann Glacier, Northern Greenland, on seasonal, inter-annual, and centennial time-scales

By

Shivani Ehrenfeucht

Doctor of Philosophy in Earth System Science

University of California, Irvine, 2023

Professor Eric Rignot, Chair

Petermann Glacier is a major outlet glacier of northern Greenland that drains a marine-based basin vulnerable to destabilization from enhanced oceanic and atmospheric forcings. Satellite observations show significant grounding line retreat of ∼7 km in a central region of the glacier, with at least 1 km of retreat elsewhere along the grounding line. This represents a significant shift from the glacier's previously stable grounding line position mapped in the 1990s. Satellite observations also show a seasonal ice acceleration for Petermann of 15% in the summer, from 1,250 to 1,500 m/yr measured close to the grounding line. We use a subglacial hydrology model (GlaDS) and an ice sheet model (ISSM) with asynchronous coupling to evaluate the role of subglacial hydrology as a physical mechanism explaining the seasonal speedup of ice velocity. Results show an excellent agreement between the observed and modeled velocity in terms of timing and magnitude when an applied lower limit on effective pressure of 6% of ice overburden pressure is imposed in the ice flow model. We conclude that seasonal changes in subglacial hydrology are sufficient to explain the observed seasonal speed up of Petermann Glacier. Current projections of glacier dynamics under 21st century climate forcings do not include seasonality or subglacial hydrology, so it is unknown if either will play any important role in evolving glacier dynamics under different climate change scenarios.

We use climate forcings through 2100 to investigate how the subglacial hydrologic system may evolve in a warmer climate, and to test if including hydrology changes the stability of Petermann under future climate scenarios using ISSM and the GlaDS model in both an asynchronous and synchronous coupled configuration. Results show that including subglacial hydrology in projections of Petermann's evolution yield larger predictions of future sea level rise by the end of the century. However, modeled results of both present day and future ice dynamics with and without subglacial hydrology included do not reproduce the observed grounding line retreat. To better understand grounding line migration of Petermann, we apply a newly published theory of seawater intrusion below grounded ice. By incorporating ocean driven basal melting in the grounding zone, we achieve a significantly improved match to the observed grounding line behavior that previous model setups failed to reproduce. This underscores the importance of considering ocean-driven melting to accurately capture grounding line behavior. These studies contribute to a deeper understanding of the observed behavior of Petermann Glacier, particularly its seasonal acceleration and grounding line migration. Subglacial hydrology and seawater intrusion both emerge as influential short time scale processes on ice dynamics, with potential long term implications on glacier stability and sea level rise.

Chapter 1

Introduction

The Greenland Ice Sheet has a total sea level rise potential of 7.42 meters (Morlighem et al., 2017) and has been losing mass at an accelerating rate over the last several decades (Howat et al., 2005; Mouginot et al., 2019). The northern and north-eastern sectors of the Greenland Ice Sheet (GrIS) are particularly important regions for determining Greenland's overall contribution to future sea level rise, because large sections of this sector sit below sea level making the region vulnerable to destabilization (Morlighem et al., 2014; Mouginot et al., 2019). There remains quite a bit of uncertainty in the predictions of 21$^{\text{st}}$ century sea level rise from the GrIS. Quantifiable uncertainties from ice sheet model variation and uncertainties associated with model forcings (i.e. climate model and ocean model uncertainty) are studied in inter-model comparison projects (Goelzer et al., 2020; Seroussi et al., 2020), but only make up some of the variability associated with sea level projections. The choice of friction law (Åkesson et al., 2021) and calving law (Choi et al., 2018; Goelzer et al., 2020) in model simulations also has a large impact on the resulting predicted sea level rise. Ocean driven basal melt parameterizations introduce additional assumptions that alter results; full coupling to an ocean model produces the most realistic patterns of basal melt, but is often prohibitively computationally expensive. Additional processes such as subglacial hydrology are often left out of simulations entirely.

While the dynamics of ice sheet flow are well established, detailed satellite observations show that ice shelves in northern Greenland are breaking up more quickly than anticipated, the glaciers are speeding up, and glacier/ice shelf systems are observed to exhibit a strong seasonal variability. Short timescale glacier dynamics can be caused by various physical processes, but are generally less well understood than the longer term trends and behaviors. The impact of short timescale dynamics on long term glacier stability is poorly constrained. Tidal flexure of floating ice can assist in transporting the relatively warm ocean waters further upstream in a glacier's grounding zone, enabling ocean driven melt over a larger area during periods of high tide. Independently, seasonal meltwater runoff percolates to the glacier bed and can cause significant acceleration during the melt season. Neither of these processes are generally included when projecting glacier evolution in response to climate change, so their ability to effect glacier stability are remaining knowledge gaps in the field of glaciology.

Northern Greenland alone drains around 40% of the total ice sheet (Hill et al., 2018). This region is sensitive to both atmospheric and ocean forcings (Morlighem et al., 2019). Key glaciers in this region are marine terminating, several of which still have intact ice shelves. Ice shelves exert important control on glacier dynamics because they have a buttressing effect, which slows the glacier flow by providing a back stress from shearing along the side walls of the bay and valley that contain them (Goldberg et al., 2009). The ice shelves in northern Greenland have been thinning from the top as a result of a warming air temperature, thinning from below due to warmer ocean temperature, and thinning from enhanced flow which stretches the ice longitudinally. Understanding the dynamics of this region is critical to understanding how the GrIS as a whole will contribute to rapid sea level rise in the future. The work described in this dissertation is focused on Petermann Glacier, northwestern Greenland. Petermann is one of the largest glaciers of the GrIS, and has a floating shelf that is roughly 50 km long (Münchow et al., 2014). Petermann also displays fast grounding line migration driven by the tidal cycle, and exhibits a seasonal acceleration of 15% each summer (Millan et al., 2022), making it a good case study for understanding short timescale glacier dynamics. The following chapters will address two main drivers of dynamics for Petermann Glacier over multiple timescales; subglacial hydrology and basal melting of grounded ice. This work explores some of the remaining uncertainties in calculating accurate sea level rise projections from fast, dynamic glaciers, and provides a case study for the relevance of two physical mechanisms operating on short timescales on one such glacier.

1.1 Background

1.1.1 Glacier mass balance

Total ice sheet mass balance is determined by the difference between the Surface Mass Balance (SMB) and the ice discharge (D) along the periphery of the ice sheet. Observed mass loss for the GrIS is attributed to both increased D and decreased SMB (Rignot et al., 2008b; Hill et al., 2018; Van den Broeke et al., 2016). SMB is calculated as the balance between the processes occurring at the surface of the ice sheet, e.g. snow accumulation, runoff, sublimation, evaporation, wind-blown snow, etc), while D is calculated as the total mass flux which crosses the grounding line, the point where the glacier is no longer in contact with bedrock and begins to float on the ocean. Glacier discharge is takes into consideration both calving and the basal melting of floating ice. Greenland's mass loss has been almost equally contributed by SMB and D (Howat et al., 2007).

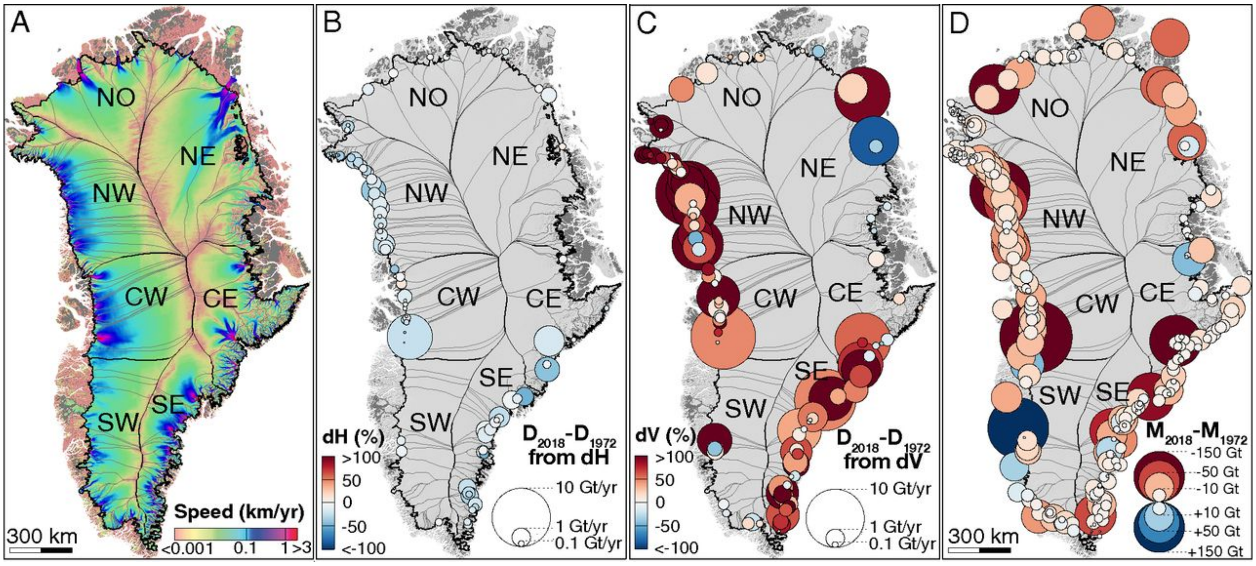

Figure 1.1: **Greenland mass balance from 1972 to 2018.** (A) Seven regional sectors of the Greenland Ice Sheet outlined over mosaic showing ice surface speed (km/year). (B) Change in ice thickness and (C) change in ice velocity of each drainage basin, where color corresponds to the % change and the size of each circle represents the contribution of that change to the resulting change in ice discharge. (D) Total change in mass for each drainage basin. This figure was taken from Mouginot et al. (2019).

1.1.2 Seasonal acceleration of Greenlandic glaciers

Many glaciers in Greenland have been observed to experience a characteristic seasonal ice acceleration (Bartholomaus et al., 2011; Howat et al., 2008; Joughin et al., 2008; Lemos et al., 2018; Millan et al., 2022; Moon et al., 2014; Vijay et al., 2019), although the pattern of behavior in seasonality can vary widely and has been attributed to seasonally changing ice front positions (driven by calving) (Howat et al., 2008; Kehrl et al., 2017; Lemos et al., 2018; Moon et al., 2014), evolving subglacial hydrology (driven by meltwater runoff) (Bevan et al., 2015; Kehrl et al., 2017; Moon et al., 2014; Rathmann et al., 2017; Zwally et al., 2002), or sometimes a combination of the two (Moon et al., 2014). Calving is able to cause speedup of ice velocity by reducing the back stress on the glacier, whereas seasonal runoff impacts velocity by lubricating the glacier bed and thereby altering basal friction. Glaciers exhibiting typical behavior associated with seasonality driven by calving have a speedup that coincides with ice front retreat, and a slowdown that coincides with ice front advance.

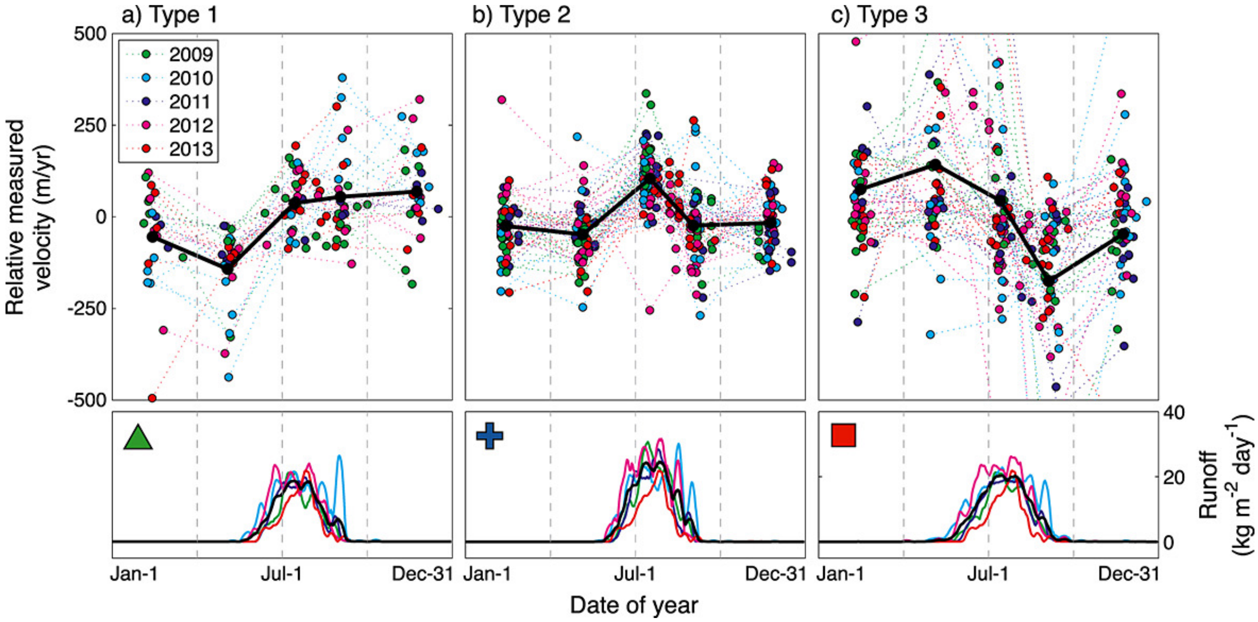

Figure 1.2: **Seasonal behavior of ice velocity (m/yr) for 55 marine-terminating Greenland outlet glaciers.** Three distinct behaviors are observed in satellite observations using TerraSAR-X radar data. (a) Type 1 is determined to have seasonality corresponding to glacier front position. (b) Type 2 and (c) Type 3 glaciers have seasonal behavior associated with subglacial hydrologic system with either an inefficient distributed state (Type 2) or an efficient channelized state (Type 3). This figure was taken from Moon et al. (2014).

Although ice front retreat can coincide with the onset of summer surface melt, glaciers which are considered to be calving-driven retain their summer speed past the end of the melt season, eventually slowing down later in the fall as the ice front extends again. Glaciers exhibiting typical behavior associated with seasonality driven by meltwater runoff can have a velocity pattern that closely correlates to the volume of runoff (Moon et al., 2015; Vijay et al., 2019), or they can exhibit a much more complex relationships between meltwater runoff and speed (e.g. Chu et al. 2016). For some glaciers, velocity initially increases, but with high rates of runoff velocity decreases, reaching an annual minimum in late summer and winter acceleration (Abe and Furuya, 2014; Quincey et al., 2009). The former is associated with inefficient flow through the subglacial hydrologic system, while the latter is associated with a transition to efficient flow partway through the melt season (Moon et al., 2014, 2015; Vijay et al., 2019).

1.1.3 Subglacial hydrology

There is substantial surface melting in Greenland during the summer months, when surface air temperatures rise above freezing (Van den Broeke et al., 2016). Some surface melt refreezes and becomes solid ice again, but a large amount remains liquid and develops into a complex hydrologic system that interacts with glacier physics. Surface meltwater runoff collects in pools at the surface forming supraglacial lakes, flows across the top of the glacier carving streams into the ice surface (Smith et al., 2015), and also percolates vertically through the ice eventually reaching the underlying bedrock (Chu et al., 2016; Clason et al., 2015). The meltwater runoff that reaches the ice-bed interface evolves a subglacial hydrologic system, where it combines with other sources of subglacial water, such as frictional melt and geothermal basal melt. Initially, meltwater collects in isolated cavities (Bartholomew et al., 2012), but as the volume of input increases, these cavities connect, forming a thin, distributed sheet of flowing water along the glacier bed (Schoof et al., 2012). With further input, the system evolves into a channelized network that allows for the quick transport of water from the subglacial hydrologic system across the grounding line, the location at which the glacier transitions from sliding across the bedrock to floating in the ocean, where it is discharged to the ocean (Dow et al., 2022; Kamb, 1987; Hewitt et al., 2012; Shreve, 1972).

The presence of water within the subglacial hydrologic system alters the basal friction exerted on the glacier by the underlying bedrock (Sommers et al., 2018; Werder et al., 2013), allowing changes in subglacial hydrology to impact ice flow. Observations have correlated changes in subglacial hydrology to ice velocity for many Greenland glaciers (Moon et al., 2014, 2015; Vijay et al., 2019; Zwally et al., 2002), and theoretical modeling studies have shown that this relationship can be reproduced by combining the physics of subglacial hydrology and glacier ice flow (e.g. Hewitt 2013). While it is understood that freshwater discharge from the subglacial hydrologic system can have an impact on ice flow, it remains unclear under what conditions and to what degree these changes occur. It also remains unclear if the changes

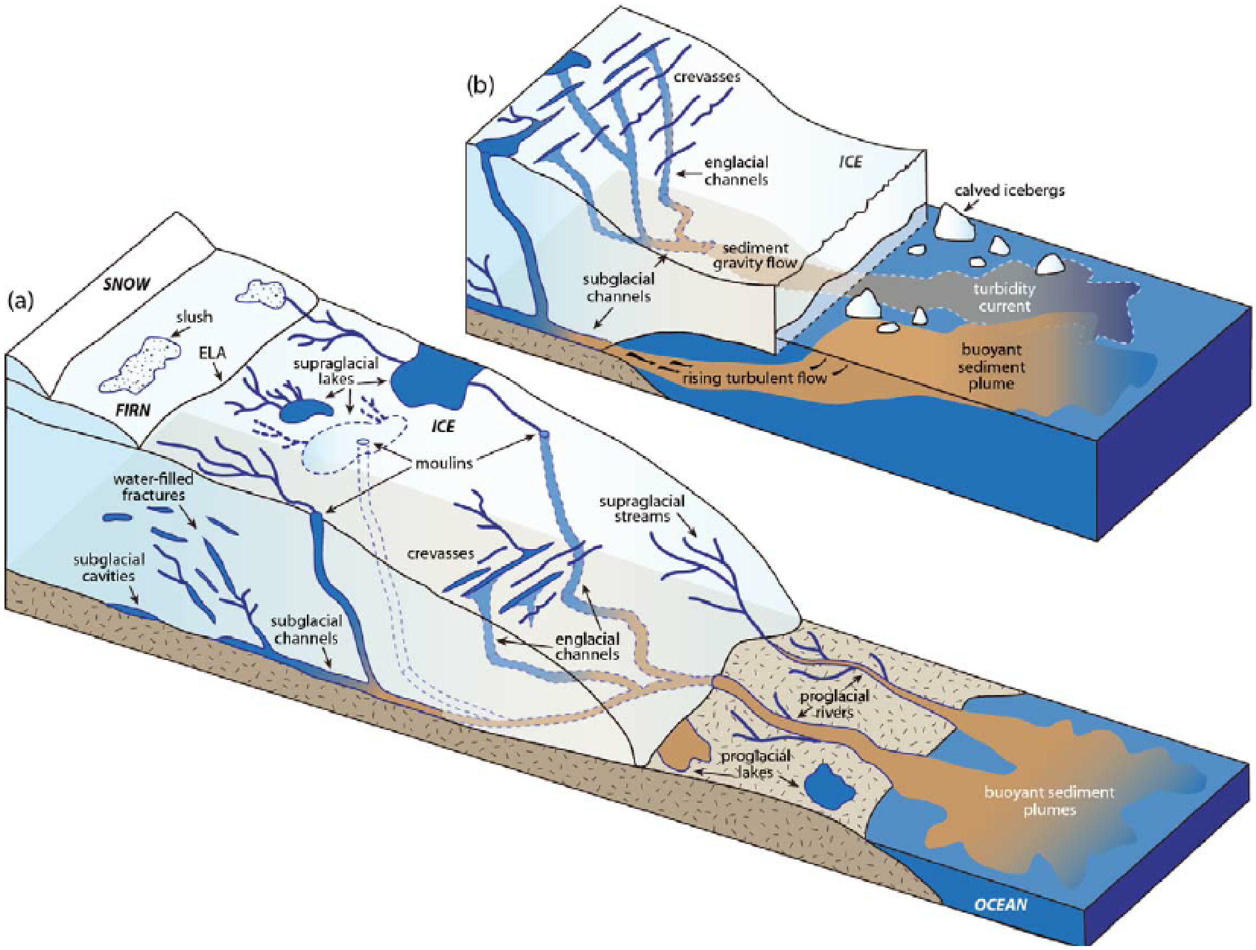

Figure 1.3: **Components of the hydrologic system for the Greenland Ice Sheet.** (a) Meltwater runoff collects and flows across the surface in streams, forming supraglacial lakes, and percolates vertically through the glacier to the bed via cracks, crevasses and moulins. At the bed, surface water combines with other sources of melt. Subglacial water collects in cavities, develops into a thin sheet-like layer of water between the glacier and the bedrock, and evolves networks of subglacial channels that form proglacial rivers after exiting the subglacial environment at the terminus of the glacier. (b) For marine-terminating glaciers, subglacial discharge enters the ocean directly, where it combines with warm ocean water and enhances sub-ice shelf melt rates. This figure was taken from Chu (2014), and was originally adapted from Cuffey and Paterson (2010).

to ice flow induced by evolving subglacial hydrology have any long term effects on glacier stability. The uncertainty associated with subglacial hydrology on sea level rise projections due to climate change is often cited as a critical unknown remaining in glaciology (Armstrong et al., 2022; Moon et al., 2018; Simkins et al., 2023; Thøgersen et al., ress).

1.1.4 Ice shelf basal melting

Ocean circulation brings warm salty water to the coast of Greenland, where it sits below the more buoyant and cold freshwater from ice melt. Warm deep water enters into the fjord where it then contributes to glacier dynamics (Jenkins, 2011). Since the melt water discharged is less dense than the ocean water, upon reaching the fjord it flows vertically. This vertical motion creates turbulent mixing, wherein the warm deep water mixes with the melt water and buoyantly rises. The result of this process is a plume of relatively warm water flowing along the base of the floating ice towards the ice front, enhancing melt along the ice-ocean interface near the grounding line (Cai et al., 2017; Pelle et al., 2019). This causes ice shelf thinning and is a substantial form of mass loss for some glaciers Pritchard et al. (2009).

The melting of floating ice can reduce the buttressing effect of ice shelves on glaciers, resulting in increased ice discharge and ultimately contributing to rising sea levels (Sun et al., 2020). Moreover, subglacial discharge plays a significant role in the ocean-driven melting of ice shelves (Dow et al., 2022; Gwyther et al., 2023), yet it is currently not always incorporated into ice sheet models, potentially leading to inaccuracies in their projections of future ice behavior and sea level rise. Runoff is not discharged uniformly at the grounding line, but is dependent on how the subglacial hydrologic system evolved. Modeling studies have demonstrated that subglacial discharge can amplify ice shelf melt (Sergienko et al., 2013; Nakayama et al., 2021) and melting at the calving front (Cook et al., 2020). Recent research has also postulated that the intrusion of seawater under grounded ice through the subglacial hydrologic system has the potential to significantly enhance melt rates and induce rapid grounding line retreat (Robel et al., 2022; Wilson et al., 2020). Discrepancies between melt rates by inferred by satellites, field measurements, and calculated by ocean models (Catania et al., 2010; Ciracì et al., 2023; Jackson et al., 2022) could potentially be explained or mitigated by accounting for subglacial discharge in a more physically realistic manner.

Many ice shelves have characteristic channels along their base in the direction of ice flow, that some have suggested are caused or enhanced by the irregular pattern of meltwater discharged from subglacial hydrology (Le Brocq et al., 2013; Sergienko et al., 2013). Ice shelf channels have been associated with enhanced crevassing (Alley et al., 2016), and have been suggested to structurally weaken ice shelves (Goldberg et al., 2019; Pritchard et al., 2012). Others suggest an overall stabilization effect (Millgate et al., 2013). Several modeling studies have connected the presence of channels enhanced rates of fracture (Sergienko et al., 2013; Vaughan et al., 2012), which may contribute to the eventual collapse of the ice shelf. Although melting of floating ice does not directly contribute to sea level rise, it can reduce the buttressing effect of ice shelves on glaciers, which can ultimately increase the total ice discharge and thereby increase sea-level rise.

1.1.5 Basal friction and sliding velocity

Basal friction plays a crucial role as an input parameter in ice flow and subglacial hydrology models. It depends on factors such as ice thickness and bed geometry, but can vary significantly between glaciers due to local conditions such as bedrock topography, bed roughness, and meltwater input (Engelhardt et al., 1978; Hubbard et al., 2000). While there have been laboratory experiments to study basal velocity (Budd et al., 1979; Iverson and Zoet, 2015), they are relatively rare as opposed to theory-based studies. Several theories of glacier sliding

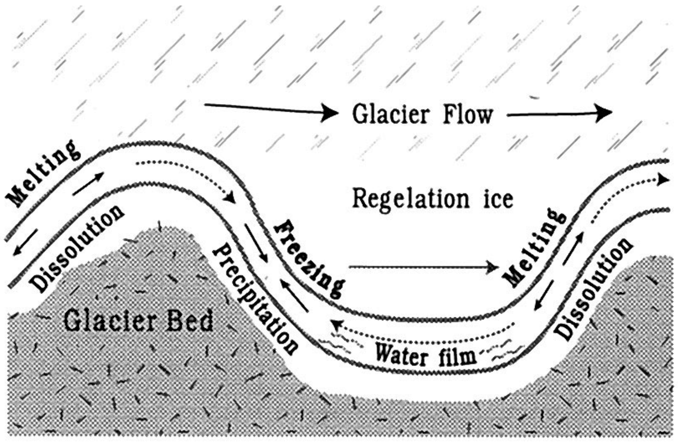

Figure 1.4: **Diagram of the regelation mechanism at the ice-rock interface** for ice flow past small obstacles in the bed. Pressure and temperature gradients create localized regions of melt and refreezing. This figure was taken from Fountain and Walder (1998).

have been developed since the 1950s, based on lubricated creeping flow principles from classical continuum mechanics (Kamb, 1970; Lliboutry, 1968; Schoof, 2005; Weertman, 1957). Generally, sliding laws incorporate two mechanisms: regelation and enhanced creep.

In the regelation sliding mechanism, it is assumed that the ice is at its pressure melting temperature at the ice-rock interface throughout the base. When the ice encounters a bump in the bedrock that obstructs its flow, a pressure gradient is generated parallel to the flow direction. The ice upstream of the bump experiences greater pressure from the rock compared to the ice on the downstream side. This pressure gradient leads to a temperature gradient. The ice downstream of the bump becomes colder than the pressure melting temperature, causing the refreezing of meltwater. The release of heat during water freezing is absorbed by the bedrock, creating a temperature gradient. As a result, the downstream side of the bump becomes warmer, and heat flows upstream through the bump. This warms the ice on the upstream side of the bump, causing it to exceed its pressure melting temperature and leading to melting. This melting-freezing mechanism allows the ice to flow around relatively small obstacles in the bedrock.

On the other hand, the creep mechanism of basal sliding is more straightforward. When the ice encounters a sufficiently large obstacle while sliding over the bed, it viciously deforms around the obstacle. As the ice reaches a larger bump in the bedrock it is forced to change direction. Under the assumption of incompressibility, this change in direction causes the ice to deform by compressing in the direction of flow. This deformation induces a vertical extension, enabling the ice to flow over and around the obstacles. The deformation is caused by enhanced stress (Fowler, 2010).

The enhanced creep mechanism is more effective for large obstacles, as the area of ice which is experiencing enhanced stress is related to the size of the obstacle. A large bump in the bedrock will cause a large area of ice upstream to experience enhanced stress. The product of this area and the strain rate is the determining factor in how fast the ice can deform around an obstacle. Since regelation operates on a heat flux through the obstacle, it is limited by the size of the obstacle, and ice is able to get past smaller obstacles more easily.

Weertman (1957) applied these concepts to glaciers and proposed a theory of sliding, which assumed that both mechanisms are operating simultaneously, allowing glaciers to flow past a spectrum of obstacles of varying sizes. The Weertman sliding law relates shear stress, τ_b, directly to basal sliding velocity, u_b:

$$\tau_b = C_W ub^{1/n}, \tag{1.1}$$

where C_W is a friction parameter, and n is the flow law exponent, which is generally taken to be 3.

Multiple alternatives have been developed since the publication of Weertman's sliding law, many of which take into consideration some of the simplifications made by the original formulation. Cavitation, the process in which gaps form between the ice and bedrock due to

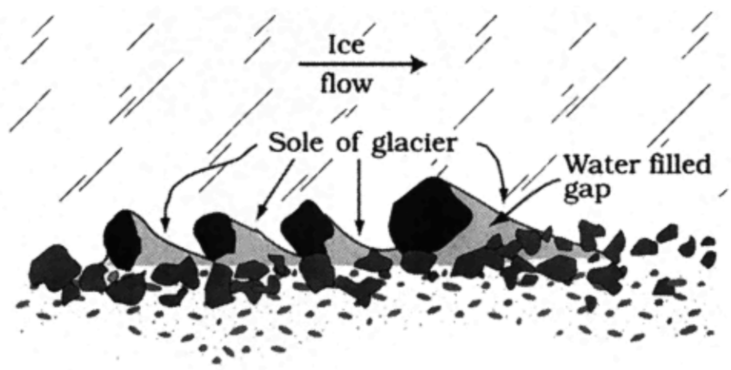

Figure 1.5: **Diagram of a theorized microcavity network** created by obstacles in the subglacial environment that allow for the development of a linked network of water filled cavities. This figure was taken from Fountain and Walder (1998), and describes ideas first pointed out by Kamb (1987).

sliding, was disregarded by Weertman and first suggested by Lliboutry (1968) and remains widely used. Accounting for cavitation requires an additional term in the sliding law: effective pressure, N, is the difference between the ice overburden pressure and water pressure at the base of the glacier.

$$N = P_{ice} - P_{water} = \rho_{ice} g H - P_{water}, \tag{1.2}$$

where ρ_{ice} is the density of ice, g is the gravitational constant, and H is the ice thickness.

Many sliding laws have now incorporated effective pressure into their formulation (e.g. Budd et al. 1979; Schoof 2005). The Budd sliding law remains the simplest of these, and was developed based on laboratory experiments which showed a strong dependence of τ_b on N from experiments of pressurized ice sliding over rock surfaces with various degrees of roughness. The new relationship between τ_b and u_b takes the form:

$$\tau_b = C_B^2 u_b^{1/n} N^q, \tag{1.3}$$

where C_B is the friction coefficient associated with the Budd friction law, and q is a positive constant.

More complex representations of basal friction have been proposed in recent years in the form of regularized coulomb friction laws (Brondex et al., 2019; Joughin et al., 2019; Nias et al., 2018), of which there are multiple variations. One specific form, referred to as the Schoof friction law (Schoof, 2005), incorporates an Iken bound (Iken, 1981) to establish an upper limit on tau_b when N is small:

$$\boldsymbol{\tau}_b = -\frac{C_S^2 \left|\boldsymbol{v}_b\right|^{m-1} \boldsymbol{v}_b}{\left(1 + \left|\boldsymbol{v}_b\right| \left(\frac{C_S^2}{C_{\max} N}\right)^{\frac{1}{m}}\right)^m}, \tag{1.4}$$

where C_S is the friction coefficient associated with the Schoof friction law, $C_{\max} \sim \tau_b/N$ is Iken's bound, which is connected to the bedrock geometry (Gagliardini et al., 2007; Iken, 1981; Schoof, 2005), and $m = 1/n$. $C_{\max}$ typically ranges between 0.17 and 0.84 according to lab experiments (Cuffey and Paterson, 2010).

1.2 Dissertation objectives

The global concern of sea level rise, which is expected to become increasingly pressing over the next century, necessitates the use of models to make accurate projections. We rely on models to project the rate of sea level rise, including from melting ice sheets, but those models are missing key components to accurately estimate additions of freshwater to the oceans (Masson-Delmotte et al., 2021). In particular, the role of subglacial hydrology in ice dynamics and ice shelf stability has, to date, not been included in models projecting sea level rise. In this work, we aim to understand the role of subglacial hydrology in the ice dynamics of Petermann Glacier and its contribution to projected sea level rise, with a focus on understanding the interactions between subglacial discharge, ice acceleration, and grounding line retreat. There are two central questions we aim to address: (1) What are the physical processes that make Petermann change rapidly on seasonal and inter-annual time scales? and (2) What contribution to sea-level rise should we expect from Petermann in the coming century?

1.3 Chapter overviews

In chapter 2, we test the ability of changes in subglacial hydrology to explain the observed seasonal cycle in ice velocity of Petermann Glacier. In recent years, extensive satellite data have become available which provide frequent and widespread observations over much of the Greenland ice sheet, including Petermann. Access to such records provides the opportunity to investigate changes in glacier dynamics taking place over much smaller time periods. We see that in the summer Petermann's speed increases by about 15% from 1,250 meters/year to 1,500 meters/year near the grounding line. We use two finite-element numerical models: 1) a subglacial hydrology model which calculates how effective pressure at the bed evolves over the course of the summer melt season; and 2) and an ice sheet model that uses the effective pressure calculated by the subglacial hydrology model to calculate the new glacier velocity. The offline, asynchronous coupling between these models is the first application of a coupled model framework between subglacial hydrology and ice dynamics applied to questions of ice velocity without using an idealized ice geometry. We validate modeled results by comparison to the satellite record of ice velocity over three consecutive years, and discuss the subglacial hydrologic system which evolves during simulations. Our model successfully replicated the observed pattern in speed, demonstrating that changes in subglacial hydrology play a critical role in driving the observed seasonality of Petermann's velocity and merits further investigation to better understand its role in glacier dynamics more generally.

In chapter 3, we address the lack of consideration for subglacial hydrology in 21$^{\mathrm{st}}$ century sea level rise projections. We apply two different coupling model frameworks to Petermann, integrating subglacial hydrology with ice dynamics and comparing results to projections that ignore the physics associated with an evolving hydrologic system. Our model frameworks include one in which the models have synchronously coupled ice dynamics and subglacial hydrology, where results from the hydrology model are fed into the ice flow model at each time step with new fields for ice flow variables then fed directly into the hydrology model to calculate results at the next model time-step. We also run simulations using an asynchronous modeling framework where the subglacial hydrology is run first for the full 100 year simulation. We then give the results from the hydrology run to the ice flow model so that ice dynamics are calculated with evolving subglacial hydrology. Since hydrology is calculated with static ice flow variables, comparison of these runs to those from the synchronously coupled model framework allows us to examine the impact that hydrology has on ice dynamics and the feedback from those changes in ice dynamics back on hydrology.

In chapter 4, we focus on understanding the grounding line migration that has been observed for Petermann over recent years in the satellite data record. Observations show extensive grounding line retreat not captured by previous modeling studies. We examine the ability for ocean induced melting of grounded ice to explain the pattern of retreat present in the data. Seawater intrusion beneath grounded ice, by a mechanism similar to the salt wedge mechanics observed in marsh environments, has been recently suggested as a missing component of glacier physics at the ice-ocean interface. This theory models overlaying layers of ocean water below freshwater melt in the subglacial environment. A sustained layer of freshwater sits between the glacier base and the bedrock in the subglacial hydrologic system, allowing for the intrusion of seawater below the grounded ice if the velocity within the freshwater layer is sufficiently small. We apply this theory to our modeling framework of Petermann. Informed by the results from the subglacial hydrology model GlaDS, we are able to explicitly solve for the maximum intrusion distance, and introduce ocean driven basal melt in kilometer-size intrusions beneath the grounded ice. We achieve a vastly improved match of observed grounding line retreat, without requiring the use of an arbitrarily large basal melt rate. Additionally, model results using seawater intrusion help match the trend of winter velocity acceleration observed on Petermann since 2010.

Chapter 2

Seasonal acceleration of Petermann Glacier, Greenland, from changes in subglacial hydrology

S. Ehrenfeucht, M. Morlighem, E. Rignot, C.F. Dow, J. Mouginot

As presented in:

Ehrenfeucht, S., Morlighem, M., Rignot, E., Dow, C. F., and Mouginot, J. (2023). Seasonal acceleration of petermann glacier, greenland, from changes in subglacial hydrology. *Geophysical Research Letters*, 50(1):e2022GL098009

2.1 Abstract

Petermann Glacier is a major outlet glacier of northern Greenland that drains a marine-based basin vulnerable to destabilization from enhanced oceanic and atmospheric forcings. Using satellite radar interferometry data from the Sentinel-1a/b missions, we observe a seasonal glacier acceleration of 15% in the summer, from 1,250 to 1,500 m/yr near the grounding line, but the physical drivers of this seasonality have not been elucidated. Here, we use a subglacial hydrology model coupled one-way to an ice sheet model to evaluate the role of subglacial hydrology as a physical mechanism explaining the seasonal acceleration. We find excellent agreement between the observed and predicted velocity in terms of timing and magnitude with the addition of an applied lower limit on effective pressure of 6% of ice overburden pressure. We conclude that seasonal changes in subglacial hydrology are sufficient to explain the observed seasonal speed up of Petermann Glacier.

2.2 Introduction

Seasonality in ice velocity directly impacts annual ice discharge, and is therefore relevant to sea-level rise projections. Understanding the physical mechanism by which glaciers respond to seasonal changes in atmospheric and oceanic forcings will improve our ability to predict the dynamic responses of glaciers to changes in these forcings from a warming climate. Seasonal acceleration has been observed on many Greenland glaciers in recent years due to the growing availability of satellite data, which has allowed a nearly continuous monitoring of glaciers on the timescale of days that was not previously available (Bartholomew et al., 2011; Joughin et al., 2008; Lemos et al., 2018; Moon et al., 2014). It is not known whether these glaciers have always exhibited a seasonal acceleration that remained undetected in the past due to a more limited availability of satellite observations, or if ice flow dynamics have been altered in recent decades in response to climate warming and glacial retreat. As a key example, a study conducted with Global Positioning System (GPS) data from 1985-1986 indicated that Jakobshavn Isbræ, the largest outlet glacier in Greenland, exhibited no seasonal fluctuation in speed (Echelmeyer and Harrison, 1990). A decade later, however, a follow-on study suggested that seasonal fluctuations in speed started to become noticeable in the 2000s (Luckman and Murray, 2005), which coincides with a time period where the climate system was warming up in Greenland compared to previous decades. During this time, Jakobshavn also transitioned from terminating in a substantial ice shelf to a tidewater glacier (Csatho et al., 2008). The loss of the glacier's buttressing ice shelf is attributed to enhanced ocean-driven melting caused by a 1.1°C increase in the temperature of deep ocean waters (Holland et al., 2008; Motyka et al., 2011). Jakobshavn eventually underwent a major transition in ice flow dynamics and state of mass balance. Since then, Jakobshavn is observed to accelerate seasonally by more than 4 km/yr (nearly 40% of its annual average of 10.5 km/yr) (Moon et al., 2014).

In contrast to Jakobshavn, another western Greenland tidewater outlet glacier, Store Glacier, has remained stable over recent years. Modeling of calving dynamics and thermal forcing show that Store is currently being stabilized by a sill and is not particularly sensitive to ocean thermal forcing (Morlighem et al., 2016; Todd and Christoffersen, 2014). Despite its apparent stability, Store also exhibits a seasonal speed up of roughly 10%, which has been observed in GPS records as early as 2010 (Ahlstrøm et al., 2013; Moon et al., 2014), indicating that seasonality may be a component of the typical dynamics of at least some glaciers. Additionally, ice discharge across the Greenland Ice Sheet exhibits a seasonality which closely follows the pattern of seasonal meltwater runoff, and is consistently observed in each sector, regardless of glacier stability. Summer time discharge increases by 6% averaged over the full ice sheet, with the northwestern sector exhibiting the largest increase (9%) and the southeastern sector exhibiting the smallest increase (5%) (King et al., 2018). As such, understanding seasonality is important for a more complete understanding of glacier dynamics and for accurate calculations of annual ice discharge.

Seasonality in glacier speed has been attributed to various physical mechanisms, with different glaciers exhibiting different dominant mechanisms that control their dynamics. Seasonality in speed on a particular glacier could be related to changes in the intensity of ice-ocean interactions (Cai et al., 2017; Jenkins, 2011), changes in basal hydrology (Andrews et al., 2014; Dow et al., 2015; Hoffman and Price, 2014; Vijay et al., 2019), migrations of the ice front (King et al., 2018; Vijay et al., 2019) or grounding line positions (Walker et al., 2008; Xie et al., 2018), or the formation/disappearance of ice melange in front of the glacier (Amundson et al., 2010; Cassotto et al., 2015). However, the mechanism responsible for the summertime speed up of Petermann Glacier has not yet been fully elucidated. A more complete understanding of seasonality in Petermann's glacier dynamics is required to help understand both current observations and to make more accurate future projections of the glacier's evolution.

Petermann is one of the largest glaciers in northern Greenland, with an average ice discharge of 11.85 $\pm$0.7 Gt/yr from 1986 to present (Mankoff et al., 2020; Mouginot et al., 2019). The glacier is grounded below sea level (Figure 2.1C) and connected to the deep interior of the ice sheet via a narrow submarine channel (Bamber et al., 2013; Morlighem et al., 2014) that makes this northern sector of Greenland susceptible to ocean-driven retreat. Prior to 2010, Petermann terminated in a $\sim$70-80 km long floating ice shelf, but three large calving events in 2010-2012 forced a large retreat of the ice shelf front (Crawford et al., 2018; Falkner et al., 2011) which reduced the ice shelf to 46 km in length (Münchow et al., 2014). The 2010 calving event did not produce a significant change in glacier flow (Nick et al., 2012) or change in grounding line position (Hogg et al., 2016). From 2012 to present, the ice shelf front of Petermann has remained relatively stable. An observed 10% acceleration in winter velocity between 2012 and 2017 was attributed to the combined effect of the 2012 calving event and the formation of a large rift in 2016 (Rückamp et al., 2019). The average velocity from 2016 to 2019 was 1,240 m/yr at the grounding line center. Summer speeds increased during this time period to a maximum of 1,475 m/yr, 1,495 m/yr, and 1,409 m/yr in mid-July of 2016, 2017, and 2018, respectively (Figure 2.1D). A previous study observed seasonal speedup on Petermann in the summers of 2011 and 2012 (Ahlstrøm et al., 2013). To the best of our knowledge there are no records of summer time acceleration for Petermann before 2011, and no continuous record which clearly shows the magnitude of acceleration until 2016 (Lemos et al., 2018).

Subglacial hydrology exerts a control on ice velocity by moderating the effective pressure at the ice-bedrock interface (Nienow et al., 2005; Sole et al., 2011). Summer meltwater runoff enters the subglacial hydrological system through crevasses, cracks, and moulins at the ice surface. Runoff drains through the ice to the glacier bed, where it migrates downstream and discharges into the ocean at the grounding line. The presence of liquid water at the ice-bed interface modulates sliding velocity by altering the basal friction (Lliboutry, 1958). An increased volume of water in the subglacial hydrologic system, however, does not necessarily lead to further reduced friction and a consequential increase of ice velocity because the subglacial hydrologic system is nonlinear (Schoof, 2010; Nienow et al., 2017; Davison et al., 2019). Relatively small fluxes of water typically flow beneath the glacier inefficiently as a distributed sheet that lubricates the ice-bed interface (Parizek and Alley, 2004; Zwally et al., 2002). When a large volume of meltwater input is sustained, channels develop to create a more efficient drainage system (Andrews et al., 2014; Schoof, 2010; Werder et al., 2013). This effective drainage reduces the water pressure, draws water from the distributed system, and decreases basal lubrication. Thus, isolated cavities of melt and a fully channelized system are the two end-members of subglacial hydrology; most glaciers that experience warm atmospheric temperatures likely shift along a continuum between these limits as the melt season progresses with an inefficient hydraulic sheet developing as an intermediate state (Sommers et al., 2018).

In this work, we aim to test whether changes in subglacial hydrology can explain the observed seasonal cycle in ice velocity of Petermann Glacier. We use a combination of two finite-element numerical models: 1) a subglacial hydrology model employed to predict how effective pressure at the bed evolves over the course of the melt season; and 2) an ice sheet model

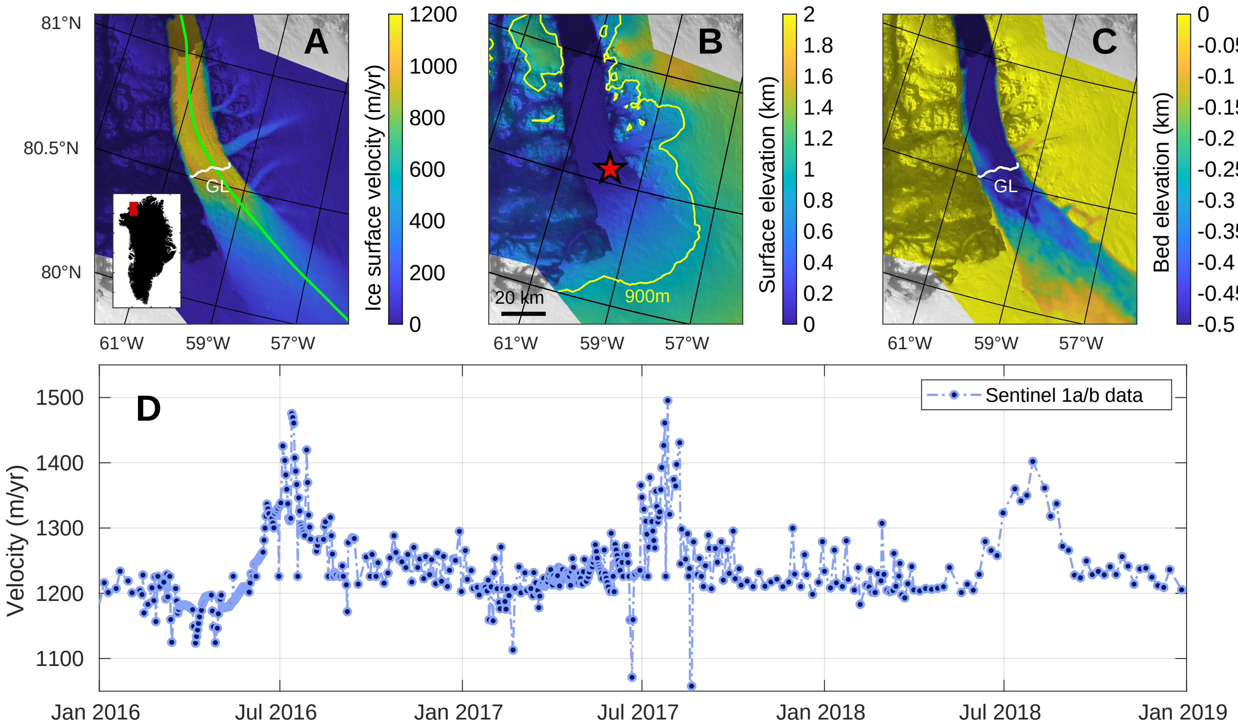

Figure 2.1: **Observations of Petermann Glacier.** (A) Ice surface speed Joughin et al. (2010) derived by averaging data spanning 1995-2015, (B) surface elevation above mean sea level, and (C) bed elevation (Morlighem et al., 2017) of Petermann Glacier, Greenland. (D) Velocity time series from Sentinel 1a/b observations is measured at the location indicated in panel B by the red star. Surface and bed elevations are derived from data corresponding to 2007. The white line is the 1996 grounding line. The green line in panel A is the central flow line. The yellow line in panel B is the 900 m ice surface elevation contour, which is the upper bound of the equilibrium line elevation.

where the seasonal cycle in effective pressure is used to calculate the new glacier velocity. We evaluate the results by comparing our calculated ice velocity to satellite observations of ice velocity from three consecutive years, and discuss the subglacial hydrologic system which evolves during simulations.

2.3 Data and Methods

2.3.1 Subglacial hydrology

We calculate effective pressure, N, using the Glacier Drainage System model (GlaDS) over a region of roughly 6,000 km^2 (Figure S.1A) in order to determine how basal friction changes over the course of the melt season. The effective pressure is defined as $N = P_i - P_w$, where P_i is ice overburden pressure and P_w is water pressure. $P_i = \rho_i g H$, where ρ_i is ice density, g is the gravitational constant, and H is ice thickness. GlaDS is a two-dimensional model which combines equations for the development of R-channels with the distribution of meltwater throughout a sheet-like drainage system, where both systems are formulated using the empirical Darcy-Weisbach law (Werder et al., 2013). GlaDS calculates the effective pressure at the glacier base and the hydraulic potential across the domain based on meltwater input to a prescribed ice-bedrock geometry. Water enters the system via basal melting and surface runoff that drains through the glacier to the bed. Water then flows along the bed following the gradient in hydraulic potential. R-channels, referred to as subglacial channels or simply channels, are melted into the base of the ice at the bed, producing an efficient meltwater drainage network through the transfer of frictional heat into the melting ice. Channel opening is determined by melt rate, which is dependent on sliding velocity, and channels close by ice creep (Röthlisberger, 1972; Nye, 1976; Werder et al., 2013). We use a zero-flux Neumann boundary condition along the edges of the domain except at the outflow boundary located at the grounding line of the glacier where we use hydrostatic ocean pressure as the boundary condition.

2.3.2 Ice flow modeling

We use the Ice-sheet and Sea-level System Model (ISSM) to calculate the ice velocity resulting from seasonally-variable basal friction, which depends on the effective pressure from GlaDS. ISSM is a three-dimensional, finite-element ice flow model (Larour et al., 2012), and here we use the Shelfy-Stream Approximation (MacAyeal, 1985). Critical variables and boundary conditions, e.g. basal friction and ice rigidity, are difficult to observe directly and are therefore inferred using inverse methods (Morlighem et al., 2013). GlaDS and ISSM are coupled one way. GlaDS is implemented into ISSM, which allows us to initialize GlaDS with ISSM. Results from GlaDS are then loaded into ISSM manually to calculate the evolution of the glacier velocity from the time-dependent hydrology simulation. At present, the coupling does not operate in the opposite direction, i.e. effective pressure is calculated assuming a static velocity field. There is a negative feedback between basal velocity and effective pressure as increased velocity reduces water pressure from enhanced cavitation (Hoffman and Price, 2014). Our model cannot currently incorporate this feedback because it is not fully coupled, which is a limitation.

2.3.3 Geometric constraints and ice temperature

Ice-bedrock geometry is defined across both domains using BedMachine v3 (Figures 1 & A.2) (Morlighem et al., 2017), which has a grid resolution of 150 m. GlaDS requires values for basal velocity, basal ice temperature, and rheology. We turn on the optional user-specified basal melt as an additional parameter. ISMIP6 data are used to set basal sliding velocity (Figure A.3A) and basal meltwater production (Figure A.3B) (Goelzer et al., 2018). Basal temperature and ice rheology factor (B) are assumed to be uniform and set at -2°C and 8.34×10^7 Pa s$^{-1/3}$ respectively in the hydrology model. Additional parameters required for GlaDS are listed in the supplemental document (Table A.1). In the ice flow model we use -

15°C for a uniform temperature field. The ice flow model uses a depth averaged temperature, whereas GlaDS specifically uses basal temperature, which is close to the pressure melting point. We choose a value for temperature based on the ISSM submission to initMIP that included a 3-dimensional thermal model (Goelzer et al., 2018). In this work, we are interested in dynamics which occur relatively close to the grounding line. The thermal model calculated temperatures of grounded ice for much of the region within 50 km of the grounding line to be around -15°C. Modeled ice temperature reaches below -20°C in this region and is about -13°C at the grounding line. Using uniform temperature is a common practice and justified given that variations in temperature have a limited impact on basal friction inversions and modeled ice flow results over short time periods (Seroussi et al., 2013). We constrain the ice rigidity based on temperature for grounded ice and solve for it using an inverse approach on floating ice.

2.3.4 Modeling procedure

We run GlaDS with basal meltwater, but without surface meltwater input until a steady state is reached to determine initial hydraulic potential and hydraulic sheet thickness. To start the steady state simulation we use an initial hydraulic potential set to half the overburden pressure (MPa). We use 50% overburden to help with stability, but solutions using several initial conditions were compared. The converged steady state solution was not very dependent on the choice of initial hydraulic potential. We set the initial hydraulic sheet thickness to 0.03 m uniformly (Dow et al., 2016). The end results from the steady state run are used as initial conditions for transient runs with seasonal meltwater runoff driving the evolution of the subglacial hydrologic system. We test multiple values for several of the parameters used in the GlaDS equations, and found the choice of sheet and channel conductivities to be particularly relevant to the results. Results from simulations run with varying conductivities are discussed in the supplemental document (see Table A.3 and Figures A.12-A.17).

We use runoff reconstructed across the Greenland Ice Sheet by the regional climate model, MAR (Modèle Atmosphérique Régional), (Fettweis et al., 2017) and specific datasets from MARv3.9 (Tedesco and Fettweis, 2020). Runoff is added to the ice-bedrock interface via 36 moulins randomly distributed throughout a sub-region of the hydrology domain within the ablation zone (Figure A.4A). Other methods of transporting meltwater runoff to the bed were examined, and results were not particularly sensitive to this choice (See Figures A.18 & A.19). The equilibrium-line altitude of the glacier is set at the long-term average of 800-900 m elevation (Rignot et al., 2001). All moulin locations are set below the ice surface elevation contour of 900 m and at least 5 km inland from the grounding line. Runoff is integrated daily over the full hydrology domain and divided evenly among the moulins, which act as point sources of meltwater input in GlaDS. We do not add moulins close to the grounding line because channels necessarily form along element edges so, with a coarse mesh resolution, placing point sources of runoff close to the grounding line will in effect determine the locations of the channels. In recent years, warming in northern Greenland has increased the extent of surface melt and the length of the melt season (Mernild et al., 2011; Tedesco et al., 2013), which implies that setting the ELA at 900 m may not encompass the entire region subject to surface melting in the 2016-2018 summers. Since we integrate MAR runoff over the full domain, and our model has not proven to be particularly sensitive to where melt is injected to the bed, we do not believe that this will have a significant impact on our results.

We run GlaDS at a 2-hour time step for 4 years, allowing the model to spin up during the first year. A longer simulation was initially conducted where we allowed the model to spin up for 8 years, and found no significant difference in results. Effective pressure compared between the long and short runs can be seen in Figure A.6. The results yield 3 years of effective pressure data. We calculate daily averages of effective pressure, which we use as inputs to calculate ice velocity in ISSM.

The hydrology simulation excludes floating ice, the fjord rocky cliffs on the glacier sides, and regions where ice is less than 100 m thick, but these regions are included in the calculation of ice velocity (Figure A.1B). Ice shelves exert a control on glacier dynamics through buttressing (Gudmundsson, 2013; Howat et al., 2007), so excluding Petermann ice shelf would impact the glacier flow dynamics. We also extend the ice flow domain to the ice divide.

We use a double inversion of ice rheology over floating ice and basal friction under grounded ice using a regularized coulomb friction law (Gagliardini et al., 2007; Schoof, 2005; Joughin et al., 2019), also referred to as a Schoof friction law (Equation 1.4, repeated here for convenience), to initialize the ice flow model:

$$\boldsymbol{\tau}_b = -\frac{C_S^2 \left|\boldsymbol{v}_b\right|^{m-1} \boldsymbol{v}_b}{\left(1 + \left|\boldsymbol{v}_b\right| \left(\frac{C_S^2}{C_{\max} N}\right)^{\frac{1}{m}}\right)^{m}}, \tag{2.1}$$

where $\boldsymbol{\tau}_b$ is basal shear stress, C_S is a friction parameter, $\boldsymbol{v}_b$ is the basal velocity, $C_{\max}$ is an upper limit on $\boldsymbol{\tau}_b/N$ known as Iken's bound, and $m = 1/n$ where $n = 3$ is the Glen's flow law exponent. During the inversion, we use the winter average of effective pressure calculated by GlaDS. We take $C_{\max} = 0.8$ everywhere in the ice flow domain. Iken's bound is generally between 0.17 and 0.84; a range of values determined from laboratory experiments (Cuffey and Paterson, 2010). During the inversion step we try different values in this range and choose the one which gives us the best fit to observations for our initial velocity field. We calculate C_S, which does vary spatially, during the inversion where it is treated as a tuning parameter to match surface velocity to observations. The inversion results can be seen in the supplemental document (Figure A.7).

Daily averaged effective pressure is added to the ice flow domain where it overlaps with the hydrology domain. In regions outside of the hydrology domain, we use a time-invariant effective pressure calculated from initial static ice thickness and bed elevation assuming a perfect hydrological connection to the ocean, i.e. water pressure at the grounding line is equal to the seawater pressure (Vieli et al., 2001). Our effective pressure forcing is calculated without feedback from evolving ice thickness during the simulation. We put a lower limit on effective pressure in the ice flow model such that effective pressure cannot be less than 6% of the overburden pressure:

$$N = \max(N_G, 0.06 \times \rho_i g H), \tag{2.2}$$

where N is the effective pressure used in ISSM and N_G is the effective pressure calculated by GlaDS. The limit on effective pressure prevents water pressure from exceeding 94% of ice overburden pressure, so water pressure is forced to remain less than overburden pressure. Similar limits have been used when modeling till hydrology mechanics where the minimum effective pressure of overlying ice on saturated till is fixed as a small portion of the ice overburden pressure (Aschwanden and Brinkerhoff, 2022; Bueler and van Pelt, 2015; Tulaczyk et al., 2000). We discuss the importance of this parameter later on.

Basal friction is computed from these effective pressure values during the transient simulation. We run the ice flow model at a 1-day time step for 12 years. The initialized model is not in equilibrium and requires time to reach a baseline equilibrium state for winter months. We allow the model to spin up for 9 years, at which point baseline acceleration is minimal. A single year of effective pressure values from the hydrology results are looped so that seasonal effective pressure is present during the full 12 year simulation. This prevents numerical issues that occur at the onset of initiating the one-way coupling in the final years of the simulation, after a baseline equilibrium is reached. The last 3 years of the simulation use effective pressure data calculated from MARv3.9 data spanning the time period of January

1st 2016 to December 31st 2018.

We compare the last 3 years of modeled ice velocity to satellite observations at a point near the grounding line (Lat: 80°33'12.96", Lon: -59°52'36.48"; Figure 2.1B) where the seasonal signal is prominent in our observations (Figure 2.1D). Additional comparisons at other point locations are included in the supplemental document (Figures A.12 and A.13). Ice velocity observations are obtained using C-band synthetic aperture radar (SAR) from the Sentinel-1a/b missions, which yield data with a 150 m resolution and a 6 day repeat cycle (Millan et al., 2022). The data provide a multi-year monitoring of ice velocity at a high spatial and temporal resolution.

2.4 Results

2.4.1 Seasonal subglacial hydrology

The general patterns present during the seasonal evolution of the hydrologic system calculated by GlaDS are persistent from year to year. We discuss the results using the 2018 model output as an example. In 2018, the model displays less dependency on the effective pressure limit as compared to the other years considered in this study, which makes that year of results more insightful than years when the limit is used over a larger region and for a longer period of time.

GlaDS calculates a widespread decrease in effective pressure with the influx of meltwater runoff to the bed (Figure 2.2A-F). Runoff spikes at the beginning of June and remains elevated until mid-August (Figure 2.3A). Quickly after the onset of runoff we see a reduction in effective pressure over a large portion of the domain (Figure 2.2B), which is sustained until meltwater runoff input to the hydrologic system is greatly reduced. During the melt season, modeled effective pressure mirrors runoff. A local minimum in pressure is reached on July 7th (Figure 2.2 B & S), which corresponds to a local maximum in runoff (Figure 2.3A). On July 15th we see a local minimum in runoff and a corresponding maximum in effective pressure (Figure 2.2C) . When runoff drops back below 1 m^3/s on September 4th, effective pressures are nearly back to winter values everywhere in the domain (Figure 2.2 F & S). Minimum effective pressure occurs close to the date when we see peak runoff. In 2016 we see minimum effective pressure about one week before maximum runoff, in 2017 they occur on the same day, and in 2018 we see that minimum effective pressure occurs one day after maximum runoff (Table A.2). Although values vary in magnitude, minimum effective pressure occurs on the same date for most regions of the domain, with the exception being in the immediate vicinity of the grounding line. There is very little variation in effective pressure values within 1 km of the grounding line, where N fluctuates between 0.195 MPa and 0.163 MPa during the year, which is equivalent to water pressure remaining between 97 and 99% of overburden pressure all year. These values are greater than the threshold for water pressure imposed by the lower limit on effective pressure, meaning that in this region the N limit is consistently applied all year during the ice flow simulation. There is no discernible seasonality in effective pressure this close to the grounding line. This pattern is also seen in years 2016 and 2017, although there is some variation in the specific dates.

Distributed subglacial water sheet thickness increases throughout the domain on the scale of centimeters with the addition of melt water runoff to the bed. Within 20 km of the grounding line, water sheet thickness remains elevated year round (dark yellow area in Figure 2.2M-R). In this region, winter sheet thickness is about 0.1 m and does not substantially increase in summer. However, we see this region extend significantly inland during the melt season (Figure 2.2, panel P vs Q). Sheet thickness closely follows the runoff flux; it increases as runoff increases (Figure 2.2N), decreases fractionally when runoff experiences a local minimum (Figure 2.2O), peaks with peak runoff (Figure 2.2P) and then begins to decrease (Figure 2.2Q). By the end of the melt season, sheet thickness had returned back to winter

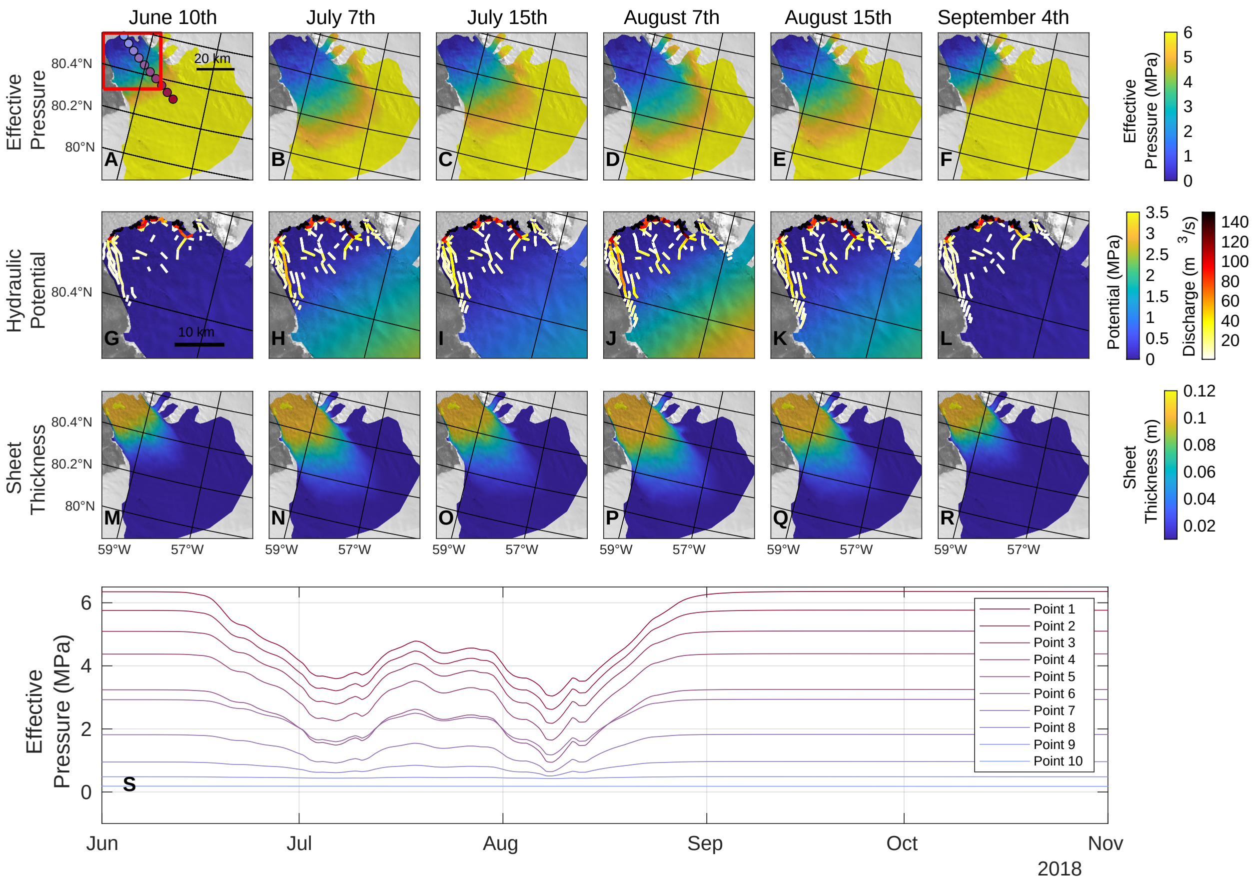

Figure 2.2: **Evolution of the subglacial hydrologic system of Petermann Glacier during the 2018 melt season.** (A-F) Effective pressure, (G-L) channel discharge (m^3/s) overlaid on top of hydraulic potential (MPa), and (M-R) hydraulic sheet thickness on various days during the melt season. The first column for June 10th is the first day when runoff exceeds 1 m^3/s and is representative of the pre-melt season state. The middle row shows channel discharge in a smaller region of the hydrology domain marked by the red square in Panel A. Channels of discharge <1 m^3/s are not shown. (S) time series of effective pressure at point locations, shown in Panel A, along a flow line.

values (Figure 2.2R). The region where the distributed subglacial water sheet reaches its maximum values is in the northwest corner of Figure 2.2M-R (bright yellow region). Results show a sustained water sheet thickness of 0.28 m in this region throughout the duration of the simulation. This is consistently the thickest part of the sheet, with summer values elsewhere remaining below 0.12 m. This region reaches a maximum thickness of 0.3 m during the melt season, and never drops below 0.28 m in the winter months.

Initial channels are established in the first year of the transient hydrology simulation, while we allow the model to spinup. After the initial channels grow, they do not fully close between subsequent melt seasons (Figure 2.2J-L). Instead, they slowly decrease in size between September and the following June, after the majority of water has been drained from the hydrologic system. They do not reach a steady state during the winter months, but instead continue to reduce in size until a substantial volume of runoff is produced the following summer and the channels begin to grow again. Our model predicts the development of several large subglacial channels by the peak of the melt season (Figure 2.2J). We see 2 channels that are roughly 7 and 10 km long close to the western fjord wall (north-west corner of Figure 2.2G-L). An additional 7 km long channel can be seen 5 km away from the eastern fjord wall (center north of Figure 2.2G-L). Discharge at the grounding line for the two western channels reaches a maximum of $\sim$100 m^3/s each, and the central-eastern channel has a maximum discharge of $\sim$300 m^3/s in 2018. In the center of the glacier there is a longer channel segment, which does not continue all the way to the grounding line, but instead intersects with the region of sustained increased hydraulic sheet thickness. Maximum discharge occurs when integrated meltwater runoff reaches its peak for the season (Figure 2.3A), after which point discharge decreases and the channels begin to close. By the end of the melt season (Figure 2.2L) channel size and discharge has more or less returned to their pre-melt season state (Figure 2.2G).

2.4.2 Ice velocity results

We compare the modeled and observed velocity in 2016-2018 (Figure 2.3C). Velocity increases until maximum runoff is reached on July 19th in 2016, August 1st in 2017, and August 7th in 2018 (Figure 2.3A). Velocity then decreases quickly back to winter values, reaching a steady state in September. Our model predicts a seasonal cycle further upstream of the grounding line than is observed. We see a distinct seasonal cycle 15 km upstream in the model results, which can be seen in Figure A.11C, where seasonal acceleration is not visible in observations. The region over which the lower limit on effective pressure is used during the ice flow simulations can be seen in Figure A.12. Notable dates and corresponding runoff fluxes are summarized in Table A.2.

We find that modeled velocity near the grounding line is sensitive to the selection of the minimum limit on effective pressure. The predicted velocity in 2016 changes from 1,700 m/yr to 1,350 m/yr when the minimum varies from 5 to 8% relative to ice overburden pressure (Figure A.9). With a threshold value of 6%, we match the observations well. If the minimum effective pressure is set higher, the model under-predicts the peak velocity; vice versa if the minimum is set too low, the peak velocity is overestimated. Importantly, however, the start and duration of the speed up are not affected by this parameter selection. We discuss implications of this parameter below.

Two additional simulations were run without subglacial hydrology to test the ability of other physical mechanisms to cause Petermann's observed seasonal acceleration. We examined seasonal forcing in sea ice buttressing and enhanced basal melt under the ice shelf, but neither were able to reproduce ice velocity observations. Results from these simulations can be seen in Figures A.20 and A.21.

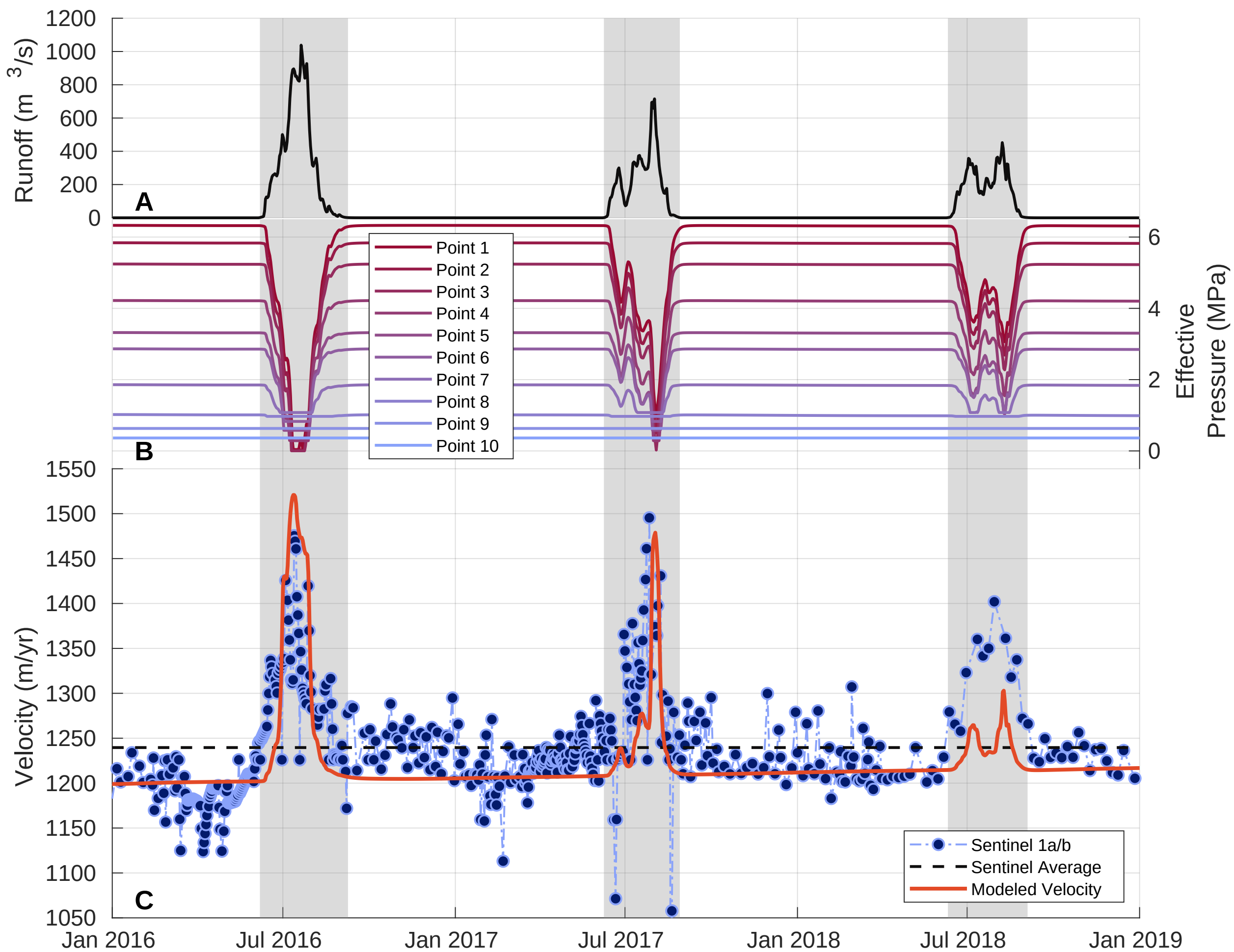

Figure 2.3: **Modeled seasonal ice acceleration of Petermann Glacier.** (A) Meltwater runoff integrated over the hydrology domain, (B) time-series of effective pressure adjusted to include the lower limit of 6% of ice overburden pressure at 10 locations spaced by 4.75 km along a central flow line from near the grounding line (pale blue) to 40 km inland (dark red). (C) Modeled velocity (red line) of Petermann Glacier, Greenland, and observations from the Sentinel 1a/b satellite data (blue dots) in 2016-2018 at a point near the grounding line (see Figure 1B for location).

2.5 Discussion

Our results suggest that Petermann's ice velocity is sensitive to subglacial hydrologic variability driven by changes in surface meltwater production, which percolates through the glacier to the bed. Overall, the modeled seasonal ice velocity matches the satellite observations well with respect to the timing and duration of the acceleration over the three consecutive years examined. The model success indicates that changes in subglacial hydrology are sufficient to explain the seasonal acceleration of Petermann Glacier.

We see a narrow region along the grounding line on the western side of the glacier where the subglacial water sheet thickness remains elevated throughout the three year time period, without significantly reducing between summers. The water pressure calculated by GlaDS in this region is continuously around 98% of ice overburden pressure, but never exceeds overburden. A recent study that uses satellite observations to monitor Petermann's grounding line migration shows an extensive retreat of nearly 5 km in this same region (Millan et al., 2022). The observed grounding line retreat is not uniform across the full extent of the fjord, and is less than 1 km as compared to the observed 1996 grounding line in some places. However, we see sustained high water pressures and elevated sheet thickness in our hydrology model results which align with the region that experienced the most extensive recent grounding line retreat. The authors attribute the retreat to infiltrating warm ocean water causing enhanced melting after noting that this is a region where the bed is topographically depressed (Millan et al., 2022). Our model results independently indicate that this region is very near flotation continuously throughout the year, which supports their interpretation of a sustained retreat from the previously stable grounding line position.

The subglacial hydrologic system has been connected to increased rates of basal melt on Petermann by direct measurements of surface meltwater runoff concentrations within one of the central sub-ice-shelf channels (Washam et al., 2019). Meltwater runoff concentrations peak within the channel roughly one month after the onset of above freezing air temperatures, which is interpreted as the time required for meltwater to travel through the subglacial hydrologic system and flow along the ice shelf base to the point of data collection 16 km downstream of the grounding line. These observations are consistent with our model's prediction of how the hydrologic system evolves for Petermann: we observe about a one month lag (see Figure 2.3A, Table A.2) between the onset of the melt season and maximum integrated meltwater runoff, which coincides with the maximum discharge predicted in our results (see Figure 2.2J). We also have agreement with the observation that surface runoff was observed below the ice shelf months after the 2016 melt season had ended, reaching a minimum concentration in February 2017 (Washam et al., 2019). This was attributed to meltwater slowly draining the subglacial hydrologic system. We see elevated thickness of the subglacial hydrologic sheet (Figure 2.2Q-R), and large sustained rates of discharge at the grounding line (Figure 2.2J-L) after the melt season has ended. Our modeled channels slowly decrease throughout the winter, with remnant meltwater continuing to discharge across the grounding line into the winter.

Channel discharge across the outflow boundary is not uniform in our hydrology model results, but rather spikes in regions of enhanced channelization near the grounding line. Approximate locations where we see the largest discharge values along the grounding line are at 1, 3-5, 7.5, 9-11, and 15.5 km as measured from the eastern fjord wall along the grounding line (Figure 2.2J). Channel discharge at these locations exceeds 100 m^3/s at the peak of the 2018 melt season, and the maximum discharge along the grounding line was nearly 350 m^3/s at 1 km from the eastern fjord wall. Observed sub-ice-shelf channels within 10 km of Petermann's grounding line are identified on its floating shelf (Rignot and Steffen, 2008). The observed locations of ice shelf channels generally align with where GlaDS predicts the largest subglacial channels along the grounding line to be. The ice elevation data used to show sub-shelf channel locations also shows significant thinning within 3 km of the western fjord wall (Rignot and Steffen, 2008), which is a highly channelized region in our results (northwest corner of Figure

2.2G-L), and was identified to have large non-hydrostatic crevasses penetrating ∼150 m into the ice, where ice thickness is about 400 m (Münchow et al., 2014). Colocation of crevasses and subglacial channels may be the result of enhanced basal melt rates in highly channelized regions of the grounding line leading to thinner ice with reduced restraining forces that is more susceptible to fracture (Watkins et al., 2021). The channels developed by our model are the most prominent in regions close to both fjord walls, (center-north and northwest corner of Figure 2 panels G-L). We suspect that Petermann's ice-shelf channels are initiated by subglacial channels, as has been suggested by others (Le Brocq et al., 2013; Sergienko et al., 2013), but our results are not sufficient to conclude this. Alternatively, ice shelf channels could be initiated by flow over protrusions in basal topography, locally thinning the ice and creating sinks for water discharged along the grounding line. Relatively small irregularities in ice thickness are propagated by enhanced melting from buoyant plume water resulting in large ice shelf channels farther away from the grounding line (Gladish et al., 2012).

Petermann Glacier is not the only glacier which experiences summer time speed up. A previous study (Moon et al., 2014) identified 55 marine terminating glaciers across different regions of Greenland, which exhibited seasonal fluctuations in ice velocity. The authors classified 3 distinct patterns of seasonal variability, one which is associated with changes in ice front position, and two controlled by meltwater runoff. The 2 glacier types controlled by runoff are distinguished by the subglacial hydrology either developing an efficient network of drainage channels early in the melt season or not. Glaciers that develop efficient drainage networks reach a minimum annual velocity in the late summer, which recovers during the winter and spring (type 3). Glaciers which do not develop an efficient system experience a maximum velocity during the summer and exhibit a relatively stable velocity during the rest of the year (type 2). Although Petermann Glacier was not part of that study, our velocity results match type 2, i.e. no efficient drainage network (Moon et al., 2014). How Petermann responds to future climate warming will, in part, depend on how efficiently it drains runoff. Climate change projections indicate that a larger area of the Greenland Ice Sheet will experience a melt season, and that summer melt seasons will begin earlier and last longer (Mernild et al., 2011; Tedesco et al., 2013; Välisuo et al., 2018). If Petermann currently develops an efficient drainage network, which seems unlikely given the magnitude of modeled effective pressure, then perhaps there will be minimal impact on seasonal acceleration with additional meltwater runoff moving easily through the subglacial system. However, if Petermann does not yet develop an efficient drainage network, or if it is efficient only in certain regions, we may see an increase in the magnitude of seasonal speedup or possibly the emergence of an entirely different velocity cycle.

A lower limit on effective pressure was required to avoid large areas with no basal resistance from the bed, which lead to unrealistically large velocities. We selected 6% of overburden pressure after testing (Figure A.9). Given the one-way coupling of our model configuration, the negative feedback between velocity and effective pressure is not incorporated into the ice dynamics (Hoffman and Price, 2014). Summer acceleration may reduce water pressure (i.e., increase N), which could then reduce velocity and damp the initial response. This may reduce the need for a lower limit on N. A fully coupled model configuration would be necessary to properly examine this relationship, but as a first step we ran our hydrology model with sliding velocity increased by 15% uniformly. Results showed that increasing sliding velocity alone was not sufficient to remove the lower limit on N (Figure A.17). Negative effective pressure values were also calculated in a different study using a fully coupled model of Store Glacier (Cook et al., 2022), so we may see $N < 0$ even if the feedback on velocity is represented. Introducing a time-variable hydraulic conductivity may help to reduce the dependency on the N limit, as reduced winter conductivity has been shown to produce a better match to winter time observations of water pressure (Downs et al., 2018). Allowing conductivity to grow as the hydraulic system evolves during the melt season could allow more water to move quickly through the system in high melt years while retaining enough water within the system in low melt years to develop a seasonal response to runoff entering the system.

Alternatively, it may be important to accurately place moulin locations. If a larger fraction of meltwater runoff is injected into a small subset of moulins at known locations from satellite data, perhaps channels in those regions would be able to efficiently remove enough runoff to reduce the need for an effective pressure limit without necessarily increasing the sheet conductivity parameter such that the model consistently under-predicts peak speed in low melt years. We tested our model using 3 different numbers of moulins to transport melt to the bed: 36, 15, and 0. When moulins are not present, melt is transported directly from the surface to the bed without first being funneled into a point source location. Results from all three simulations under-predicted acceleration in 2018 and required the N limit to match peak velocity in 2016 (Figures 3, A.18, and A.19). We therefore think that incorporating accurate moulin locations into the hydrology model seems unlikely to remove the dependency on an effective pressure limit, but further work is required to be sure.

The glacier bed is not perfectly smooth, so bedrock topography is expected to provide some resistance to flow even when GlaDS predicts a large area at zero effective pressure. Friction laws were not designed for cases where water pressure approaches and exceeds ice overburden pressure in magnitude (i.e. $N \leq 0$). For a regularized coulomb friction law, $N = 0$ yields a singularity and for the Budd friction law it forces basal drag to zero (Brondex et al., 2017; Schoof, 2010). Physically, it is unlikely for τ_b to get infinitesimally small over the bulk of the glacier's fast flowing region, which is what happens when N is allowed to be zero in current formulations of friction laws. Until recently, ice flow had not been coupled to hydrology in models. As such, friction laws that only consider $N > 0$ were reasonable for the applications in ice dynamics previously being considered. Now that hydrology models are being coupled to ice flow models, the inability of friction laws to be applied when water pressure exceeds ice pressure is a limitation of the current state of ice dynamics modeling. We interpret the necessity of a lower limit on N to be the result of small scale processes being interpreted onto a large scale mesh using equations which were not designed to consider hydrologic dynamics.

2.6 Conclusions

We find that short time scale seasonal acceleration of ice velocity of Petermann Glacier can be explained by changes in subglacial hydrology, wherein surface meltwater runoff moderates basal friction through the evolution of the subglacial hydrologic system over the course of the melt season. We reproduce the observed ice velocity from satellite data with the correct magnitude, start and duration of acceleration. Warmer atmospheric temperatures will likely increase runoff production and produce a longer melt season which begins earlier in the year. Since Petermann's seasonal speed up coincides with the production of runoff, we expect the speed up to start sooner in future years. However, the duration of the speed up and its maximum amplitude may vary and not necessarily increase with additional runoff. This sensitivity of the glacier speed to runoff will need to be studied in more detail. Meanwhile, this study demonstrates that changes in subglacial hydrology are capable of producing a substantial impact on the seasonal flow of a major Greenland glacier.

Chapter 3

Sea level rise projections of Petermann Glacier, Greenland, modeled using synchronously coupled subglacial hydrology and ice flow dynamics

3.1 Abstract

Greenland ice shelves are known to display seasonal speedups of ice velocity which can be attributed to ice front position or to meltwater runoff, depending on which glacier is being examined. However, it remains uncertain if the seasonality of glacier speed will be impacted by climate change in the coming century. Current projections of glacier dynamics under 21st century climate forcings do not include subglacial hydrology, so it also remains unknown if

it will play any important role in evolving glacier dynamics under different climate change scenarios, or ultimately have an impact on sea level rise projections. Here we present a model with synchronous coupling of ice dynamics and subglacial hydrology applied to Petermann Glacier in northern Greenland. Petermann exhibits a summer-time acceleration of roughly 15% as compared to its baseline winter velocity, which is likely the result of subglacial hydrology. Although it has been relatively stable in recent years, as one of the largest marine terminating glaciers in northern Greenland, whether or not Petermann remains stable will have a significant impact on the sea level contribution of the northern sector of the ice-sheet. We use climate through 2100 to investigate how the subglacial hydrologic system may evolve in a warmer climate and to test if including hydrology changes the stability of Petermann under future climate scenarios using the Ice-sheet and sea level System Model (ISSM) which includes the Glacier Drainage System (GlaDS) model. We compare glacier evolution and projected sea level rise for three model configurations: one with synchronously coupled subglacial hydrology and ice dynamics, a second with asynchronous coupling where subglacial hydrology is calculated with static ice geometry and velocity but ice dynamics are calculated using effective pressure from GlaDS output, and a third where subglacial hydrology is excluded entirely from the model setup. Results show a significant increase in projected sea level rise by the end of the century and differing patterns of grounding line migration and ice thinning when subglacial hydrology is included in the model configuration for Petermann.

3.2 Introduction

Petermann Glacier is one of the largest Greenlandic glaciers, and as such it has the potential to contribute significantly to the total sea level rise from the GrIS (Mouginot et al., 2019; Morlighem et al., 2014). Enhanced basal melting (Khan et al., 2014), terminus retreat (Choi et al., 2021), grounding line migration (Pelle et al., 2021), and enhanced surface melting (Rignot et al., 2011) all impact ice velocity and total ice discharge, both of which play key roles in determining the total mass loss and overall contribution to sea level rise of the ice sheet (Mouginot et al., 2015). Reducing uncertainties associated with how these various processes contribute to and influence the dynamic mass loss of glaciers will improve the accuracy of sea level rise predictions.

Although various state of the art subglacial hydrology models have been developed at this point, their availability to the glaciology community is still relatively new as compared to other tools in the field (De Fleurian et al., 2014; Sommers et al., 2018; Werder et al., 2013). The coupling of subglacial hydrology models to ice flow models is a recent advancement in glacier modeling capabilities (Cook et al., 2020; Ehrenfeucht et al., 2023). Even more recent is the ability to run two-way coupling between the systems (Cook et al., 2022), wherein subglacial hydrology informs ice flow, which then in turn informs subglacial hydrology, allowing the two systems to evolve dynamically over the course of the simulation. To date, there are only a handful of publications that have utilized this development to ask questions related to the ability of subglacial hydrology to influence ice dynamics.

To test the hypothesis that subglacial hydrology contributes to sea level rise by altering long term ice dynamics, we run a suite of simulations representing how Petermann might evolve over the 21$^{\text{st}}$ century in response to climate change. Two different climate change scenarios are utilized; one high and one low emissions projection. Subglacial hydrology is represented in our model simulations in two different ways or excluded entirely as a means to isolate the impact of hydrology on long term stability and mass loss from the other physical processes represented in the model. A more complete understanding of how subglacial hydrology and ice flow dynamics interact will fill some of the knowledge gaps remaining in glaciology. Evaluating the capability of subglacial hydrology to impact the glacier dynamics governing ice flow and discharge will ultimately contribute towards a more accurate calculation of projected sea level rise from glaciers in Greenland.

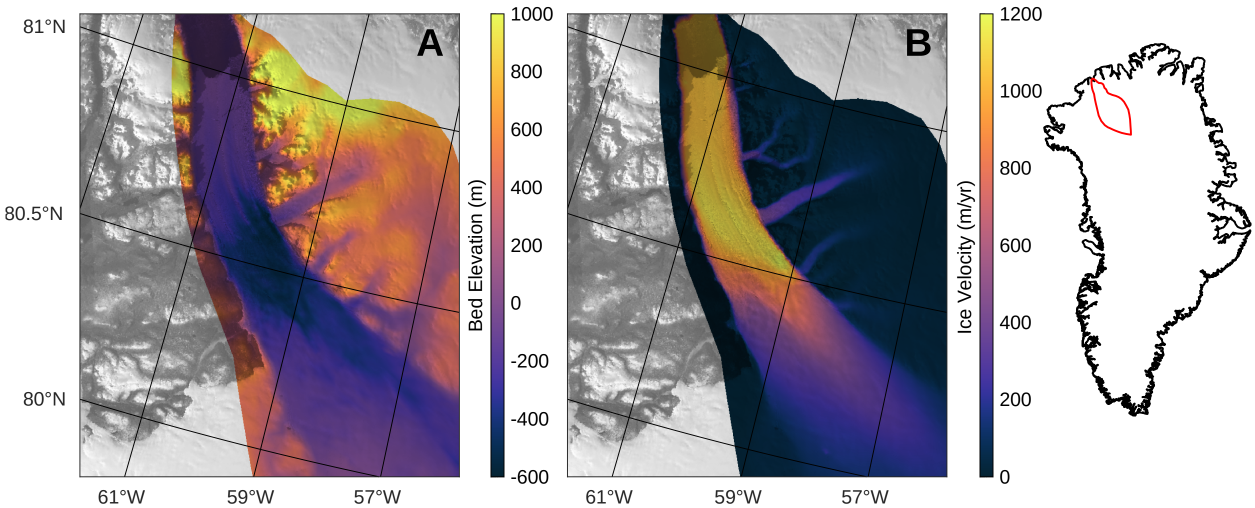

Figure 3.1: **Coupled modeling environment of Petermann Glacier.** (A) Bed elevation of Petermann Glacier, Greenland, from BedMachine Greenland v4 (Morlighem, 2021) is inferred from mass conservation (Morlighem et al., 2017) and (B) ice surface velocity (Joughin et al., 2010) derived from satellite observations. The black outline shows the ice extent around Greenland from BedMachine, and our model domain outline is marked in red.

3.3 Data and Methods

3.3.1 Subglacial hydrology and ice sheet models

We use the Glacier Drainage System (GlaDS) model (Werder et al., 2013) and the Ice-sheet and Sea-level System Model (ISSM; Larour et al. (2012)) to examine the impact of subglacial hydrology on glacier velocity for Petermann. One model domain is used for both models and in all coupling configurations. It extends from the glacier's ice front nearly 500 km inland to the ice divide, including the rocky cliffs of the fjord side walls. The two-dimensional model domain is discretized using an anisotropic mesh of 12,693 elements. Element size varies according to the gradient in velocity and ranges from 500 m in regions of fast flowing ice to 5 km upstream where ice is slow and the gradient is small. We use the two-dimensional Shelfy-Stream Approximation of the Stokes equations as our ice flow law (MacAyeal, 1989), and implement an adaptive time step in all simulations that calculates an appropriate time step according to a Courant-Friedrichs-Lewy condition. We set a minimum time-step at fifteen minutes, and a maximum of 6 hours in all of our model runs.

3.3.2 Representations of subglacial hydrology

In our model setup, we employed both asynchronous and synchronous coupling between subglacial hydrology and ice dynamics. In the asynchronously coupled configuration, we run GlaDS alone, without a dynamic connection to ice ISSM. Effective pressure, N, is an output of the GlaDS model, and is defined as the difference between the ice overburden pressure and the basal water pressure. A time series of effective pressure spanning the entire model domain from the year 2000 to 2100 is incorporated as an additional forcing parameter in ISSM, which then runs with spatially and temporally varying effective pressure utilized to calculate ice flow. This configuration will also be referred to as 1-way coupling for short hand.

In the synchronously coupled model configuration, also referred to as 2-way coupling, subglacial hydrology and ice dynamics are both updated at each time step during the full model simulation. This allows effective pressure calculated by GlaDS to immediately influence ISSM's calculations of surface velocity and ice geometry. Changes in these fields are then fed back into GlaDS to calculate the new effective pressure using the updated ice velocity and geometry values. A schematic representation of the connections between the two glacier models under the two coupling configurations can be seen in Figure 3.2.

In addition to the different model coupling approaches of subglacial hydrology and ice dynamics, we also run simulations that fully exclude subglacial hydrology from simulations of Petermann's evolution during the 21st century. This gives us the ability to examine (1) if hydrology's impact on ice velocity alters Petermann's long term ice dynamics and contribu-

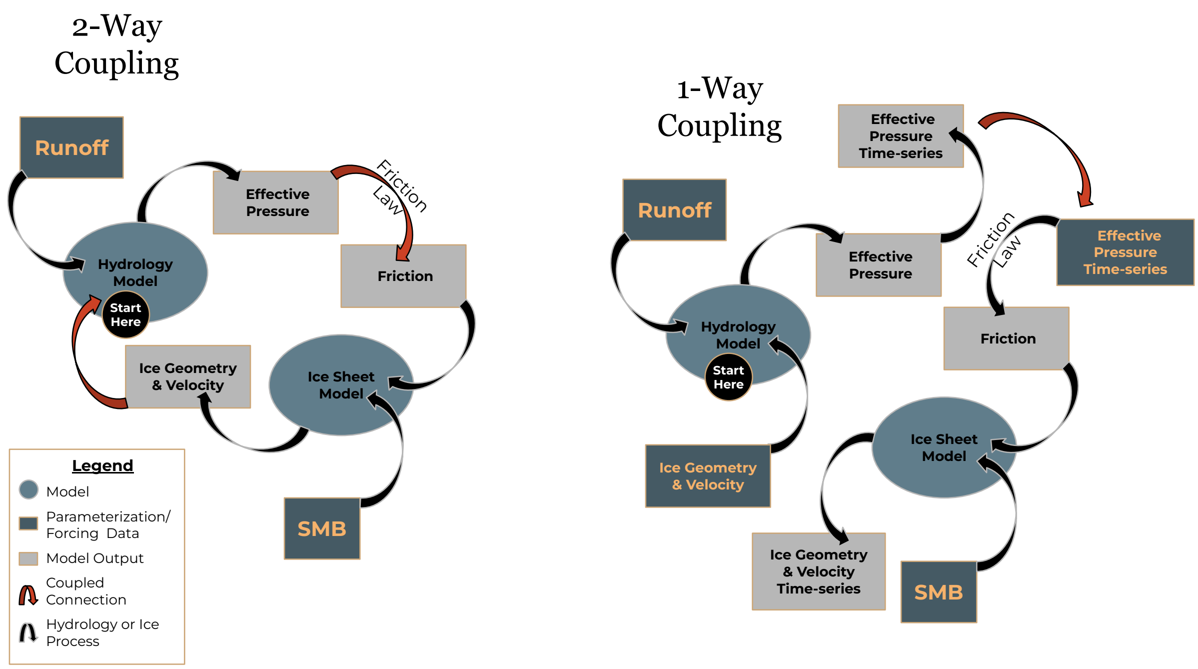

Figure 3.2: **Schematic representation of synchronous coupling (2-way) versus asynchronous coupling (1-way) of subglacial hydrology and ice flow models.** Effective pressure output from the hydrology model is used by the ice flow model as one of the parameters that is used to calculate basal friction either as an offline input (1-way coupling) or dynamically during one simulation (2-way coupling).

tion to sea level rise, and (2) if the feedback from ice velocity back to subglacial hydrology mitigates any initial effect of hydrology on the long term dynamics.

3.3.3 Climate change scenarios and forcing data

We conducted simulations to investigate the future projections of Petermann Glacier, Greenland, under two climate change scenarios from the Climate Model Intercomparison Project Phase 6 (CMIP6). We use climate forcing data from two Shared Socio-economic Pathways (SSPs): SSP 1-2.6, representing a low emissions scenario, and SSP 5-8.5, representing a high emissions scenario (Eyring et al., 2016; O'Neill et al., 2016). These scenarios are widely used in climate research to explore different plausible narratives that outline various developments of the global community and associated greenhouse gas emissions. SSP 1.26 represents

Table 3.1: **GlaDS Model Parameters**

Symbol	Description	Value	Units
e_v	Englacial void ratio	10^{-5}	-
c_t	Pressure melt coefficient	7.5×10^{-8}	K Pa^{-1}
L	Latent heat of fusion	3.34×10^{5}	J kg^{-1}
A	Ice flow constant	2.5×10^{-25}	Pa^{n} s^{-1}
n	Glen's flow constant	3	-
g	Gravitational acceleration	9.81	m s^{-2}
h_r	Bedrock bump height	0.1	m
l_r	Cavity spacing	2.0	m
k_s	Sheet conductivity	0.02	$m^{7/2}$ $kg^{-1/2}$
k_c	Channel conductivity	0.2	$m^{3/2}$ $kg^{-1/2}$

a global shift towards sustainability. This requires net zero carbon emissions by the year 2075 and equates to 1.8°C of atmospheric warming by the year 2100, whereas SSP 5-8.5 represents further fossil fuel development in the coming decades in a "business as usual" line of course. This scenario would reach 3× current carbon emissions by the year 2075 and is associated with 4.4°C of warming by 2100.

We utilized SMB and runoff data obtained from projections generated by the regional climate model MAR (Fettweis et al., 2013) and specific datasets (Hofer et al., 2020) to drive all of our model simulations. These datasets relied on output from the Community Earth System Model (CESM), which is one of the state-of-the-art climate model (Kay et al., 2015) that participated in CMIP6 (Danabasoglu et al., 2020). Under the high emissions scenario, we observed a significant negative trend in SMB by the end of the century, accompanied by a nearly quadrupled meltwater runoff by 2100. In contrast, the low emissions scenario displays relatively consistent patterns of SMB and runoff compared to current observations.

3.3.4 Friction laws

Basal friction plays a crucial role in glacier ice flow, as it governs interactions between the ice and its underlying bed, which influences the overall dynamics and behavior of the glacier.

However, there is no consensus on how friction is best represented in ice flow models. Friction laws define the relationship between ice velocity and the driving stresses. By incorporating the effects of shear stress, bed roughness, subglacial hydrology, and other factors, friction laws provide a means to represent the complex processes that occur at the ice-bed interface. However, due to the inaccessibility of the bed for direct measurement and to the spatial and temporal variability of basal friction, there is no consensus on a best representation of friction in models. As such, many different friction laws exist taking a variety of forms that incorporate various parameters. The choice of friction law can significantly impact the modeled results, and different laws may yield distinct predictions of ice flow patterns, rates of ice loss, and the sensitivity of glaciers to environmental changes. To account for the uncertainty surrounding how to most accurately represent basal friction in ice flow models, we employed two of the most commonly used friction laws that utilize effective pressure: the Budd friction law (Budd et al., 1979) and the Schoof friction law (Joughin et al., 2019; Schoof, 2005), repeated here for reference.

We use the linear version of the Budd friction law:

$$\boldsymbol{\tau}_b = C_B^2 \boldsymbol{v}_b N, \tag{3.1}$$

where $\boldsymbol{\tau}_b$ is basal shear stress, $\boldsymbol{v}_b$, N is effective pressure, and C_B is a coefficient. There is no upper limit incorporated into the Budd friction law, allowing for shear stress to reach arbitrarily large (Brondex et al., 2017).

We also use a regularized coulomb friction law (Gagliardini et al., 2007; Schoof, 2005; Joughin et al., 2019), which we will refer to as the Schoof friction law:

$$\boldsymbol{\tau}_b = -\frac{C_S^2 \left|\boldsymbol{v}_b\right|^{m-1} \boldsymbol{v}_b}{\left(1 + \left|\boldsymbol{v}_b\right| \left(\frac{C_S^2}{C_{\max} N}\right)^{\frac{1}{m}}\right)^m}, \tag{3.2}$$

where C_S is the friction coefficient associated with the Schoof friction law, $m = 1/n$, where we take $n = 3$ as the flow law exponent (Glen, 1958). $C_{\max}$ is a positive value corresponding to the maximum value of $\boldsymbol{\tau}_b/N$, which is bounded by the local maximum up-slope of the bedrock (Gagliardini et al., 2007). There are two distinct flow regimes associated with Schoof friction. For large values of effective pressure, the Schoof friction law reduces to $\boldsymbol{\tau}_b \sim C_S \boldsymbol{v}_b^m$, which is a Weertman-type friction regime (Weertman, 1957), where basal shear stress is determined by sliding velocity. For small values of N, water filled cavities open, and the apparent roughness of the rigid bedrock is decreased, reducing the friction law to $\boldsymbol{\tau}_b \sim C_{\max} N$, which is referred to as an Iken bound (Iken, 1981). This case exhibits glacier flow with characteristic plastic basal rheology (Brondex et al., 2017), which is considered appropriate for glaciers flowing over soft beds (Tulaczyk et al., 2000).

3.3.5 Model parameterization and initial conditions

We initialize the model with inversions for both rheology and the friction coefficients (Morlighem et al., 2010). The initial velocity field closely matched observations, with a maximum misfit of approximately 12%. To insure that simulations run using different friction laws begin from a similar initial state, we analytically calculate the Budd friction law coefficient, C_W, from the inverted Schoof friction law coefficient, C_S, as has been done in other studies (Choi et al., 2022). Initial ice velocity, geometry, and basal shear stress are all equivalent going into the model spinup for both friction laws. We parameterize ocean forcing using a depth dependent linear melt rate that has been used previously to model Petermann (Åkesson et al., 2021) and other Greenlandic glaciers (Choi et al., 2017), and is consistent with modeling and observations of melt rates under Petermann's floating ice (Cai et al., 2017; Rignot and Steffen, 2008). We set the maximum melt rate to 30 m/yr at a depth of 600 m and a minimum melt rate of zero at 200 m such that no basal melt is applied to floating ice shallower than 200 m and the maximum melt rate is applied to all floating ice deep than 600 m.

We first spin up the ice dynamics for 20 years, allowing the model to reach a steady state for ice geometry, surface velocity, and grounding line position. At this point the subglacial hydrology model is parameterized. We use an initial condition of 0.03 m for the hydraulic sheet thickness and $0.5 \times P_{ice}$ for the hydraulic potential, both of which help with model stability. There are two separate conductivity parameters used in GlaDS, one for the hydraulic sheet, and one for the channels. We use a sheet conductivity value of 1.5×10^{-2} $m^{7/2}kg^{-1/2}$ and a channel conductivity of 5.0×10^{-2} $m^{3/2}kg^{-1/2}$ based on model tuning. Additional hydrology parameters can be found in Table 3.1. We use a Neumann flux boundary condition everywhere except the grounding line. We assume the floating ice shelf is in perfect hydrostatic equilibrium such that at the grounding line $\phi = 0$ (Cook et al., 2022), as well as for all floating ice elements. We run the model with synchronously coupled subglacial hydrology and ice dynamics for 5 years, allowing for all variables to come to equilibrium, the results of which are used as the initial conditions for all transient simulations in our experiment.

3.4 Results

3.4.1 Sea level rise

The dominant factor in determining the magnitude of Petermann's sea level rise contribution is the climate change scenario. Each model configuration that used the CMIP6 SSP 5-8.5 high emissions scenario experienced nearly double the mass loss as the same model configuration

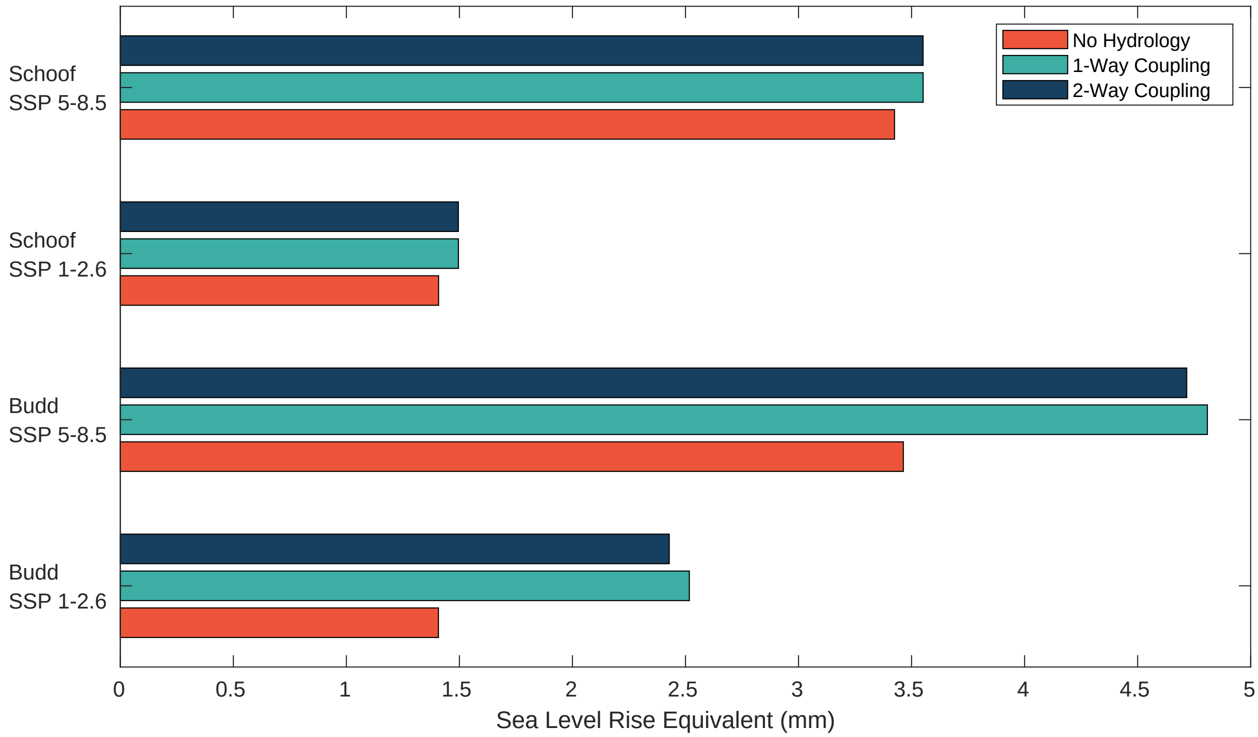

Figure 3.3: **Final projected sea level rise at the end of year 2100 for all 12 simulations.** Three different representations of subglacial hydrology are compared: the case where dynamic hydrology is fully excluded (red), asynchronous (1-way) coupling between ice dynamics and hydrology (teal), and synchronous (2-way) coupling (blue). All three model configurations are run using both a Budd and a Schoof friction law (y-axis). Two different CMIP6 climate change scenarios (y-axis) are used to force model simulations: SSP 5-8.5 (high emissions) and from SSP 1-2.6 (low emissions).

forced by the SSP 1-2.6 low emissions scenario (see Table 3.2). This resulted in the six simulations forced by SSP 5-8.5 having a predicted sea level rise contribution ranging from 3.42 to 4.72 mm by the year 2100. Whereas the other six simulations, forced by SSP 1-2.6, range from 1.41 to 2.43 mm at the end of the century (Figure 3.3, Table 3.2).

We find that including subglacial hydrology in future projections of Petermann increases the predicted sea level rise in all cases as can be seen in Figure 3.3. The impact of subglacial hydrology on sea level rise was much larger in the simulations that employed a Budd friction law rather than a Schoof friction law. Sea level rise for the Budd, high emissions scenario was 3.46 mm with no hydrology and 4.81 and 4.72 mm when hydrology was represented using 1 and 2-way coupling respectively. That amounts to a 38.8% increase using 1 way coupling and a 36.2% increase using 2 way coupling. Results for the Schoof, high emissions scenario showed a sea level rise of 3.42 mm with no hydrology included, and 3.55 mm for both model configurations including subglacial hydrology, which is equivalent to a 3.7% increase.

The low emissions scenario resulted in a lower net increase in sea level rise for simulations including hydrology, but a larger percent increase. When Budd friction was used, sea level rise increased from 1.41 mm to 2.52 (1-way coupling) and 2.43 mm (2-way coupling), which amounted to a 78.9% increase for 1-way coupling and a 72.6% increase for 2-way coupling. When Schoof friction was used, sea level rise increased from 1.41 mm to 1.5 mm (6.2% increase) for both representations of subglacial hydrology.

We see no significant difference between synchronously and asynchronously coupling subglacial hydrology and ice dynamics when Schoof friction is employed. In both the cases (high and low emission climate forcing scenarios), the final ice volume differs by less than 1 Gt. However, in simulations that used a Budd friction law, 2-way coupling results in about 0.1 mm less sea level rise than 1-way coupling between subglacial hydrology and ice flow. These values can be found in Table 3.2, along with the total volume change for each simulation.

3.4.2 Change in surface velocity and ice thickness

Surface velocities for all of the simulations except for those that used Budd friction and incorporated subglacial hydrology decreased by the end of the century (see Figure 3.4). The simulations that used a Budd friction law and either 1 way or 2 way coupling to hydrology (Figure 3.4 Panels E F I and J) accelerated over fast flowing grounded ice and across most of the floating ice shelf, while slowing down further upstream over the slower portions of the glacier. A larger magnitude of speed up is observed in the high emissions scenario, but the spatial pattern is consistent for both climate forcings.

Table 3.2: **Summary of model results:** the final sea level rise contribution of Petermann Glacier by the end of the 21st century is shown for model simulations using three different model configurations, two different parameterizations of basal sliding, and two different climate forcing scenarios. Additionally, total glacier mass loss is shown, as well as the contributions to mass loss by surface mass balance (SMB) and discharge (D). Note that positive SMB corresponds to accumulation of mass, while positive D corresponds to mass loss via calving and basal melt. The percent change of projected sea level rise is also shown for 1 and 2-way coupling model configurations as compared to the corresponding no hydrology simulation results.

		Friction Law			
		Budd		Schoof	
Hydrology	Output Variable	SSP 1-2.6	SSP 5-8.5	SSP 1-2.6	SSP 5-8.5
No Hydrology	Sea level rise (mm)	1.41	3.46	1.41	3.42
	Total volume change (Gt)	-425.04	-1069.79	-428.63	-1067.54
	Integrated SMB (Gt)	54.46	-663.54	54.46	-663.54
	Integrated D (Gt)	479.50	406.25	483.08	404.00
1-Way Coupling	Sea level rise (mm)	2.52	4.81	1.50	3.55
	SLR percent change	78.9%	38.8%	6.2%	3.7%
	Total volume change (Gt)	-736.55	-1422.75	-454.11	-1100.27
	Integrated SMB (Gt)	54.46	-663.51	54.46	-663.51
	Integrated D (Gt)	791.01	759.24	508.57	436.76
2-Way Coupling	Sea level rise (mm)	2.43	4.72	1.50	3.55
	SLR percent change	72.6%	38.2%	6.2%	3.7%
	Total volume change (Gt)	-710.73	-1396.65	-454.01	-1100.04
	Integrated SMB (Gt)	54.18	-663.90	54.18	-663.92
	Integrated D (Gt)	764.90	732.75	508.19	436.12

In contrast to this, the spatial pattern of surface velocity change is consistent for the Budd friction runs without subglacial hydrology and for all three model configurations using a Schoof friction law. Of these 8 simulations, changes in surface velocity can be attributed to the climate forcing. The final surface velocities of all three simulations using Schoof friction and forced by the low emissions scenario (Figure 3.4 Panels C, G, and K) and the simulation using Budd friction forced by the low emissions scenario (Figure 3.4 Panel A) have minimal differences. Similarly, the three simulations using Schoof friction forced by the high emissions scenario (Figure 3.4 Panels D, H, and L) plus the Budd, high emissions, no hydrology simulation (Figure 3.4 Panel B) also have minimal differences from one another. The simulations run using CMIP6 SSP 5-8.5 climate forcing data experience a larger magnitude slow down across the fast flowing portion of the glacier as compared to those that used SSP 1-2.6 climate forcings.

The general slow down of grounded ice observed in the majority of simulations is paired with significant thinning of Petermann's floating ice shelf and fast flowing grounded ice (Figure 3.5). Simulations that used Budd friction and included subglacial hydrology, which experience acceleration of surface velocities, also show ice thickening on the ice shelf and within 20 km of the grounding line (Figure 3.5 Panels E, F, I, and J). All simulations that used Schoof friction, and those that used Budd friction without Hydrology, exhibit thinning across the floating ice shelf that extends upstream of the grounding line several 10s of kilometers.

3.5 Discussion

The results from simulations with and without subglacial hydrology show that it is likely an important process in calculating ice loss for Petermann. The total sea level rise increased by the end of the century in all simulations including subglacial hydrology as compared to those that ignore the process. In simulations that utilized the Budd friction law, sea level rise increased significantly (>35%), and while the difference was much smaller in simulations that used the Schoof friction law, we still see an increased projected sea level rise of 3-6% by the end of the century. This suggests that projections that have previously left out this physical process may be underestimating sea level rise.

We find that the sensitivity of our simulations to the inclusion of subglacial hydrology is highly dependent on the choice of friction law. This is consistent with what other modeling

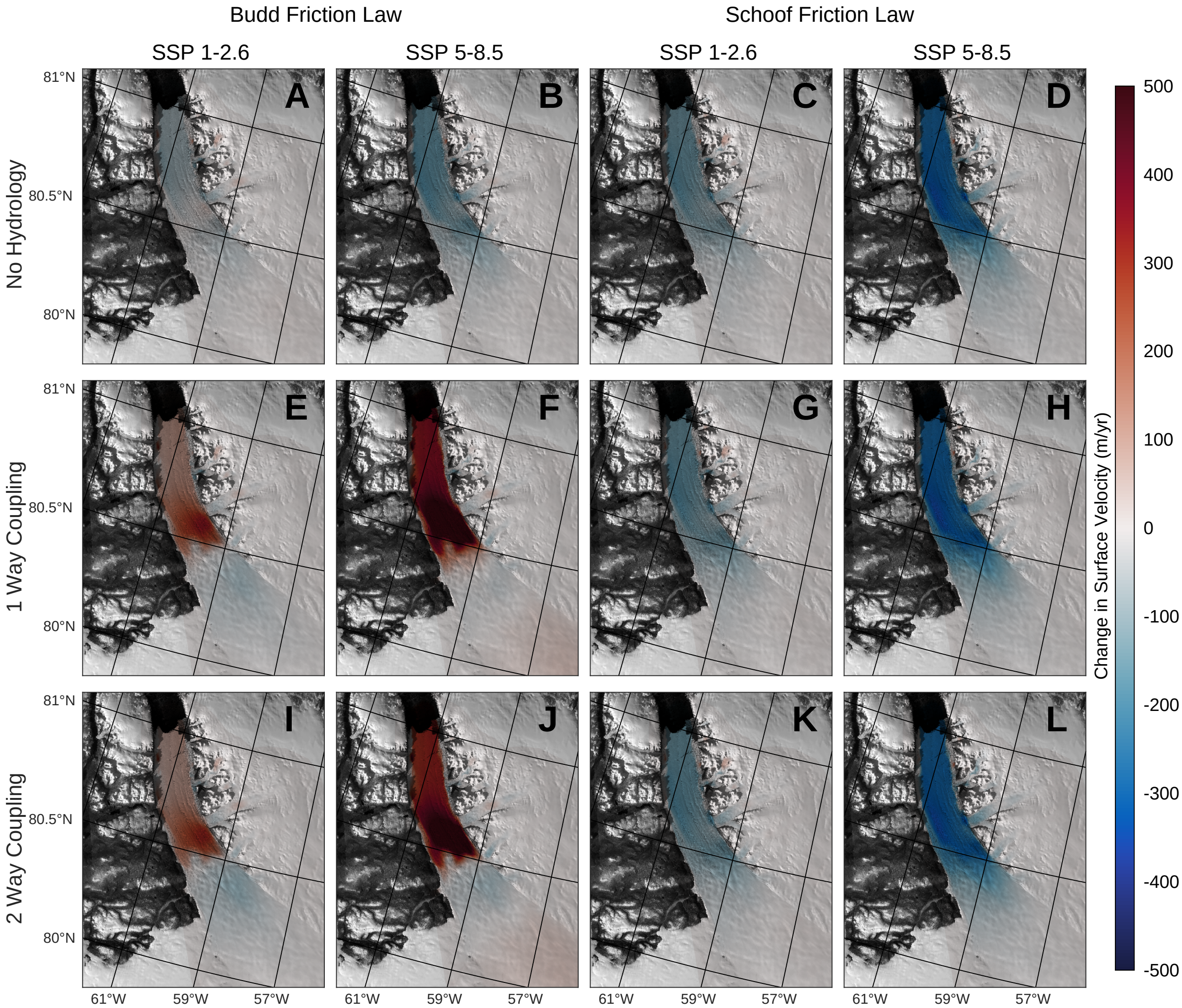

Figure 3.4: **Change in modeled ice surface velocity field** from 2000 to 2100. Positive values are associated with acceleration (red shading) and negative values indicate a slow down (blue shading) of ice velocity by the end of the century.

studies have found for other glaciers in both Greenland (e.g. Choi et al. 2022) and Antarctica (e.g. Brondex et al. 2019). Notably, a recent study (Åkesson et al., 2021) found that the projected evolution of Petermann is extremely sensitive to the choice of friction law. This study ran projections of Petermann's evolution to the year 2300 under 5 ocean warming scenarios. Unlike the work presented in this paper, the authors exclude atmospheric forcing, choosing to specifically focus on oceanic warming. Six different friction laws were examined, including Budd and Schoof friction laws. Effective pressure was defined according to Equation 1.2

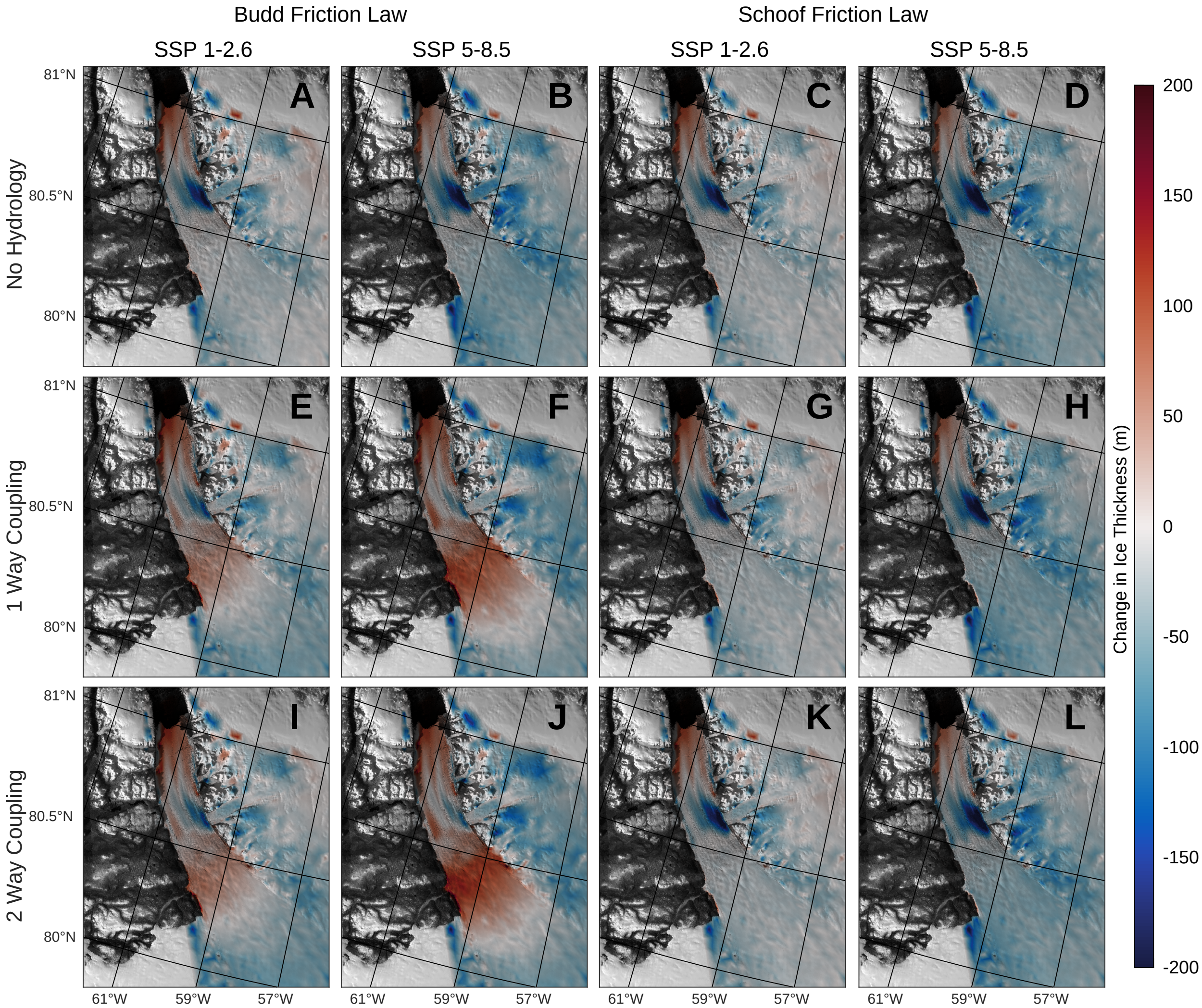

Figure 3.5: **Change in modeled ice thickness** from 2000 to 2100. Positive values indicate an increase in ice thickness (red shading) by 2100 and negative values indicate an overall trend of ice thinning (blue shading).

without the use of a full hydrology model to compute water pressure. As such, in their simulations, when effective pressure is required by the friction law, it is calculated purely based on initial ice geometry. The authors find significant differences in ice velocity, inland thinning of grounded ice, and grounding line retreat resulting from the choice of friction law. Differences between their Budd and Schoof future projections also produce different sea level rise projections for Petermann. They find a 1.97 to 2.53 mm sea level rise contribution by the year 2100 using Budd friction, and a 1.17 to 2.53 mm sea level rise using Schoof friction, depending on the magnitude of warming applied.

Interestingly, results from our no hydrology simulations show remarkably similar behavior using the two friction laws, with only marginally different total mass loss and projected sea level rise (Table 2). We only see notable differences from using different friction laws when subglacial hydrology is included. As we kept ocean forcing constant across all of our simulations, those excluding subglacial hydrology are being driven by SMB. By the end of the hundred year simulations, both Budd and Schoof friction caused a decrease in velocity and thinning, with the Schoof friction law causing a moderately larger slow down than Budd friction. The decrease in ice thickness caused a reduction in effective pressure which outweighed the impact of reducing velocity, causing basal shear stress to decrease for both cases. Overall, SMB driven ice dynamics were not particularly sensitive to the choice of friction law in our simulations.

In simulations that do include subglacial hydrology, Budd friction results in substantially more sea level rise than Schoof friction. When subglacial hydrology is represented, large seasonal changes in effective pressure alter ice dynamics over very short periods of time. The injection of meltwater runoff to the subglacial hydrologic system causes water pressure to rapidly increase, which lowers the effective pressure at the bed of the glacier. The impact of lowering effective pressure on basal shear stress is dependent on the choice of friction law. With the Budd friction law, we see a seasonal increase in τ_b in several locations within 10 km of the grounding line, and a reduction in basal shear stress from about 10 to 20 km inland of the grounding line across the main trunk of the glacier (Figure 3.6 Panel D). The spots where shear stress increases using Budd friction experience a reduction in shear stress using Schoof friction (Figure 3.6 Panel E), with the rest of the model domain experiencing a negligible seasonal change. The reduction with Schoof is caused by the value of the Iken bound decreasing. Schoof friction has an upper limit on shear stress that is determined for a given value of N, where $\tau_b/N < C_{max}$. Since N becomes smaller with increased seasonal water pressure, the maximum value that τ_b can take becomes smaller as well. We see that in the winter, basal shear stress is near its maximum value in several spots along the fast

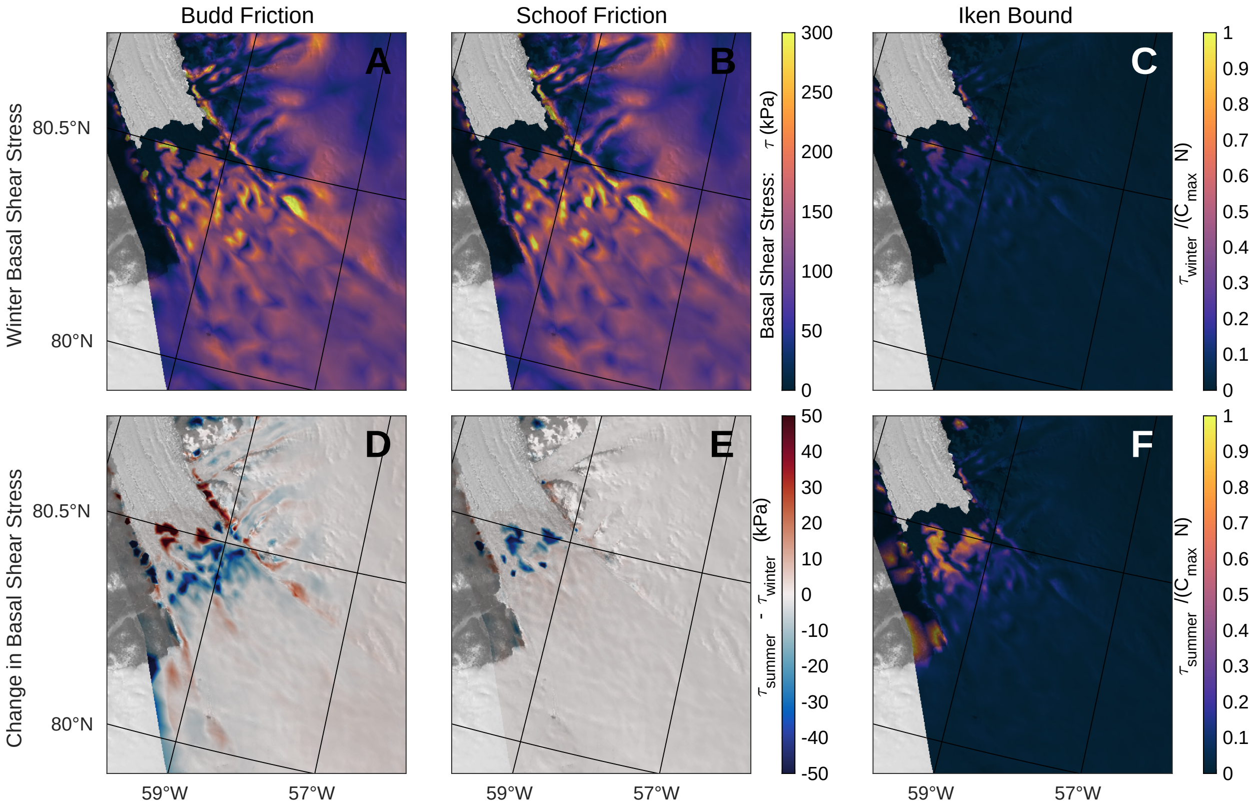

Figure 3.6: **Seasonal change in basal shear stress, τ_b,** using different parameterizations of basal sliding. Winter values of τ_b are very similar using both (A) a Budd friction law and (B) a Schoof friction law. Schoof friction includes (C) Iken's bound: a limit on τ_b when N is small such that $\tau_b \sim C_{\max}N$. Summer time meltwater runoff reduces effective pressure at the glacier bed in both cases, resulting in seasonal changes of τ_b using both (D) Budd friction and (E) Schoof friction. (F) Iken's bound limits seasonal increases in tau_b for simulations using Schoof friction.

flowing portion of the glacier (Figure 3.6 Panel C). In the summer, the area over which tau is close to its limit increases (Figure 3.6 Panel F), and τ reaches the Iken bound in several places. Locations where the Iken bound is reached align with locations where we see the seasonal reduction in tau (Figure 3.6 Panel E).

Generally speaking, we expect to see faster ice velocities when either effective pressure decreases or basal shear stress increases using either friction law. In actuality, changes in the driving stress of a glacier reflect the balance between changes to both velocity and effective pressure, both of which can exhibit a range of behaviors. In the Budd formulation of friction, there is no upper limit on the magnitude of shear stress as effective pressure becomes small. We see both positive and negative changes to shear stress as the result of subglacial hydrology, and a wide spread acceleration. The surging behavior acts to discharge a larger volume of ice, which accumulates over the century and ultimately results in more ice loss and larger sea level rise as compared to simulations using Schoof. The Iken bound in the Schoof friction law limits basal shear stress in regions of low effective pressure. This moderates the velocity response as effective pressure gets smaller in the summer. A smaller region of the glacier experiences seasonal speedup, and the magnitude of the speedup is more sensitive to annual runoff than for Budd friction. This results in increased discharge as compared to when no hydrology is included, but a smaller increase than we see with Budd friction.

Given that we use a simple depth-dependent basal melt parameterization that is static in time to account for ice shelf undercutting, the sea level rise projections calculated here are representative of projected sea level rise from climate forcings alone, and do not account for the enhanced thermal forcing from the ocean. Ocean temperatures were observed to increase in the Nares Strait by 0.023 ± 0.015°C between 2003 and 2009 alone (Münchow et al., 2011), and by the year 2100, the temperature in the Arctic ocean is projected to increase by ¿1°C up to 800 m deep (Cheng et al., 2022). Here we aim to tease apart the impact that excluding the physics of subglacial hydrology on ice velocity and ice thickness has on projected mass loss based on enhanced climate forcing. However, freshwater discharge across the grounding line is very likely an important component of ice shelf melting (Hewitt, 2020) as well the dynamics examined here. Basal melting of floating contributes substantially to the Greenland Ice Sheet's mass balance. By ignoring it, we are likely underestimating Petermann's total sea level rise contribution, but are able to disentangle the impact that subglacial hydrology is having on mass loss driven by atmospheric forcing from changes in SMB. There is evidence that including discharge in calculations of basal melt reduces the model mismatch to observations (Nakayama et al., 2021; Wei et al., 2020), and also that the volume loss of floating ice increases (Cai et al., 2017; Dow et al., 2020; Gwyther et al., 2023; Sergienko et al., 2013), and grounding line retreat is enhanced (Robel et al., 2022;

Wilson et al., 2020). Understanding the full impact of subglacial hydrology on sea level rise will require further study and careful consideration of both atmospheric and oceanic climate forcings. However, the work presented here illustrates capability for evolving subglacial hydrology to drastically alter modeled projections, and the need for further research to fully understand these physics.

3.6 Conclusions

21st century sea level rise projections have been made on a variety of spatial scales, using different ice flow models, and incorporating various different physical processes. However, subglacial hydrology has not been considered in the calculation of future sea level rise in most cases due to the technological and computational difficulties associated with combining the use of subglacial hydrology and ice flow models. Here we address this gap by applying two coupled model frameworks to Petermann at a full drainage basin scale connecting subglacial hydrology to ice dynamics. One in which subglacial hydrology is coupled to ice flow asynchronous by calculating effective pressure offline using the GlaDS model and then manually adding it to ice flow simulations in ISSM, and a second in which hydrology and ice flow are synchronously coupled, allowing both to influence the other. We find that the inclusion of subglacial hydrology in future projections of Petermann increases the total sea level rise predicted by the end of the century in all cases. However, the magnitude of sea level rise from subglacial hydrology's impact on ice dynamics is highly dependent on the choice of friction law. This is the first application of a synchronously coupled framework between GlaDS and ISSM.

Chapter 4

Modeled sea water intrusion in the observed grounding zone of Petermann Glacier causes extensive retreat

4.1 Abstract

Understanding the dynamics of glacier grounding line migration is critical for projecting marine terminating glacier evolution and their contribution towards global sea level rise. Here, we investigate the dynamics of the grounding zone of Petermann Glacier, a major outlet glacier in northern Greenland that develops a floating ice shelf. We use the Ice-sheet and Sea-level System Model (ISSM) and include seawater intrusions under gounded ice in the model to represent ocean-driven melt in kilometer-sized grounding zones revealed by a time series of recent radar interferometry observations. The seawater intrusions alter the thermal

regime of the ice base and melt basal ice. We initialize the model in year 2010 and run projections until year 2022. We compare the modeling results with a dense record of radar interferometry observations. If we exclude seawater intrusions and try to match the pattern of retreat, the model requires melt rates greater than 90 m/yr near the grounding line, which is not confirmed by observations. Conversely, if we use a moderate level of seawater intrusion, we match the observations quite well in terms of both the magnitude and spatial pattern of retreat across the glacier width. The best results, including a reproduction of the long-term glacier speed up, are obtained for ice melt rates of 50-60 m/yr with 3-km size intrusions. Such melt rates and scales of intrusions are fully compatible with the observations from satellite radar interferometry.

4.2 Introduction

Ocean-driven basal melt of ice shelves is a major physical mechanism controlling glacier mass loss and may be the primary factor for determining future sea level rise (An et al., 2021; Fenty et al., 2016; Mouginot et al., 2019; Pritchard et al., 2012; Roberts et al., 2018; Wood et al., 2021). In Greenland, enhanced warming of subsurface waters since the 1990s has contributed to an acceleration of glacier flow and in turn of ice mass loss (e.g. Rignot et al. 2011). Glaciers grounded well below sea level also experienced the most dramatic changes (Wood et al., 2021). The grounding line of a glacier, where it transitions from sliding across the underlying bedrock to floating on the ocean, plays a crucial role in determining its stability and evolution(e.g. Wood et al. 2018). Glaciers with deep grounding lines are in direct contact with oceanic water masses that are significantly warmer than surface waters, which results in high basal melt rates that undercut the glacier and induce grounded ice loss (Jenkins et al., 2018; Rignot et al., 2016; Thoma et al., 2008; Xu et al., 2013). The position of the grounding line directly influences the flow of ice from the interior of the ice sheet into the ocean. When the grounding line retreats, as observed in various glaciers worldwide (Brancato et al., 2020; Chen et al., 2023; Millan et al., 2022; Pelle et al., 2021; Rignot et al., 2021; Seroussi et al., 2017), more of the glacier's underside is exposed to warm ocean waters, leading to increased melting and ice loss (Mouginot et al., 2015; Park et al., 2013; Rosenau et al., 2013).

Despite the well-established understanding that grounding line dynamics are a critical component of ice mass loss and that the position of the grounding line is sensitive to ice shelf melt rates, large uncertainties remain on how to represent basal melt rates in models in order to match observations (Lilien et al., 2019). Few in situ observations of ice shelf melt rates exist (e.g. Washam et al. 2019) as measurements of melt rates near the grounding line are challenging to obtain (Rignot et al., 2010; Straneo et al., 2016). Ice shelf melt rates are commonly represented using depth-dependent parameterizations (Favier et al., 2014; Joughin et al., 2010; Shean et al., 2019; Bondzio et al., 2018; Pelle et al., 2019; Reese et al., 2018). These models are computationally efficient, but may underestimate basal melt rates near the grounding line and assume that subglacial discharge is limited to point sources. Subglacial hydrology models, however, reveal that subglacial discharge is more distributed across the grounding line (e.g. Ehrenfeucht et al. 2023), allowing for enhanced melt across a larger portion of the glacier width. More accurate representations of basal melt may be obtained using a cavity-resolving ocean model (De Rydt and Gudmundsson, 2016; Goldberg et al., 2018; Seroussi et al., 2017), e.g., the Massachusetts Institute of Technology general circulation model (MITgcm; Marshail and Clarke 1997), which allow for spatially and temporally variable melt rates within a three-dimensional geometry. At present, the required modeling resources make this approach challenging for long-term modeling applications (De Rydt and Gudmundsson, 2016). There is, therefore, a need for more realistic but computationally efficient basal melt parameterizations that make it possible to reproduce observations.

A comparison between modeled grounding line retreat and observations for several Antarctic glaciers found that using melt rates consistent with observations produced stable grounding lines (Lilien et al., 2019), which was not consistent with the many kilometers of retreat observed in the area (Rignot et al., 2014; Scheuchl et al., 2016). Better results were obtained by doubling the melt rates and concentrating them at the grounding line (Lilien et al., 2019). Similarly, a model initialization of present day Greenland achieved mixed results during model spin up using melt rates consistent with published values. Some glaciers were found to be in equilibrium consistent with observations, while others experienced extensive retreat or advances that were not consistent with observations (Lee et al., 2015). Finally, the choice of numerical implementation of melt rates at the grounding line can lead to overestimated grounding line retreat if an appropriate mesh resolution is not utilized (Seroussi and Morlighem, 2018; Vieli and Payne, 2005).

Petermann Glacier has captured attention due to two major calving events in 2010-2012 (Falkner et al., 2011; Nick et al., 2012; Hill et al., 2018; Johannessen et al., 2011; Rückamp et al., 2019) followed more recently by extensive and rapid grounding line retreat. Since about 2018, Petermann's grounding line has retreated several kilometers from its prior position, marking a substantial change in the glacier behavior (Ciracì et al., 2023; Hogg et al., 2016; Millan et al., 2022; Mouginot et al., 2019). Satellite observations have provided valuable insights into the retreat pattern of the grounding line, varying from about 7 km at the glacier center to 1-2 km elsewhere (Ciracì et al., 2023). Furthermore, these observations have revealed that the grounding line migrates by kilometers during tidal cycles, which is far larger than expected from hydrostatic equilibrium, and indicates that vigorous seawater intrusions occur during the tidal cycles, over kilometers beneath grounded ice. These observations prompt the need to represent grounding lines as grounding zones in models, and include basal melt rates within the grounding zone.

Seawater intrusions via the subglacial hydrologic system allows warm ocean waters to infiltrate the thin layer of freshwater between the grounded glacier and the underlying bedrock, delivering ocean heat to the grounded ice (Robel et al., 2022; Wilson et al., 2020). Theoretical modeling has estimated intrusion distances on the order of 10s of km upstream of the grounding line (Robel et al., 2022). The sustained freshwater layer persists year round from storage of surface meltwater runoff, frictional heating caused by glacier sliding on bedrock, and geothermal heat. The thickness of the freshwater layer depends on the bed topography, ice thickness, and other factors. Recent subglacial modeling of Petermann shows a freshwater water layer about 10 cm thick across the glacier width and extending kilometers inland (Ehrenfeucht et al., 2023).

Here, we investigate how seawater intrusion beneath grounded ice affects the grounding line retreat for Petermann. We generate model simulations with a range of values for two parameters: 1) maximum basal melt rate in the grounding zone; and 2) distance of the seawater intrusion. Seawater intrusion distance is estimated from the theoretical framework by Robel et al. (2022) and Wilson et al. (2020) combined with full subglacial hydrology modeling of Petermann Glacier. We compare the results with observations and conclude on the importance of seawater intrusions for explaining and modeling the evolution of Petermann Glacier in a warming environment.

4.3 Data and Methods

4.3.1 Model parameterization

We employ the Ice-sheet and Sea-level System Model (ISSM) to simulate grounding line migration of Petermann Glacier (Larour et al., 2012). ISSM is a state-of-the-art numerical ice sheet model that incorporates various physical processes governing ice dynamics with adaptive mesh capability. Our model domain encompasses the floating ice shelf and extends to the ice divide near the center of the ice sheet. We set the minimum mesh resolution

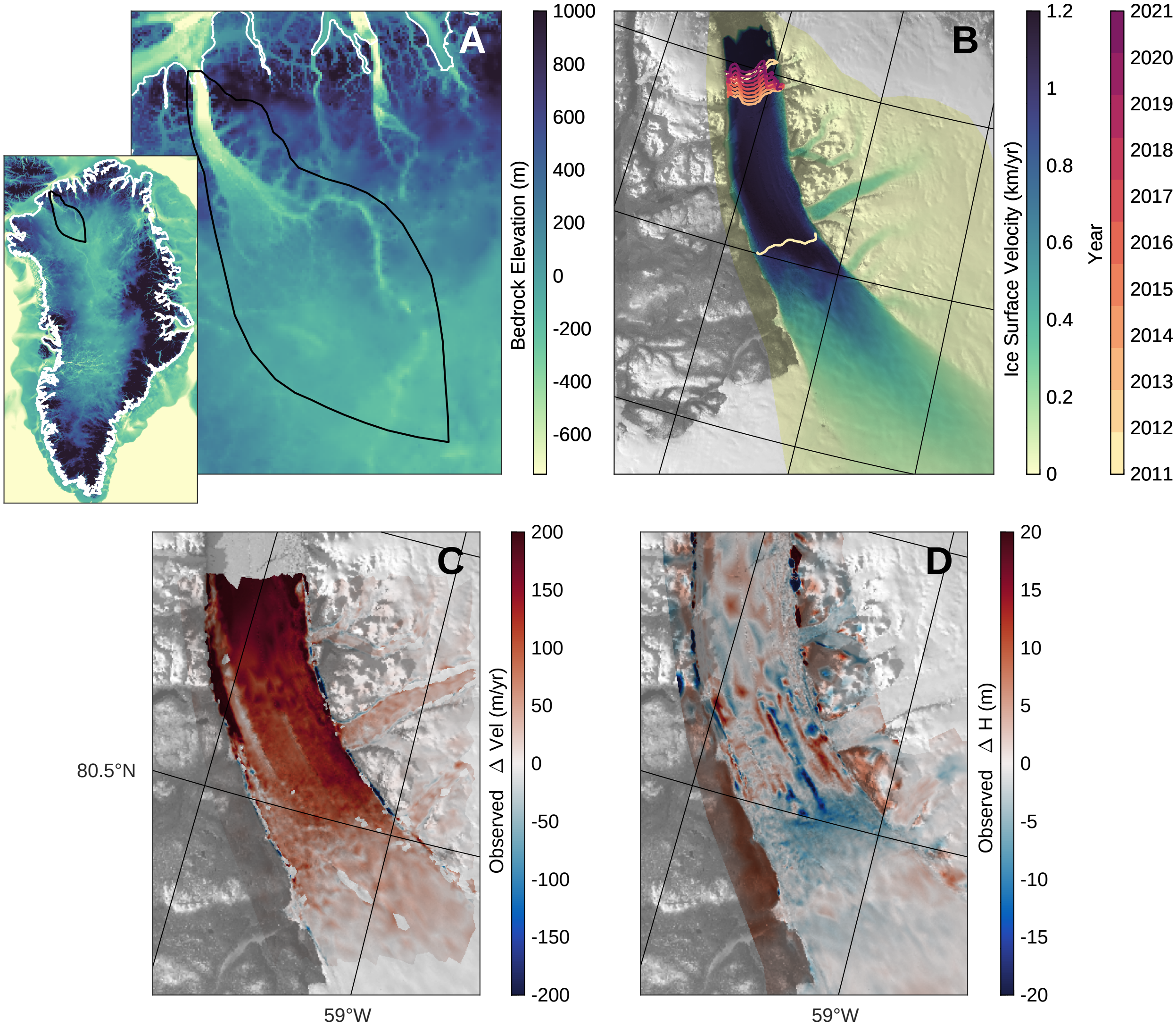

Figure 4.1: **Modeling environment of Petermann Glacier, Greenland** Inset shows location of the drainage basin. (A) model (black line) and ice extent (white line) overlain on bedrock elevation (m) from BedMachine v4 Morlighem (2021). (B) Ice surface elevation (m) from satellite data Joughin et al. (2010) with observed 1996 grounding line location Rignot (1996) and ice front locations from Ciracì et al. (2023) (C) Observed change in ice surface velocity (m/yr) from satellite observations from December 2020 Millan et al. (2022) versus a reference from 2010 Joughin et al. (2010). (D) Observed change in ice surface elevation between (m) 2010 and 2021 from TanDEM-X data Ciracì et al. (2023).

to 250 meters in the grounding zone and the maximum resolution to 15 kilometers in the slow flowing portion of the glacier in the interior of the ice shelf. Element size is inversely proportional to the gradient in ice surface velocity. The model domain contains 24,878 elements.

The model is initialized using inversion methods following (Morlighem et al., 2013) with surface velocity measurements derived from satellite observations (Joughin et al., 2010). We use the 2-D Shelfy-Stream Approximation (SSA) for ice flow (MacAyeal, 1989). Initial ice geometry is from BedMachine v4 (Morlighem et al., 2017; Morlighem, 2021), i.e., bed topography, ice thickness, ice extent, and surface elevation. We select a regularized coulomb friction law (Gagliardini et al., 2007; Joughin et al., 2019; Schoof, 2005), as recent results reveal it to be one of the most appropriate sliding law to match glacier speed up (Khan et al., 2022)

Ocean-driven melting of floating ice is represented using a depth dependent linear basal melt parameterization consistent with other studies (Åkesson et al., 2021; Choi et al., 2017). During model initialization and spin up, the maximum basal melt rate is set at 30 m/yr. This melt rate is applied to all floating ice at or below a depth of 600 m. Zero basal melt is applied to floating ice shallower than 200 m depth. For intermediate depths, the applied melt rate is linearly interpolated.

To ensure model convergence and realistic initial conditions, the fully parameterized model is spun up for 20 years without transient forcing. During this model relaxation period, we fix the ice front to its position in 2010, which is also the beginning of our dense series of observations. Ice velocity, geometry, and grounding line position are allowed to evolve to steady state values which are used as the initial conditions for the transient model simulations.

To stabilize the grounding line during model spin up in a position consistent with observations (Hogg et al., 2016; Rignot, 1996), we lower the bed elevation by 100 m on the west side of

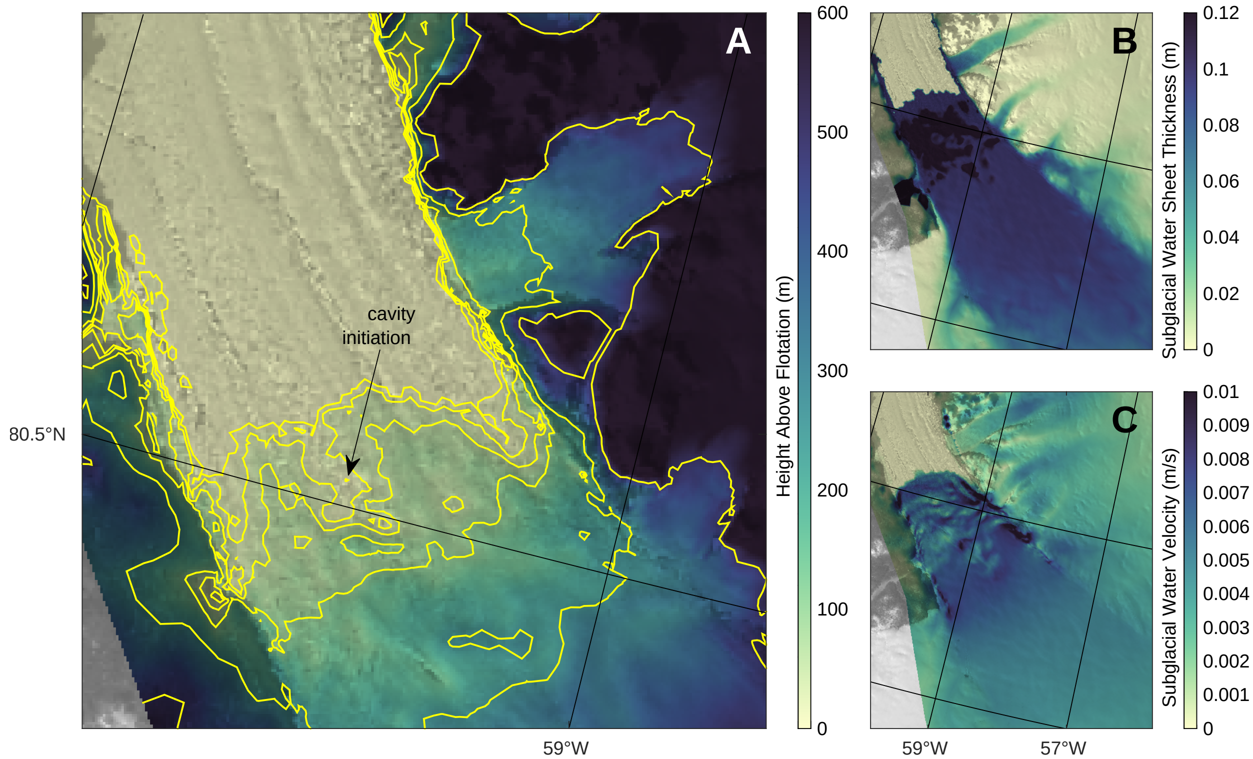

Figure 4.2: **Elevation characteristics of Petermann Glacier.** (A) height above flotation (HAF) of the fully parameterized model calculated in steady state with 1, 25, 50, 100, and 500 m contour levels. A region of ice near flotation is visible at the center where most extensive grounding line retreat has been observed (black arrow). Results from the GlaDS subglacial model Werder et al. (2013) for (B) subglacial hydrologic sheet thickness (m) and (C) water velocity (m/s) in the freshwater sheet.

the glacier. This adjustment does not alter the behavior of grounded ice but prevents the grounding line to advance in the fjord. This adjustment is justified by the lack of detailed bed elevation data in the fjord (the bed elevation in BedMachine v4 is an interpolated bed not based on actual observations).

4.3.2 Seawater intrusion via subglacial hydrology

To determine the region over which we apply ocean-driven melt from seawater infiltrating the subglacial hydrological system, we utilize a theoretical framework recently developed by (Robel et al., 2022), which was generalized from theory and experiments describing seawater intrusion within a subglacial channel (Wilson et al., 2020). This theory describes a physical mechanism in which warm salty water flows below a layer of relatively cold freshwater from basal ice melt. Here we apply the non-dimensionalized partial differential equation solving for the intrusion distance length scale using parameters obtained from the output of a subglacial hydrology model applied to Petermann. This is Equation 5 from Robel et al. (2022), which we repeat here for reference:

$$(Fr^2 - 1)\frac{\partial h}{\partial x} = Fr^2[\widetilde{C}_i(1-h)^{-1} + \widetilde{C_d}(1+\gamma h)] - \Theta, \tag{4.1}$$

where Fr is the Froude number scale which can be written in terms of Fr_0, the Froude number for the subglacial freshwater layer: $Fr = Fr_0 h^{3/2}$. $\partial h/\partial x$ is the non-dimensionalized change in thickness of the freshwater layer with respect to distance from the grounding line. $\widetilde{C}_i = C_i/C_0$ and $\widetilde{C_d} = C_d/C_0$, where C_i is the drag coefficient associated with the interface between freshwater and ocean layers in the subglacial environment, C_d is the drag coefficient associated with ice, bedrock, and obstacles within the subglacial environment, and C_0 is a characteristic scale for drag coefficients. The parameter γ is the bulk drag from water flowing through a macroporous substrate and is associated with the geometry of obstacles within the subglacial environment. It is defined as $\gamma = 2\phi H/\pi d(1-\phi)$, where ϕ is the bulk porosity of the subglacial environment, H is the combined thickness of the subglacial water sheet (ocean water and freshwater layers), and d is the characteristic obstacle diameter size. Lastly, $\Theta = tan\theta/C_0$ where θ is the bed slope.

In Equation 4.1, x is the horizontal length scale, which we consider to be oriented parallel to ice flow, not a physically realistic distance. h is the height scale of the freshwater layer, where a value of 1 corresponds to total occupation of the subglacial environment by freshwater and zero corresponds to the the grounding line where the freshwater layer thickness is zero and the subglacial environment is fully occupied by ocean water. As such, we are interested in solving for the value of x when $h = 1$, which corresponds to the length scale of maximum seawater intrusion.

We make several simplifying assumptions. We take $C_0 = C_d$ so that $\widetilde{C_d} = 1$, and $\widetilde{C_i} = C_i/C_d$. We assume that the drag from flow across ice and bedrock is much larger than the drag between the ocean and freshwater layers, i.e. $C_d >> C_i$ and therefore $\widetilde{C_i} \sim 0$. We also take $\theta = 0$. Petermann's bed is extremely flat in the grounding zone. This allows us to reduce Equation 4.1 to the following form:

$$(Fr^2 - 1)\frac{\partial h}{\partial x} = Fr^2(1 + \gamma h). \tag{4.2}$$

The freshwater layer Froude number, Fr_0, is dependent upon properties of the subglacial water sheet:

$$Fr_0 = \frac{U_{in}}{\sqrt{g'H}}, \tag{4.3}$$

where U_{in} is the velocity of the fresh subglacial discharge, and H is the thickness of the subglacial water layer. g' is a reduced gravity constant associated with the density difference between the fresh and salt water layers.

4.3.3 Subglacial hydrology

We use the Glacier Drainage System (GlaDS) model (Werder et al., 2013) to obtain steady state fields for the thickness of the subglacial water layer and the velocity of the water in that layer near Petermann's grounding zone. We run GlaDS using the model setup parameterized in ISSM, but without dynamic coupling to the ice flow modules. To obtain steady state results, we do not include seasonal meltwater runoff. Basal melt and geothermal heat flux, both from ISMIP6 data, are the only contributions to meltwater in the subglacial hydrology. We ran the subglacial hydrology model for 5 years, at which point a steady state had been reached for all hydrology output variables.

To solve Equation 4.2, representative values are required for the thickness of the hydraulic sheet layer and the velocity of the water in that layer. GlaDS model results can be seen in Figure 4.2 for both sheet thickness (Panel B) and for water velocity (Panel C). We use a value of $H = 0.1$ m as representative for the thickness of the water layer. Water velocity within the hydraulic layer is more variable than the thickness of the layer. We use a value of $U_{in} = 0.006$ m/s, which is the average within the grounding zone as calculated by GlaDS.

4.3.4 Intrusion length scale

Solving Equation 4.2, we obtain 147 as the maximum value of x, when h, the non-dimensionalized thickness of the freshwater layer is equal to 1. To determine the distance over which we will apply ocean-driven basal melt to grounded ice in our model, it is first necessary to re-dimensionalize the value of $x_{\max}$. The non-dimensional distance parameter is obtained from $x = C_0X/H$, with X equal to the actual horizontal distance and H equal to the total subglacial layer thickness, both measured in meters. To simplify Equation 4.1, we took $C_0 = C_d$, the drag coefficient associated with water flowing past ice. We therefore have the following relationship for the maximum seawater intrusion distance, L, dependent on the drag coefficient:

$$L = \frac{x_{\max} H}{C_d}. \tag{4.4}$$

Multiple estimates of C_d have been made, and generally range between 0.001 and 0.01 (Johannessen, 1970; Kottmeier and Engelbart, 1992; Lu et al., 2011; McPhee, 1989; Shirasawa, 1986), with a few cited values larger than this range (e.g. McPhee (1979)). Using the end members of this range we find a corresponding range of potential values for seawater intrusion below Petermann of between 1.47 and 14.7 km. We assume that the upper limit intrusion distance is somewhat unrealistic given the lack of any bed irregularities or localized changes in bed slope in this calculation, and focus our study on the lower end of this range, testing 5 different seawater intrusion distances from 1.5 to 6 km.

4.3.5 Transient simulations

We force our transient simulations with daily surface mass balance (SMB) data spanning the time period 2010 to 2022 from the regional climate model MAR (Fettweis et al., 2013), and prescribed annual ice front positions from TanDEM-X elevation data (Ciracì et al., 2023). We run a suite of simulations to account for uncertainties in basal melt rates and in seawater intrusion distance caused by the drag coefficient. An early estimate calculated the melt rate to be 20 m/yr from satellite observations in the proximity of the grounding line (Rignot, 1996). Since then, the ocean thermal forcing has increased in Petermann Fjord and calculations of basal melt rates have increased. One study reported melt rates exceeding 50 m/yr near the grounding line (Wilson et al., 2017). Modeling results found peak winter melt rate of 38 m/yr that increases to 85 m/yr in the summer (Cai et al., 2017). More recently, a time series of satellite observations reported basal melt rates for the grounding zone ranging from 60±13 to 80±15 m/yr between 2015 to 2021 (Ciracì et al., 2023).

Here, we use basal melt rates ranging from 10 to 90 m/yr in increments of 10 m/yr. We apply the linear depth-dependent parameterization. The only change from one simulation to to the next is the magnitude of the maximum melt rate. Ice less than 200 m deep has no melt applied. We add basal melt to grounded ice following Robel et al. (2022), with a maximum melt rate, $m_{\max}$, is applied at the grounding line, and zero additional melt is applied at a distance, L, away from the grounding line where L corresponds to the calculated seawater intrusion distance. A fractional portion of $m_{\max}$ is applied to ice within an L distance of the grounding line as $m(x) = m_{\max}/(1 - x/L)$ where x is the horizontal distance to the closest portion of the grounding line. We run simulations using 9 basal melt rates and 5 intrusion distances, totaling 45 simulations.

4.4 Results

4.4.1 Grounding line retreat

The most extensive grounding line retreat occurs where the ice is closest to flotation, following isolines in HAF (Figure 4.2 A and Figure 4.3), which is a proxy for the amount of ice thinning required to reach flotation and thus for the grounding line to retreat. After model spin up, the ice is relatively thinner along a central lobe in the middle of the glacier where HAF is smaller than on either side (Figure 4.2 A). This region of maximum retreat aligns with the observed grounding line retreat (ex: center of Figure 4.3 E3). The HAF is also relatively small along the edges of the glacier to the right and left of the central lobe (Figure 4.2 A), which are other regions of large retreat in both observations and model results.

Modeled grounding line retreat varies with the melt rate and the intrusion distance of seawater. Increased melt rates and larger seawater intrusion distances lead to more extensive grounding line retreat (Figure 4.3 Column 5 versus Column 1). There is minimal grounding line retreat in all simulations if we use a melt rate <30 m/yr (Figure 4.3 Rows 1 and 2). With a melt rate of 20 m/yr and an intrusion distance of 3 to 6 km (Figure 4.3 Panels C3-C5), we reproduce retreat where observations show the most extensive retreat, but the modeled results do not match the maximum observed retreat, even with the largest degree of seawater intrusion. This is particularly noticeable on the western edge of the glacier (Figure 4.3 C5).

Simulations with melt rates of 30 m/yr or higher and a minimum seawater intrusion distance of 1.5 km show a vastly increased amount of grounding line retreat across most of the glacier compared to simulations that exclude melt from seawater intrusion (Figure 4.3 Column 2 versus Column 1). The maximum seawater intrusion distance of 6 km results in the fastest and most extensive grounding line retreat. In simulations with a melt rate of 40 m/yr

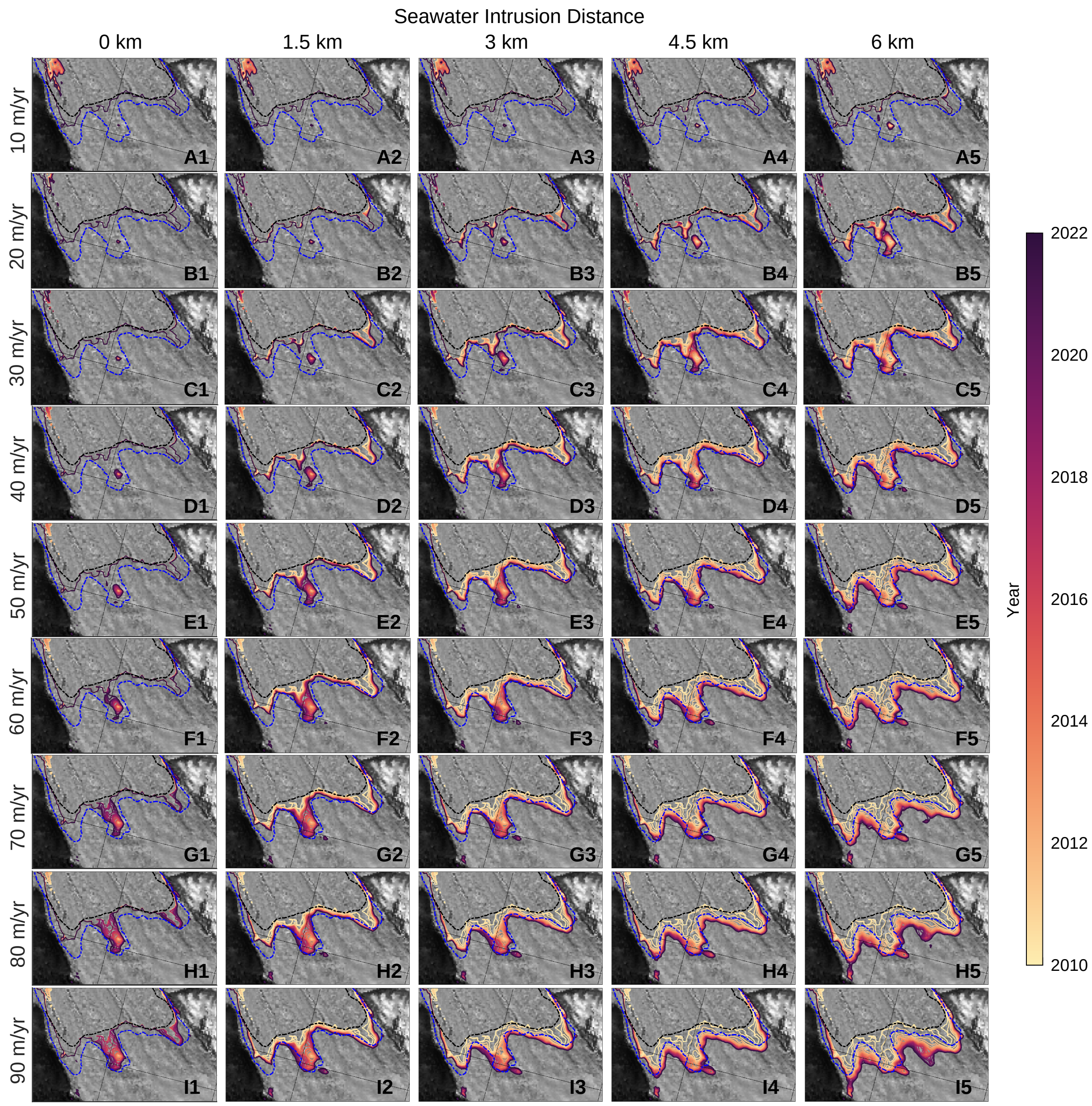

Figure 4.3: **Grounding line migration of Petermann Glacier from model simulations** with 9 basal melt rates (row) and 5 maximum intrusion distances (column) of seawater intrusion beneath grounded ice from year 2010 to 2022 color coded from white to blue, overland on Landsat satellite imagery. Reference grounding line locations are for 1996 (black) Rignot (1996) and 2022 (blue) Ciracì et al. (2023).

or higher, the modeled retreat for these simulations exceed the observed retreat along the eastern edge of the glacier (Figure 4.3 Column 5).

Most model runs underestimate grounding line retreat along the western edge of the glacier. Exceptions to this are simulations using high melt rates (>60 m/yr) and large intrusion distances (4.5 to 6 km). Results from these simulations exhibit a grounding line migration consistent with observations along the western region, but overestimated elsewhere.

4.4.2 Cavity formation

There is a small area in the center of the glacier several kilometers upstream of the grounding line that is very close to flotation in our initial steady state conditions after model spin up. This region, visible in Figure 4.2 A, is the first area to unground in all of our model simulations that exhibit any degree of grounding line retreat, which creates a small cavity of floating ice surrounded by grounded ice. We see some degree of ungrounding in the cavity in every simulation except for one. When we apply the smallest melt rate examined in the parameter space, 10 m/yr, and also have no applied seawater intrusion, the cavity remains grounded at the end of the simulation (see Figure 4.3 A1). In all other parameter combinations, we see at least an initial ungrounding of the cavity by the end of the simulation.

Once ungrounded the linear depth dependent melt rate for floating ice takes effect, regardless of the intrusion distance applied in the model simulation. For cases where the cavity begins to unground early in the simulation, we can see that it grows quickly following the initial ungrounding. The cavity expands radially at first, and then elongates parallel to the direction of ice flow. In many cases it then connects to the retreating grounding line, creating a large lobe of enhanced retreat that generally aligns with the shape of grounding line migration observed in satellite data.

The extent to which this process takes place in a particular simulation depends on both the choice of maximum melt rate and the applied seawater intrusion distance. Lower melt rates and no seawater intrusion results in the cavity remaining disconnected from the grounding line as an isolated region of floating ice. However, when a melt rate of 70 m/yr or larger is applied, the cavity is able to grow large enough to connect to the main grounding line, leading to a grounding line retreat of about 6 km in the area where the cavity is initiated. Elsewhere along the glacier minimal grounding line retreat occurs unless some degree of seawater intrusion is included in the model. Simulations with seawater intrusion included and lower melt rates also show a cavity that does not connect to the main grounding line by 2022, but the size of the cavity at the end of the simulation increases with increasing intrusion distances. Results obtained using the largest intrusion distance, 6 km, only show the isolated cavity when the lowest melt rate is used. Even the relatively small melt rate of 20 m/yr induces a retreat extensive enough for the cavity to connect to the main grounding line.

4.4.3 Ice acceleration

Changes in surface ice velocity depend on the maximum basal melt rate and distance of seawater intrusion. We obtain a slow down across most of the floating ice shelf. Some simulations show a slight speedup (10 m/yr) near the ice front. We either reproduce minimal change in velocity on grounded ice, or a speedup focused in the area of grounding line retreat that tapers off with increased upstream distance to the grounding line. The magnitude of velocity change is larger when the applied melt rate increases and when the intrusion distance increases. Model simulations that did not allow for any ocean-driven melt under grounded ice do not exhibit any speedup except if the maximum melt rate exceeds 70 m/yr. When we allow seawater to infiltrate 1.5 km upstream of the grounding line, we reproduce an increase in ice surface velocity of up to 100 m/yr immediately upstream of the grounding line (Figure

B.1).

4.4.4 Changes in ice thickness

We see substantial thinning across most of Petermann's ice shelf in all simulations that use a basal melt rate of at least 30 m/yr (see Appendix Figures B.2 and B.3). This is caused by a large amount of sub ice shelf melting as opposed to surface lowering, with the most melt occurring near the grounding line where the melt rate is higher, because the base of the ice is deeper. The total change in ice thickness over the 12 year time period exceeds 100 m in simulations using a combination of large melt rates and seawater intrusion (ex: Figure B.2 Panels D5, E4, and E5). In all simulations we see an insignificant change in ice surface elevation just downstream of the grounding line, followed by some lowering of the surface in simulations that exhibit a large degree of thinning from sub ice shelf melting (ex: Figure B.2 and B.3, Panel E5). Lowering of the ice surface for floating ice in our model simulations is the result of changes in the hydrostatic balance caused by basal melt, as opposed to SMB which we apply as a climate forcing and is equivalent across all simulations.

Our results show some thinning of grounded ice (Figure B.3), but significantly less than the degree of thinning that occurs over the floating ice shelf (Figure B.2). However, the change in ice surface elevation across the suite of simulations is dependent upon the melt rate and the intrusion distance, and can therefore not be attributed to changes in SMB. We see a decrease in surface elevation of more than 20 meters just upstream of the grounding line in simulations using a sea water intrusion distance of 6 km for most melt rates (Figure B.3 Column 5), and in simulations excluding seawater intrusion we still see lowering of the ice surface across a large region of grounded ice, but to a lesser extent with the exception of regions of the glacier that unground during the simulation. These regions experience a large magnitude of surface lowering as the hydrostatic balance changes when they start to float causing enhanced rates of thinning (see Figure B.3 Panel E1 and Figure 4.3 Panel G1). Larger basal melt rates increase the magnitude of surface lowering close to the grounding line, but the effect is also visible 10s of km inland. For example, comparing the results from our simulations using 3 km of seawater intrusion, when a meltrate of 30 m/yr is used (Figure B.3 A3) versus a melt rate of 70 m/yr (Figure B.3 E3), we see an ice surface lowering of about 5 m 20 km upstream of the grounding line by the end of the simulation with the smaller melt rate. The same region shows a surface lowering of around 12 m with the larger melt rate.

Simulations that use the lowest three melt rates (10, 20 and 30 m/yr) also exhibit substantial increases in ice thickness near the glacier's ice front, with the largest change occurring for simulations using the smallest melt rate of 10 m/yr. Change in ice thickness at the calving front reaches values as high as 20 m in simulations using a melt rate of 30 m/yr, and drop to only 2 m when using a melt rate of 70 m/yr.

4.5 Discussion

4.5.1 Comparison to observations

Our simulations agree with observations when including seawater intrusion and ice shelf melt rates between 30 and 70 m/yr. Lower melt rates require a larger degree of seawater intrusion to match the observed retreat (ex: Figure 4.3 Panel C4 versus G2). Conversely, simulations that exclude seawater intrusion yield poor fits to observations (Figure 4.3 Panel E1 versus E2). Using 6 km of the grounding line provides a poorer fit to observations (ex: Figure 4.3 Panel E5 versus E3), unless the melt rate is <30 m/yr (Figure 4.3 Panel C5).

Petermann Glacier sped up by 100-150 m/yr between 2010 and 2021 near the grounding line.

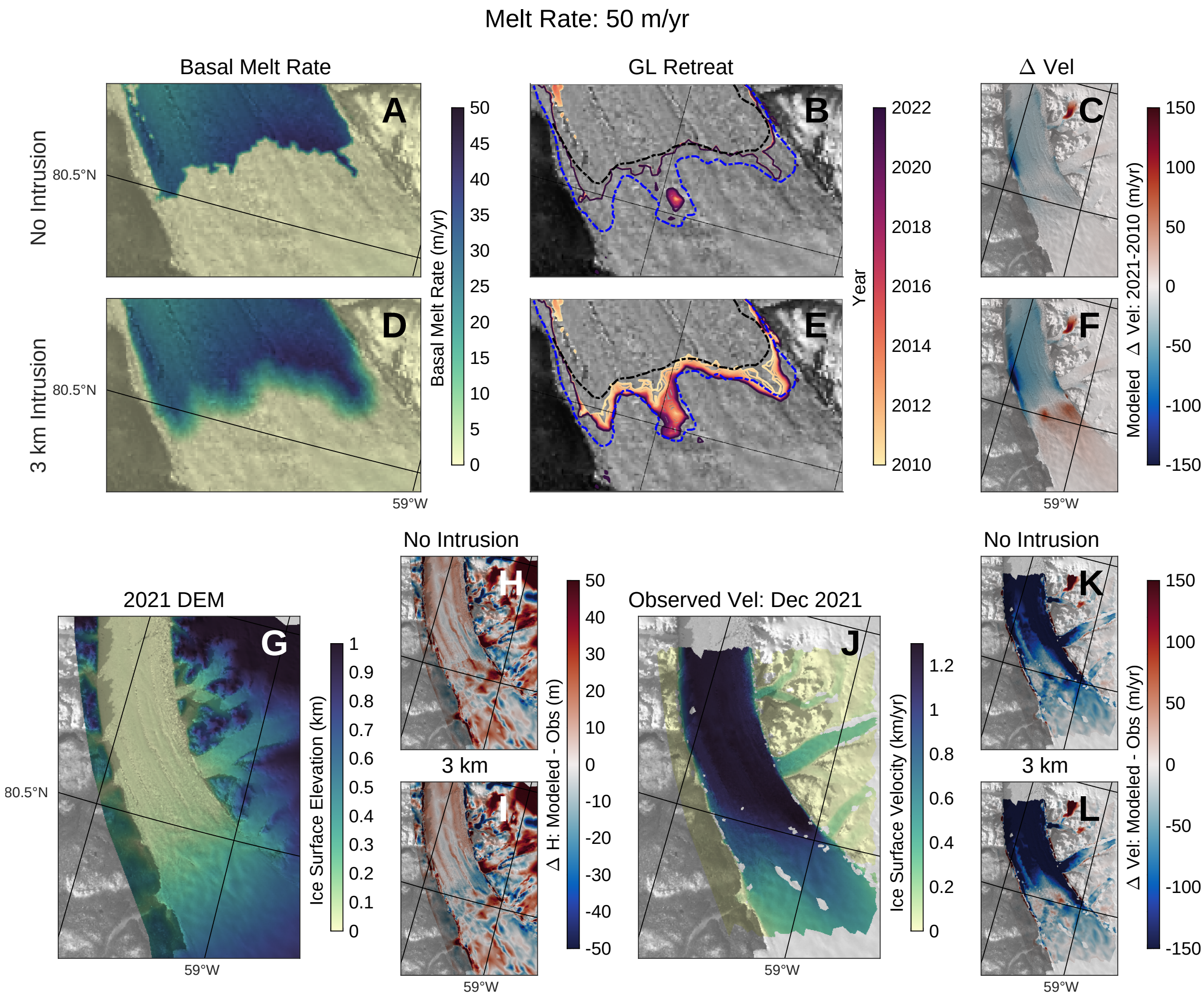

Figure 4.4: **Comparison of modeled retreat of Petermann Glacier** from two simulations with no seawater intrusion and 3-km intrusions and a 50 m/yr melt rate. (A and D) Depth-dependent basal melt rates (m/yr), (B and E) modeled grounding line migration, and (C and F) modeled change in ice surface velocity (m/yr). (G) Observed ice surface elevation (m) and (J) ice velocity (m/yr) in 2021 versus model results. Surface elevation misfit (m) for (H) no seawater intrusion and (I) 3 km of seawater intrusion. Ice surface velocity (m/yr) misfit for (K) no seawater intrusion and (L) 3 km intrusion.

The speed up tapers off to 50 m/yr speedup upstream about 30 km from the grounding line (Figure 4.1 C). Our simulations show that exclusion of seawater intrusion consistently yields a grounded ice speedup that is too small (Figure B.1 Column 1). Similarly, melt rates of 40 m/yr or less fail to reproduce speedup. However, simulations with a melt rate >50 m/yr and some degree of seawater intrusion result in a speedup on grounded ice that agrees with observations. The largest speedup occurs where grounding line retreat is the largest, i.e. the central lobe and along the eastern edge of the glacier (e.g., see Figure B.1 E5 and Figure 4.3 G5).

Observations indicate thinning within 30 km of the grounding line of 10 m between 2010 and 2020 (Figure 4.1 D). Simulations with extensive seawater intrusion produce thinning that far exceeds observations (Figure B.3 Columns 4 and 5). Even if intruding seawater were to reach such distances, its ability to melt the glacier would likely diminish due to heat exchange with ice closer to the grounding line. Our simple parameterization of thermal forcing from the seawater layer calculates melt based solely on a linear interpolation of the melt rate at the grounding line, potentially overestimating the interior thermal forcing. However, simulations without seawater intrusion generally underestimate the thinning (e.g., Figure B.3 C1), except when a melt rate of at least 70 m/yr is used (Figure B.3 E1), suggesting that some ocean-driven melt in the grounding zone is appropriate. We achieve a better fit to observations using a more moderate seawater intrusion distance of 1.5-3 km than with the larger intrusion distances.

Overall, our simulations indicate that a seawater intrusion distance of 3 km and a melt rate of 50 m/yr strike a balance between the misfit in grounding line migration, grounded ice acceleration, and ice thinning rates, yielding a final state that closely represents recent observations of Petermann (Figure 4.4).

4.5.2 Model limitations

All simulations predict a slow down of the floating ice shelf to varying degrees. This is inconsistent with observations, which show a general acceleration of the ice shelf on the same magnitude as the acceleration of grounded ice within the fast flowing region of Petermann. Despite being an inaccuracy in the model output, it is a patter than has been noted in other modeling studies. Lilien et al. (2019) see a decrease in speed on their modeled floating shelves simultaneously with acceleration of grounded ice resulting from grounding line retreat, which they attribute to ice shelf buttressing, noting that if the ice shelf were able to freely spread then any velocity change of grounded ice would be directly mirrored by floating ice. This argument is further supported by the observation that in simulations where shear margins were weakened, ice shelf speeds better matched observations. However, these simulations had worse misfit to observed velocities of grounded ice. We do not alter the shear margins in our experiments, so it seems likely that the characteristic slow down of floating ice in our model is resulting from inaccurate representations of ice shelf buttressing. Petermann, specifically, has a very damaged ice shelf with numerous large cracks visible in satellite imagery, and extensive rifting (Li et al., 2021; Millan et al., 2022; Rückamp et al., 2019). It would not be surprising if the actual buttressing capability of the ice shelf is much lower than its representation in our model reflects.

Inter-annual variability and tidal effects are not explicitly incorporated in our simulations. During summer months, enhanced rates of surface melting flush the subglacial environment with a large volume of meltwater runoff (Ehrenfeucht et al., 2023). This will necessarily alter both the thickness of the subglacial hydraulic sheet in some regions and the velocity of water flowing within the freshwater layer. Increased water velocities reduce the intrusion length scale, and with a large enough velocity, the freshwater layer essentially acts as a wall, blocking the ability for warm ocean water to slide under the freshwater layer. This could cause a seasonal shut down of the intrusion mechanism. However enhanced discharge is believed to increase sub-ice shelf basal melt as a result of the increased turbulent mixing with ocean water when the melt crosses the grounding line, which would likely mask any seasonal reduction of basal melt in the grounding zone. Additionally, tidal lifting of floating ice shelves is known to occur on daily timescales and impact grounding line dynamics (Chen et al., 2023), but these physics are generally not included in models. The impact of tidal lifting on the intrusion length scale and subglacial water layer velocities remain unexplored dynamics, but are potentially important factors to consider in this context.

4.6 Conclusions

Our model results offer significant insight into understanding grounding line migration of Petermann, and demonstrate an improvement in capturing the shape and extent of grounding line retreat by incorporating moderate seawater intrusion distances. Introducing basal melt in the grounding zone improves the modeled grounding line retreat as compared to simulations which only apply basal melt from ocean thermal forcing to floating ice in the model domain. Notably, we are able to match both observed grounding line retreat extent and the spatial spatial pattern observed while using melt rates within the range of published values by the addition of moderate seawater intrusion. Simulations excluding seawater intrusion required the use of melt rates exceeding published values to obtain the correct extent of grounding line retreat, but still failed to capture the overall observed pattern. Grounding zone processes are inherently non-static, and our simulations may not fully account for the spatial and temporal variability in this region. However, the incorporation of moderate basal melt within the grounding zone significantly improves the model's ability to reproduce observed grounding line retreat patterns, a strong indication that basal melt within the grounding zone plays a key role in these dynamics. Observed melt rates seem to be increasing and will likely grow even larger in the coming century (Ciracì et al., 2023; Wilson et al., 2017). Ocean warming will enhance the rate of basal undercutting of glaciers which is expected to induce additional grounding line retreat, reduce the buttressing effect of remaining ice shelves, and accelerate the grounded ice mass loss, making it even more critical for models to accurately represent grounding line dynamics.

Chapter 5

Conclusions

5.1 Summary of results

The work described in this dissertation aims to better understand the dynamics and behavior of Petermann Glacier, a major outlet glacier that drains a marine-based basin vulnerable to climate-driven destabilization in northern Greenland. The glacier experiences seasonal speedups in the summer melt season, and has recently been observed to have shifted away from a seemingly stable state in the 1990s, and is now undergoing retreat, accompanied by a speedup in its baseline winter velocity and thinning of its grounded ice. We focused on the physics associated with subglacial hydrology, which has been theorized to be an influential component of ice flow for quite some time. However, observations supporting its relevance are extremely limited due to the difficulty associated with reaching the subglacial environment. Thus research on this topic has largely remained theoretical until quite recently.

Computational models provide an opportunity to study the inherently complex relationships between various components of ice flow in a way that is impossible to replicate in laboratory experiments and difficult to measure with observations due to the size and nature of glacier catchments and ice sheets. However, subglacial hydrology models are relatively new as compared to other tools in the field of glaciology. The capability to couple subglacial hydrology models to ice flow models is a recent technological advancement that has only begun to be applied in the last 5 years. Even more recent is the ability to run two-way coupling between the systems (e.g. Cook et al. 2022) wherein subglacial hydrology informs ice flow, which then in turn informs subglacial hydrology, allowing the two systems to evolve together dynamically. To date, only a handful of publications have utilized coupling to ask questions related to the ability of subglacial hydrology to influence ice dynamics, and these models are not appropriate for large-scale ice flow catchments. As such, much remains unknown regarding the impact of evolving subglacial hydrology on ice flow and stability.

To address the issue of large-scale application of coupled ice dynamics and hydrology, we produced both an asynchronously and synchronously coupled framework between two state-of-the-arts models: the Glacier Drainage System (GlaDS) model (Werder et al., 2013) and the Ice-sheet and Sea-level System Model (ISSM, Larour et al. 2012). We applied this framework to study the interactions between subglacial hydrology and ice dynamics on multiple time scales. We first examined the influence of subglacial hydrology on seasonal ice velocity, followed by future projections under two different climate change scenarios to examine to what extent hydrology induced seasonal changes might impact long term stability. And finally, we examined a method by which subglacial hydrology is theorized to interact with ocean driven ice dynamics inter-annually, over a decade where we have observed significant changes in behavior. Collectively, this work contributes to a deeper understanding of Petermann Glacier's behavior, particularly its seasonal acceleration and grounding line migration. The role of subglacial hydrology and seawater intrusion emerge as significant factors influencing the glacier's dynamics and potential contributions to future sea level rise.

5.1.1 Chapter 2 main findings

In chapter 2, we applied an asynchronously coupled model framework to examine interactions between subglacial hydrology and ice dynamics, and linked the summer time speedup of Petermann observed in satellite observations (Ciracì et al., 2023; Millan et al., 2022) to the seasonal evolution of the subglacial hydrologic system. We found that by introducing time varying effective pressure, we were able to reproduce the 15% seasonal acceleration, whereas manipulating other ice flow parameters such as sub-ice shelf basal melt rates and sea ice buttressing failed to produce any significant seasonality in ice surface speeds. Modeled seasonal ice acceleration matches observations well in terms of both timing and magnitude of speedup with the addition of a physics based lower limit on effective pressure, calculated as 6% of the ice overburden pressure. We find that changes in subglacial hydrology alone are sufficient to explain the glacier's summer speedup. This work was the first published application of a coupled model framework between GlaDS and ISSM, and the publication to model the relationship between subglacial hydrology and ice velocity using realistic ice geometries on a drainage basin scale.

5.1.2 Chapter 3 main findings

In chapter 3, we examined the impact of subglacial hydrology on the future evolution of Petermann under various CMIP6 scenarios of projected climate change through 2100 using both an asynchronously and synchronously coupled model frameworks. Subglacial hydrology is generally left out of modeling simulations, including those aimed at projecting future sea level rise from glaciers and ice sheets. In chapter 2 we showed that subglacial hydrology does impact ice dynamics, at least in the case of Petermann Glacier. In chapter 3 we addressed the question of whether or not these short term seasonal changes have an accumulative impact on the long term stability of the glacier, ultimately altering projections of sea level rise. We found that including subglacial hydrology in future projections of Petermann increased the modeled sea level rise by the end of the century in all simulations. Our results showed a strong dependence of the friction law chosen during model parameterization on the magnitude of change induced by including hydrology. A Budd friction law resulted in about a 40% or more increase in the total sea level rise, and a Schoof friction law resulted in a 3-6% increase in Petermann's contribution to 21st century sea level rise. Our results demonstrate that hydrology is a key component of glacier physics that is in need of additional study if we are to correctly project sea level rise. Additionally, this work is the first successful application of the synchronously coupled framework of GlaDS and ISSM.

5.1.3 Chapter 4 main findings

In chapter 4, we focused on understanding the grounding line migration recently observed in the satellite data record (Ciracì et al., 2023; Millan et al., 2022). Notably, our model results from chapters 2 and 3 did not produce any significant grounding line migration, even in the simulations of Petermann's future evolution using climate forcing from SSP 5-8.5. This is inconsistent with observations of the extensive recent retreat, and indicates that an important process is missing from the model setup utilized in those studies. To address this inconsistency, we incorporated a recently published theory of seawater intrusion below grounded ice (Robel et al., 2022; Wilson et al., 2020) to incorporate ocean driven melting of basal ice within the grounding zone of Petermann. We utilized the generalized theoretical framework put forward by Robel et al. (2022) describing the intrusion length scale of seawater sliding below a sustained freshwater melt layer within the subglacial environment. By using steady state results from the GlaDS hydrology model, we were able to explicitly solve the equation for intrusion distance and introduce it to the modeling framework for Petermann. We ran a suite of simulations testing various basal melt rates and intrusion distances calculated using the range of published values for the drag coefficient of ice, for which significant uncertainties persist. By including seawater intrusion in model simulations, we found a significantly better match to observed grounding line behavior.

The subglacial environment is vital to accurately determining ice flow, but is difficult to accurately describe in models due to limited availability of observations and parameterizations of physical processes that are poorly constrained. Further work is necessary to understand the relevant processes occurring at the base of glaciers where the ocean, ice, freshwater and bedrock all interact. The studies presented here have each contributed to a more comprehensive understanding of the complex dynamics unfolding in the subglacial environment.

5.2 Future outlooks

Capturing the interactions between meltwater discharge from the subglacial environment, ocean circulation, and ice dynamics can be done by coupling existing ice flow, ocean, and subglacial hydrology models together, which would provide valuable insights into the relative importance of various physical processes. However, to accomplish the large scale ice sheet projections that are necessary to make future sea level rise calculations, full ice-ocean coupling is too computationally expensive to employ in all situations. Adding further coupling of subglacial hydrology would only add to the computational intensity, necessitating a basal melt parameterization that is capable of better resolving ice ocean interactions with considerations of meltwater in the subglacial environment, especially close to the grounding line. Currently, models do not allow for ocean thermal forcing to impact grounded ice. However, inclusion of ocean-driven melting in the grounding zone will likely have have a significant impact on sea level rise projections and ice sheet stability.

Much remains unknown with regards to interactions between ice, ocean, and subglacial hydrology, and there is a need for further research to refine friction laws, develop better ways to resolve or calibrate unknown parameters such as the drag coefficient of ice and the hydraulic sheet conductivity, and address the missing processes in current modeling capabilities. This aspect of glaciology is very young, making it an exciting space to occupy with many opportunities and potential applications.

5.2.1 Future work

Past and future evolutions of the Antarctic Ice Sheet with coupled subglacial hydrology and ice dynamics

In Antarctica, surface meltwater runoff is confined to low elevations along the periphery of the ice sheet and zones of blue ice on ice shelves. Despite minimal meltwater runoff, active subglacial hydrology exists in certain regions of Antarctica, primarily driven by melting of basal ice from the geothermal heat flux and from frictional heat caused by the ice flow over bedrock topography (McCormack et al., 2022), as well as the release of water from subglacial lakes (Fricker et al., 2016). Consequently, the subglacial hydrologic system in Antarctica is much less likely to undergo seasonal cycles but rather reaches longer-term steady states (Hager et al., 2022), which can be disrupted by changes in the climatology or the ice sheet's configuration, as well as shorter-term disruptions from subglacial lake outburst events (e.g. Dow et al. 2016)

In regions of fast ice flow, frictional heating can generate more melt at the glacier bed than is produced by the underlying geothermal heat flux (Joughin et al., 2009). Frictional heating alone can create a stable channelized subglacial hydrologic system (Hager et al., 2022). This process often leads to the formation of subglacial lakes as the generated basal melt pools in hydraulic lows. An extensive number of subglacial lakes have been observed using radio-echo sounding below Antarctica beginning in the 1960s (Robin et al., 1969). Some subglacial lakes are quite active, and exhibit periodic rapid drainage events which can cause short term changes in ice flow (Miles et al., 2018; Stearns et al., 2008).

Compared to Greenland, less is known about the evolution of subglacial hydrological systems, the magnitude of subglacial discharge, and their impact on ice dynamics in Antarctica (Ashmore and Bingham, 2014; Willis et al., 2016). With projected climate warming, it is anticipated that surface meltwater runoff may double over Antarctica in the coming century (Gilbert and Kittel, 2021). While most melt occurs on the ice shelves because above freezing temperatures are rarely reached on the grounded ice sheet, some regions along the periphery of the grounded ice experience surface melt, allowing for the possibility of a surface melt-subglacial hydrology connection (Ashmore and Bingham, 2014). As the century progresses we may see more active subglacial hydrologic systems develop in Antarctica with stronger influences on ice flow dynamics, similar to what is currently observed in Greenland (Dow et al., 2022).

The largest contribution to mass loss in Antarctica occurs through ice shelf melting (Rignot et al., 2019). Although melting of floating ice does not directly contribute to sea level rise, it can diminish the buttressing effect of ice shelves on glaciers, leading to increased ice discharge and ultimately rising sea levels (Sun et al., 2020). Projections indicate that over the next 300 years, the Ross, Filchner-Ronne, and Amery ice shelves will exhibit the most significant response to climate change due to weakening of ice shelf buttressing, resulting in increased ice velocity, discharge, and ultimately grounding line retreat in vulnerable areas with deep basins (Golledge et al., 2015). Grounding line retreat is directly connected with sea level rise as it is associated with ice thinning and the loss of grounded ice (Rignot et al., 2014). When the grounding line retreats beyond a stable position and onto a retrograde slope, it can trigger unstable grounding line retreat and extensive sea level rise (e.g. Favier et al. (2014)).

Furthermore, subglacial discharge is a driver of ocean-driven melting of ice shelves (Dow et al., 2022; Gwyther et al., 2023), but is currently left out of most ocean and ice sheet models.

However, increased discharge enhances thermohaline circulation and turbulent mixing below the floating ice which can increase melting (Xu et al., 2013). Seawater intrusion under grounded ice through the subglacial hydrologic system also has the potential to significantly enhance melt rates and induce rapid grounding line retreat (Robel et al., 2022; Wilson et al., 2020). Modeling studies have further shown that subglacial discharge can amplify ice shelf melt (Sergienko et al., 2013; Nakayama et al., 2021) and melting at the calving front (Cook et al., 2020). Current ocean models underestimate the rate of melt measured by satellites (Catania et al., 2010; Ciracì et al., 2023; Jackson et al., 2022). This offset might be explained or reduced by accounting for subglacial discharge.

A more complete understanding of how subglacial hydrology and ice flow dynamics interact will fill key knowledge gaps remaining in glaciology. Evaluating the capability of subglacial hydrology to impact the glacier dynamics governing ice flow and discharge will be a critical component towards producing more accurate calculations of projected sea level rise from glaciers in Antarctica.

Only a handful of studies have used coupled subglacial hydrology and ice flow models to explore the capacity of subglacial hydrology to impact future sea level rise, and as of yet, none have been applied to the full Antarctic Ice Sheet. It is unclear if subglacial hydrology will be significant in terms of impact on ice discharge, glacier stability, and ultimately sea level rise associated with Antarctica.

An opportunity for subglacial model validation

The present day Ross Sea Embayment is the largest drainage basin in Antarctica with ice contributing to it from both the East and West Antarctic Ice Sheets (Robinson et al., 2021; Rignot et al., 2008a). It currently drains roughly 25% of the total ice sheet (Halberstadt et al., 2016). Five major ice streams of the West Antarctic Ice Sheet (WAIS) feed into the eastern and central sectors of the Ross Ice Shelf: Mercer, Whillans, Lamb, Bindschadler and MacAyeal Ice Stream. The Ross Sea Embayment also drains several outlet glaciers from the larger, but less dynamic (Hughes, 1973), East Antarctic Ice Sheet (EAIS), which supply ice to the western sector of the Ross Ice Shelf. These glaciers are currently buttressed by the Ross Ice Shelf, which currently has a positive mass balance and seems to be stable (Rignot et al., 2008a). However, if the Ross Ice Shelf were to collapse, the EAIS outlet glaciers currently buttressed would likely experience grounding line retreat and substantial ice loss from the EAIS which would significantly increase the sea-level rise contribution of Antarctica. The possibility of a total collapse of the Ross Ice Shelf due to climate warming is a modeled outcome for the near term (by 2100) evolution of the Antarctic Ice Sheet with future climate change scenario RCP 8.5 (DeConto and Pollard, 2016; Golledge et al., 2015). On longer time-scales (beyond 2300), the projected total collapse of the Ross Ice Shelf occurs even in the more moderate warming scenarios RCP 4.5 and 6.0; only the best case scenario RCP 2.6 retained an intact Ross Ice Shelf by 2300 (Golledge et al., 2015).

There is extensive geologic evidence confirming that much of the present day Ross Sea was glaciated during the Last Glacial Maximum (LGM), which lasted from roughly 26.5 to 19 kya before present (BP) (Anderson et al., 2002; Clark et al., 2009; Prothro et al., 2020). The grounded ice of the Ross Sea Embayment extended nearly to the continental shelf at its maximum position (Anderson, 1999; Halberstadt et al., 2016). A data set combining marine records with radiocarbon chronology from fossil algae in sediments indicating ice extent shows that some regions of the Ross Sea remained glaciated well past other regions of Western Antarctica, with grounded ice near its maximum position until 12.3 ka BP (Christ and Bierman, 2020). Since then, grounded ice has retreated more than 1,000 km to its current location along the inner continental shelf (Anderson et al., 2014). Evidence suggests that this retreat did not occur continuously, with grounding zone wedges dating to markedly different time periods for neighboring paleo ice streams (Danielson and Bart, 2019; Ship et al., 1999). In the eastern sector of the Ross Sea, grounding line retreat did not occur until centuries after the collapse of the paleo-ice shelf (Bart et al., 2018). This suggests that additional forcings besides changing ocean conditions may be relevant to the dynamics of this region and that the long term stability of the Ross Sea Embayment may depend on complex interactions with some impacts of changing ice shelves realized much later than others. The evidence indicating non-uniform retreat of the paleo-ice sheet is consistent with the results of a modeling study that examined the ice dynamics during the collapse of the Antarctic Ice Sheet since the LGM, which showed that widespread ice sheet thinning caused by local speedup of glaciers and concluded that spatial differences acted to moderate the response of the ice sheet to ocean warming (Golledge et al., 2013).

In the present day Ross Sea, evidence has been found of a paleo-subglacial meltwater corridor indicating that when this region was last glaciated, a well developed, channelized subglacial hydrologic system had evolved under the paleo-ice sheet (Simkins et al., 2017). More evidence exists of long lasting channelized networks that developed under other paleo-ice sheets such as the Canadian Laurentide Ice Sheet, which deglaciated around 7 kyr BP (Storrar et al., 2014), the paleo-Pine Island and Thwaites Ice streams in West Antarctica (Lepp et al., 2022; Nitsche et al., 2013), and the Palmer Deep basin which contained a paleo-ice stream that was part of the Antarctic Peninsula during the LGM (Domack et al., 2006). Increased frequency of eskers, associated with channelization, during periods of deglaciation (Storrar et al., 2014) begs the question of whether a shift from a more distributed flow of subglacial meltwater to a more channelized system plays a role in ice dynamics controlling retreat and the timing of deglaciation. Analysis of bathymetry data shows that the extent of grounding line retreat was larger when a channelized drainage system was present, indicating that changes in the paleo-subglacial hydrologic system impacted ice dynamics in the Pennell Trough (Simkins et al., 2023). One study found that the feedback between ice flow and subglacial hydrology acted to switch the Kamb Ice Stream, which contributes to the modern Ross Ice Shelf from WAIS, between modes of fast flow and slow or stagnant flow by coupling modeled ice flow to a basal water routing system (van der Wel et al., 2013), further suggesting that changes to the subglacial hydrologic system are capable of inducing significant changes to ice dynamics.

Antarctic subglacial hydrology has thus far been limited by a lack of available observations with which to validate simulations. Successful implementation of a comparison study between the paleo record and output from a coupled subglacial hydrology-ice dynamics model would combine the benefits offered by the observational and modeling communities. Specifically studying the Ross Sea Embayment would take advantage of the observations available in the paleo record to validate modeling output. Observations of the subglacial environment are rare but would provide useful insights into the impacts of evolving basal conditions on ice sheet stability.

Bibliography

Abe, T. and Furuya, M. (2014). Winter speed-up of quiescent surge-type glaciers in yukon, canada. *The Cryosphere Discussions*, 8(3):2611–2635.

Ahlstrøm, A., Andersen, S. B., Andersen, M. L., Machguth, H., Nick, F., Joughin, I., Reijmer, C., van de Wal, R. S., Merryman Boncori, J. P., Box, J., et al. (2013). Seasonal velocities of eight major marine-terminating outlet glaciers of the greenland ice sheet from continuous in situ gps instruments. *Earth System Science Data*, 5(2):277–287.

Åkesson, H., Morlighem, M., O'Regan, M., and Jakobsson, M. (2021). Future Projections of Petermann Glacier Under Ocean Warming Depend Strongly on Friction Law. *J. Geophys. Res. - Earth Surface*, 126(6):e2020JF005921.

Alley, K. E., Scambos, T. A., Siegfried, M. R., and Fricker, H. A. (2016). Impacts of warm water on Antarctic ice shelf stability through basal channel formation. *Nat. Geosci.*, 9:290–293.

Amundson, J. M., Fahnestock, M., Truffer, M., Brown, J., Lüthi, M. P., and Motyka, R. J. (2010). Ice mélange dynamics and implications for terminus stability, Jakobshavn Isbræ, Greenland. *J. Geophys. Res. Earth Surf.*, 115(F1).

An, L., Rignot, E., Wood, M., Willis, J. K., Mouginot, J., and Khan, S. A. (2021). Ocean melting of the zachariae isstrøm and nioghalvfjerdsfjorden glaciers, northeast greenland. *Proceedings of the National Academy of Sciences*, 118(2):e2015483118.

Anderson, J. B. (1999). *Antarctic marine geology.* Cambridge University Press.

Anderson, J. B., Conway, H., Bart, P. J., Witus, A. E., Greenwood, S. L., McKay, R. M., Hall, B. L., Ackert, R. P., Licht, K., Jakobsson, M., et al. (2014). Ross sea paleo-ice sheet drainage and deglacial history during and since the lgm. *Quaternary Science Reviews*, 100:31–54.

Anderson, J. B., Shipp, S. S., Lowe, A. L., Wellner, J. S., and Mosola, A. B. (2002). The antarctic ice sheet during the last glacial maximum and its subsequent retreat history: a review. *Quaternary Science Reviews*, 21(1-3):49–70.

Andrews, L. C., Catania, G. A., Hoffman, M. J., Gulley, J. D., Luethi, M. P., Ryser, C., Hawley, R. L., and Neumann, T. A. (2014). Direct observations of evolving subglacial drainage beneath the greenland ice sheet. *Nature*, 514(7520):80–83.

Armstrong, W. H., Polashenski, D., Truffer, M., Horne, G., Hanson, J. B., Hawley, R. L., Hengst, A. M., Vowels, L., Menounos, B., and Wychen, W. V. (2022). Declining basal motion dominates the long-term slowing of athabasca glacier, canada. *Journal of Geophysical Research: Earth Surface*, 127(10):e2021JF006439.

Aschwanden, A. and Brinkerhoff, D. (2022). Calibrated mass loss predictions for the greenland ice sheet. *Geophysical Research Letters*, 49(19):e2022GL099058.

Ashmore, D. W. and Bingham, R. G. (2014). Antarctic subglacial hydrology: current knowledge and future challenges. *Antarctic Science*, 26(6):758–773.

Bamber, J. L., Griggs, J. A., Hurkmans, R. T. W. L., Dowdeswell, J. A., Gogineni, S. P., Howat, I., Mouginot, J., Paden, J., Palmer, S., Rignot, E., and Steinhage, D. (2013). A new bed elevation dataset for Greenland. *The Cryosphere*, 7:499–510.

Bart, P. J., DeCesare, M., Rosenheim, B. E., Majewski, W., and McGlannan, A. (2018). A centuries-long delay between a paleo-ice-shelf collapse and grounding-line retreat in the whales deep basin, eastern ross sea, antarctica. *Scientific reports*, 8(1):12392.

Bartholomaus, T. C., Anderson, R. S., and Anderson, S. P. (2011). Growth and collapse of the distributed subglacial hydrologic system of Kennicott Glacier, Alaska, USA, and its effects on basal motion. *Journal of Glaciology*, 57(206):985–1002.

Bartholomew, I., Nienow, P., Sole, A., Mair, D., Cowton, T., and King, M. A. (2012). Short-term variability in Greenland Ice Sheet motion forced by time-varying meltwater drainage: Implications for the relationship between subglacial drainage system behavior and ice velocity. *J. Geophys. Res. - Earth Surface*, 117:1–17.

Bartholomew, I. D., Nienow, P., Sole, A., Mair, D., Cowton, T., King, M. A., and Palmer, S. (2011). Seasonal variations in Greenland Ice Sheet motion: Inland extent and behaviour at higher elevations. *Earth Planet. Sci. Lett.*, 307(3-4):271–278.

Bevan, S. L., Luckman, A., Khan, S. A., and Murray, T. (2015). Seasonal dynamic thinning at helheim glacier. *Earth and Planetary Science Letters*, 415:47–53.

Bindschadler, R. (1983). The importance of pressurized subglacial water in separation and sliding at the glacier bed. *Journal of Glaciology*, 29(101):3–19.

Bondzio, J. H., Morlighem, M., Seroussi, H., Wood, M. H., and Mouginot, J. (2018). Control of ocean temperature on jakobshavn isbræ's present and future mass loss. *Geophysical Research Letters*, 45(23):12–912.

Brancato, V., Rignot, E., Milillo, P., Morlighem, M., Mouginot, J., An, L., Scheuchl, B., Jeong, S., Rizzoli, P., Bueso Bello, J. L., et al. (2020). Grounding line retreat of denman glacier, east antarctica, measured with cosmo-skymed radar interferometry data. *Geophysical Research Letters*, 47(7):e2019GL086291.

Brondex, J., Gagliardini, O., Gillet-Chaulet, F., and Durand, G. (2017). Sensitivity of grounding line dynamics to the choice of the friction law. *Journal of Glaciology*, 63(241):854–866.

Brondex, J., Gillet-Chaulet, F., and Gagliardini, O. (2019). Sensitivity of centennial mass loss projections of the Amundsen basin to the friction law. *The Cryosphere*, 13:177–195.

Budd, W. F., Keage, P. L., and Blundy, N. A. (1979). Empirical studies of ice sliding. *Journal of Glaciology*, 23:157–170.

Bueler, E. and van Pelt, W. (2015). Mass-conserving subglacial hydrology in the Parallel Ice Sheet Model version 0.6. *Geosci. Model Dev.*, 8(6):1613–1635.

Cai, C., Rignot, E., Menemenlis, D., and Nakayama, Y. (2017). Observations and modeling of ocean-induced melt beneath petermann glacier ice shelf in northwestern greenland. *Geophys. Res. Lett.*, 44(16):8396–8403.

Cassotto, R., Fahnestock, M., Amundson, J. M., Truffer, M., and Joughin, I. (2015). Seasonal and interannual variations in ice melange and its impact on terminus stability, Jakobshavn Isbræ, Greenland. *Journal of Glaciology*, 61(225):76–88.

Catania, G., Hulbe, C., and Conway, H. (2010). Grounding-line basal melt rates determined using radar-derived internal stratigraphy. *Journal of Glaciology*, 56(197):545–554.

Chen, H., Rignot, E., Scheuchl, B., and Ehrenfeucht, S. (2023). Grounding zone of amery ice shelf, antarctica, from differential synthetic-aperture radar interferometry. *Geophysical Research Letters*, 50(6):e2022GL102430.

Cheng, L., von Schuckmann, K., Abraham, J. P., Trenberth, K. E., Mann, M. E., Zanna, L., England, M. H., Zika, J. D., Fasullo, J. T., Yu, Y., et al. (2022). Past and future ocean warming. *Nature Reviews Earth & Environment*, 3(11):776–794.

Choi, Y., Morlighem, M., Rignot, E., Mouginot, J., and Wood, M. (2017). Modeling the response of Nioghalvfjerdsfjorden and Zachariae Isstrøm glaciers, Greenland, to ocean forcing over the next century. *Geophys. Res. Lett.*, 44(21):11,071–11,079.

Choi, Y., Morlighem, M., Rignot, E., and Wood, M. (2021). Ice dynamics will remain a primary driver of Greenland ice sheet mass loss over the next century. *Nature Commun. Earth Environ.*, 2(1):26.

Choi, Y., Morlighem, M., Wood, M., and Bondzio, J. H. (2018). Comparison of four calving laws to model Greenland outlet glaciers. *The Cryosphere*, 12(12):3735–3746.

Choi, Y., Seroussi, H., Gardner, A., and Schlegel, N.-J. (2022). Uncovering basal friction in northwest greenland using an ice flow model and observations of the past decade. *Journal of Geophysical Research: Earth Surface*, 127(10):e2022JF006710.

Christ, A. J. and Bierman, P. R. (2020). The local last glacial maximum in mcmurdo sound, antarctica: Implications for ice-sheet behavior in the ross sea embayment. *GSA Bulletin*, 132(1-2):31–47.

Chu, V. W. (2014). Greenland ice sheet hydrology: A review. *Progress in Physical Geography*, 38(1):19–54.

Chu, W., Schroeder, D. M., Seroussi, H., Creyts, T. T., Palmer, S. J., and Bell, R. E. (2016). Extensive winter subglacial water storage beneath the Greenland Ice Sheet. *Geophysical Research Letters*, 43.

Ciracì, E., Rignot, E., Scheuchl, B., Tolpekin, V., Wollersheim, M., An, L., Milillo, P., Bueso-Bello, J.-L., Rizzoli, P., and Dini, L. (2023). Melt rates in the kilometer-size grounding zone of petermann glacier, greenland, before and during a retreat. *Proceedings of the National Academy of Sciences*, 120(20):e2220924120.

Clark, C. D., Hughes, A. L., Greenwood, S. L., Spagnolo, M., and Ng, F. S. (2009). Size and shape characteristics of drumlins, derived from a large sample, and associated scaling laws. *Quaternary Science Reviews*, 28(7-8):677–692.

Clason, C. C., Mair, D. W. F., Nienow, P. W., Bartholomew, I. D., Sole, A., Palmer, S., and Schwanghart, W. (2015). Modelling the transfer of supraglacial meltwater to the bed of Leverett Glacier, Southwest Greenland. *The Cryosphere*, 9:123–138.

Cook, S. J., Christoffersen, P., and Todd, J. (2022). A fully-coupled 3d model of a large greenlandic outlet glacier with evolving subglacial hydrology, frontal plume melting and calving. *Journal of Glaciology*, 68(269):486–502.

Cook, S. J., Christoffersen, P., Todd, J., Slater, D., and Chauché, N. (2020). Coupled modelling of subglacial hydrology and calving-front melting at store glacier, west greenland. *The Cryosphere*, 14(3):905–924.

Cornford, S. L., Seroussi, H., Asay-Davis, X. S., Gudmundsson, G. H., Arthern, R., Borstad, C., Christmann, J., Dias dos Santos, T., Feldmann, J., Goldberg, D., et al. (2020). Results of the third marine ice sheet model intercomparison project (mismip+). *The Cryosphere*, 14(7):2283–2301.

Crawford, A. J., Mueller, D., Desjardins, L., and Myers, P. G. (2018). The aftermath of Petermann Glacier Calving Events (2008–2012): Ice Island Size Distributions and Meltwater Dispersal. *J. Geophys. Res.*, 123(12):8812–8827.

Csatho, B., Schenk, T., Van Der Veen, C. J., and Krabill, W. B. (2008). Intermittent thinning of Jakobshavn Isbrae, West Greenland, since the Little Ice Age. *Journal of Glaciology*, 54(184):131–144.

Cuffey, K. M. and Paterson, W. S. B. (2010). *The Physics of Glaciers, 4th Edition*. Elsevier, Oxford.

Danabasoglu, G., Lamarque, J.-F., Bacmeister, J., Bailey, D., DuVivier, A., Edwards, J., Emmons, L., Fasullo, J., Garcia, R., Gettelman, A., et al. (2020). The community earth system model version 2 (cesm2). *Journal of Advances in Modeling Earth Systems*, 12(2):e2019MS001916.

Danielson, M. and Bart, P. (2019). Topographic control on the post-lgm grounding zone locations of the west antarctic ice sheet in the whales deep basin, eastern ross sea. *Marine Geology*, 407:248–260.

Davison, B. J., Sole, A. J., Livingstone, S. J., Cowton, T. R., and Nienow, P. W. (2019). The influence of hydrology on the dynamics of land-terminating sectors of the greenland ice sheet. *Front. Earth Sci.*, 7:10.

De Fleurian, B., Gagliardini, O., Zwinger, T., Durand, G., Le Meur, E., Mair, D., and Råback, P. (2014). A double continuum hydrological model for glacier applications. *The Cryosphere*, 8(1):137–153.

De Rydt, J. and Gudmundsson, G. H. (2016). Coupled ice shelf-ocean modeling and complex grounding line retreat from a seabed ridge. *Journal of Geophysical Research: Earth Surface*, 121(5):865–880.

DeConto, R. M. and Pollard, D. (2016). Contribution of antarctica to past and future sea-level rise. *Nature*, 531(7596):591–597.

Domack, E., Amblas, D., Gilbert, R., Brachfeld, S., Camerlenghi, A., Rebesco, M., Canals, M., and Urgeles, R. (2006). Subglacial morphology and glacial evolution of the palmer deep outlet system, antarctic peninsula. *Geomorphology*, 75(1-2):125–142.

Dow, C., McCormack, F., Young, D., Greenbaum, J., Roberts, J., and Blankenship, D. (2020). Totten glacier subglacial hydrology determined from geophysics and modeling. *Earth and Planetary Science Letters*, 531:115961.

Dow, C., Ross, N., Jeofry, H., Siu, K., and Siegert, M. (2022). Antarctic basal environment shaped by high-pressure flow through a subglacial river system. *Nature Geoscience*, 15(11):892–898.

Dow, C. F., Kulessa, B., Rutt, I. C., Tsai, V. C., Pimentel, S., Doyle, S. H., van As, D., Lindbäck, K., Pettersson, R., Jones, G. A., and Hubbard, A. (2015). Modeling of subglacial hydrological development following rapid supraglacial lake drainage. *J. Geophys. Res.*, 120(6):1127–1147.

Dow, C. F., Werder, M. A., Nowicki, S., and Walker, R. T. (2016). Modeling Antarctic subglacial lake filling and drainage cycles. *The Cryosphere*, 10:1381–1393.

Downs, J. Z., Johnson, J. V., Harper, J. T., Meierbachtol, T., and Werder, M. A. (2018). Dynamic hydraulic conductivity reconciles mismatch between modeled and observed winter subglacial water pressure. *Journal of Geophysical Research: Earth Surface*, 123(4):818–836.

Echelmeyer, K. and Harrison, W. D. (1990). Jakobshavns Isbræ, West Greenland - Seasonal variations in velocity or lack thereof. *Journal of Glaciology*, 36(122):82–88.

Ehrenfeucht, S., Morlighem, M., Rignot, E., Dow, C. F., and Mouginot, J. (2023). Seasonal acceleration of petermann glacier, greenland, from changes in subglacial hydrology. *Geophysical Research Letters*, 50(1):e2022GL098009.

Engelhardt, H., Harrison, W., and Kamb, B. (1978). Basal sliding and conditions at the glacier bed as revealed by bore-hole photography. *Journal of Glaciology*, 20(84):469–508.

Eyring, V., Bony, S., Meehl, G. A., Senior, C. A., Stevens, B., Stouffer, R. J., and Taylor, K. E. (2016). Overview of the Coupled Model Intercomparison Project Phase 6 (CMIP6) experimental design and organization. *Geosci. Model Dev.*, 9(5):1937–1958.

Falkner, K. K., Melling, H., Münchow, A. M., Box, J. E., Wohlleben, T., Johnson, H. L., Gudmandsen, P., Samelson, R., Copland, L., Steffen, K., Rignot, E., and Higgins, A. K. (2011). Context for the recent massive petermann glacier calving event. *Eos*, 92(14):117–118.

Favier, L., Durand, G., Cornford, S. L., Gudmundsson, G. H., Gagliardini, O., Gillet-Chaulet, F., Zwinger, T., Payne, A., and Le Brocq, A. M. (2014). Retreat of pine island glacier controlled by marine ice-sheet instability. *Nature Climate Change*, 4(2):117–121.

Fenty, I., Willis, J. K., Khazendar, A., Dinardo, S., Forsberg, R., Fukumori, I., Holland, D., Jakobsson, M., Moller, D., Morison, J., et al. (2016). Oceans melting greenland: Early results from nasa's ocean-ice mission in greenland. *Oceanography*, 29(4):72–83.

Fettweis, X., Box, J. E., Agosta, C., Amory, C., Kittel, C., Lang, C., van As, D., Machguth, H., and Gallee, H. (2017). Reconstructions of the 1900-2015 greenland ice sheet surface mass balance using the regional climate mar model. *The Cryosphere*, 11(2):1015–1033.

Fettweis, X., Franco, B., Tedesco, M., van Angelen, J. H., Lenaerts, J. T. M., van den Broeke, M. R., and Gallée, H. (2013). Estimating the Greenland ice sheet surface mass balance contribution to future sea level rise using the regional atmospheric climate model MAR. *The Cryosphere*, 7(2):469–489.

Fountain, A. G. and Walder, J. S. (1998). Water flow through temperate glaciers. *Reviews of Geophysics*, 36(3):299–328.

Fowler, A. (2010). Weertman, lliboutry and the development of sliding theory. *Journal of Glaciology*, 56(200):965–972.

Fricker, H. A., Siegfried, M. R., Carter, S. P., and Scambos, T. A. (2016). A decade of progress in observing and modelling antarctic subglacial water systems. *Philosophical Transactions of the Royal Society A: Mathematical, Physical and Engineering Sciences*, 374(2059):20140294.

Gagliardini, O., Cohen, D., Raback, P., and Zwinger, T. (2007). Finite-element modeling of subglacial cavities and related friction law. *J. Geophys. Res. - Earth Surface*, 112(F2):1–11.

Gilbert, E. and Kittel, C. (2021). Surface melt and runoff on antarctic ice shelves at 1.5 c, 2 c, and 4 c of future warming. *Geophysical Research Letters*, 48(8):e2020GL091733.

Gladish, C. V., Holland, D. M., Holland, P. R., and Price, S. F. (2012). Ice-shelf basal channels in a coupled ice/ocean model. *Journal of Glaciology*, 58(212):1227–1244.

Glen, J. W. (1958). The flow law of ice: A discussion of the assumptions made in glacier theory, their experimental foundations and consequences. *IASH Publ*, 47:171–183.

Goelzer, H., Nowicki, S., Edwards, T., Beckley, M., Abe-Ouchi, A., Aschwanden, A., Calov, R., Gagliardini, O., Gillet-Chaulet, F., Golledge, N. R., Gregory, J., Greve, R., Humbert, A., Huybrechts, P., Kennedy, J. H., Larour, E., Lipscomb, W. H., Leclec'h, S., Lee, V., Morlighem, M., Pattyn, F., Payne, A. J., Rodehacke, C., Rückamp, M., Saito, F., Schlegel, N., Seroussi, H., Shepherd, A., Sun, S., van de Wal, R., and Ziemen, F. A. (2018). Design and results of the ice sheet model initialisation experiments initMIP-Greenland: an ISMIP6 intercomparison. *The Cryosphere*, 12(4):1433–1460.

Goelzer, H., Nowicki, S., Payne, A., Larour, E., Seroussi, H., Lipscomb, W. H., Gregory, J., Abe-Ouchi, A., Shepherd, A., Simon, E., et al. (2020). The future sea-level contribution of the greenland ice sheet: a multi-model ensemble study of ismip6. *The Cryosphere*, 14(9):3071–3096.

Goldberg, D., Holland, D., and Schoof, C. (2009). Grounding line movement and ice shelf buttressing in marine ice sheets. *Journal of Geophysical Research: Earth Surface*, 114(F4).

Goldberg, D., Snow, K., Holland, P., Jordan, J., Campin, J.-M., Heimbach, P., Arthern, R., and Jenkins, A. (2018). Representing grounding line migration in synchronous coupling between a marine ice sheet model and a z-coordinate ocean model. *Ocean Modelling*, 125:45–60.

Goldberg, D. N., Gourmelen, N., Kimura, S., Millan, R., and Snow, K. (2019). How Accurately Should We Model Ice Shelf Melt Rates? *Geophys. Res. Lett.*, 46.

Golledge, N. R., Kowalewski, D. E., Naish, T. R., Levy, R. H., Fogwill, C. J., and Gasson, E. G. (2015). The multi-millennial antarctic commitment to future sea-level rise. *Nature*, 526(7573):421–425.

Golledge, N. R., Levy, R. H., McKay, R. M., Fogwill, C. J., White, D. A., Graham, A. G., Smith, J. A., Hillenbrand, C.-D., Licht, K. J., Denton, G. H., et al. (2013). Glaciology and geological signature of the last glacial maximum antarctic ice sheet. *Quaternary Science Reviews*, 78:225–247.

Gudmundsson, G. H. (2013). Ice-shelf buttressing and the stability of marine ice sheets. *The Cryosphere*, 7(2):647–655.

Gwyther, D. E., Dow, C. F., Jendersie, S., Gourmelen, N., and Galton-Fenzi, B. K. (2023). Subglacial freshwater drainage increases simulated basal melt of the totten ice shelf. *Geophysical Research Letters*, 50(12):e2023GL103765.

Hager, A. O., Hoffman, M. J., Price, S. F., and Schroeder, D. M. (2022). Persistent, extensive channelized drainage modeled beneath thwaites glacier, west antarctica. *The Cryosphere*, 16(9):3575–3599.

Halberstadt, A. R. W., Simkins, L. M., Greenwood, S. L., and Anderson, J. B. (2016). Past ice-sheet behaviour: retreat scenarios and changing controls in the ross sea, antarctica. *The Cryosphere*, 10(3):1003–1020.

Hewitt, I. J. (2013). Seasonal changes in ice sheet motion due to melt water lubrication. *Earth Planet. Sci. Lett.*, 371-372(0):16 – 25.

Hewitt, I. J. (2020). Subglacial plumes. *Annual Review of Fluid Mechanics*, 52:145–169.

Hewitt, I. J., Schoof, C., and Werder, M. A. (2012). Flotation and free surface flow in a model for subglacial drainage. Part 2. Channel flow. *J. Fluid Mech.*, 702:157–187.

Hill, E. A., Carr, J. R., Stokes, C. R., and Gudmundsson, G. H. (2018). Dynamic changes in outlet glaciers in northern Greenland from 1948 to 2015. *The Cryosphere*, 12(10):3243–3263.

Hofer, S., Lang, C., Amory, C., Kittel, C., Delhasse, A., Tedstone, A., and Fettweis, X. (2020). Greater greenland ice sheet contribution to global sea level rise in cmip6. *Nature communications*, 11(1):6289.

Hoffman, M. and Price, S. (2014). Feedbacks between coupled subglacial hydrology and glacier dynamics. *J. Geophys. Res.*, 119(3):414–436.

Hogg, A. E., Shepherd, A., Gourmelen, N., and Engdahl, M. (2016). Grounding line migration from 1992 to 2011 on petermann glacier, north-west greenland. *Journal of Glaciology*, 62(236):1104–1114.

Holland, D. M., Thomas, R. H., De Young, B., Ribergaard, M. H., and Lyberth, B. (2008). Acceleration of Jakobshavn Isbrae triggered by warm subsurface ocean waters. *Nat. Geosci.*, 1(10):659–664.

Howat, I. M., Joughin, I., Fahnestock, M., Smith, B. E., and Scambos, T. A. (2008). Synchronous retreat and acceleration of southeast greenland outlet glaciers 2000–06: ice dynamics and coupling to climate. *Journal of Glaciology*, 54(187):646–660.

Howat, I. M., Joughin, I., and Scambos, T. A. (2007). Rapid changes in ice discharge from Greenland outlet glaciers. *Science*, 315(5818):1559–1561.

Howat, I. M., Joughin, I., Tulaczyk, S., and Gogineni, S. (2005). Rapid retreat and acceleration of Helheim Glacier, east Greenland. *Geophysical Research Letters*, 32(22):1–4.

Hubbard, A., Willis, I., Sharp, M., Mair, D., Nienow, P., Hubbard, B., and Blatter, H. (2000). Glacier mass-balance determination by remote sensing and high-resolution modelling. *Journal of Glaciology*, 46(154):491–498.

Iken, A. (1981). The effect of the subglacial water pressure on the sliding velocity of a glacier in an idealized numerical Model. *Journal of Glaciology*, 27(97):407–421.

Iverson, N. R. and Zoet, L. K. (2015). Experiments on the dynamics and sedimentary products of glacier slip. *Geomorphology*, 244:121–134.

Jackson, R. H., Motyka, R. J., Amundson, J. M., Abib, N., Sutherland, D. A., Nash, J. D., and Kienholz, C. (2022). The relationship between submarine melt and subglacial discharge from observations at a tidewater glacier. *Journal of Geophysical Research: Oceans*, 127(10):e2021JC018204.

Jenkins, A. (2011). Convection-driven melting near the grounding lines of ice shelves and tidewater glaciers. *J. Phys. Oceanogr.*

Jenkins, A., Shoosmith, D., Dutrieux, P., Jacobs, S., Kim, T. W., Lee, S. H., Ha, H. K., and Stammerjohn, S. (2018). West Antarctic Ice Sheet retreat in the Amundsen Sea driven by decadal oceanic variability. *Nat. Geosci.*

Johannessen, O., Babiker, M., and Miles, M. (2011). Petermann glacier, north greenland: massive calving in 2010 and the past half century. *The Cryosphere Discussions*, 5(1):169–181.

Johannessen, O. M. (1970). Note on some vertical profiles below ice floes in the gulf of st. lawrence and near the north pole. *Journal of Geophysical Research*, 75(15):2857–2861.

Joughin, I., Das, S. B., King, M. A., Smith, B. E., Howat, I. M., and Moon, T. (2008). Seasonal speedup along the western flank of the Greenland Ice Sheet. *Science*, 320(5877):781–783.

Joughin, I., Smith, B. E., Howat, I. M., Scambos, T., and Moon, T. (2010). Greenland flow variability from ice-sheet-wide velocity mapping. *Journal of Glaciology*, 56:416–430.

Joughin, I., Smith, B. E., and Schoof, C. G. (2019). Regularized coulomb friction laws for ice sheet sliding: Application to pine island glacier, antarctica. *Geophysical Research Letters*, 46.

Joughin, I., Tulaczyk, S., Bamber, J. L., Blankenship, D., Holt, J. W., Scambos, T., and Vaughan, D. G. (2009). Basal conditions for pine island and thwaites glaciers, west antarctica, determined using satellite and airborne data. *Journal of Glaciology*, 55(190):245–257.

Kamb, B. (1970). Sliding motion of glaciers: theory and observation. *Reviews of Geophysics*, 8(4):673–728.

Kamb, B. (1987). Glacier surge mechanism based on linked cavity configuration of the basal water conduit system. *J. Geophys. Res.*, 92(B9):9083–9100.

Kay, J. E., Deser, C., Phillips, A., Mai, A., Hannay, C., Strand, G., Arblaster, J. M., Bates, S., Danabasoglu, G., Edwards, J., et al. (2015). The community earth system model (cesm) large ensemble project: A community resource for studying climate change in the presence of internal climate variability. *Bulletin of the American Meteorological Society*, 96(8):1333–1349.

Kehrl, L. M., Joughin, I., Shean, D. E., Floricioiu, D., and Krieger, L. (2017). Seasonal and interannual variabilities in terminus position, glacier velocity, and surface elevation at helheim and kangerlussuaq glaciers from 2008 to 2016. *Journal of Geophysical Research: Earth Surface*, 122(9):1635–1652.

Khan, S. A., Choi, Y., Morlighem, M., Rignot, E., Helm, V., Humbert, A., Mouginot, J., Millan, R., Kjær, K. H., and Bjørk, A. A. (2022). Extensive inland thinning and speed-up of northeast greenland ice stream. *Nature*, 611(7937):727–732.

Khan, S. A., Kjaer, K. H., Bevis, M., Bamber, J. L., Wahr, J., Kjeldsen, K. K., Bjork, A. A., Korsgaard, N. J., Stearns, L. A., van den Broeke, M. R., Liu, L., Larsen, N. K., and Muresan, I. S. (2014). Sustained mass loss of the northeast Greenland ice sheet triggered by regional warming. *Nat. Clim. Change*, 4(4):292–299.

King, M. D., Howat, I. M., Jeong, S., Noh, M. J., Wouters, B., Noel, B., and van den Broeke, M. R. (2018). Seasonal to decadal variability in ice discharge from the greenland ice sheet. *The Cryosphere*, 12:3813 – 3825.

Kottmeier, C. and Engelbart, D. (1992). Generation and atmospheric heat exchange of coastal polynyas in the weddell sea. *Boundary-Layer Meteorology*, 60:207–234.

Larour, E., Seroussi, H., Morlighem, M., and Rignot, E. (2012). Continental scale, high order, high spatial resolution, ice sheet modeling using the Ice Sheet System Model (ISSM). *J. Geophys. Res.*, 117(F01022):1–20.

Le Brocq, A. M., Ross, N., Griggs, J. A., Bingham, R. G., Corr, H. F. J., Ferraccioli, F., Jenkins, A., Jordan, T. A., Payne, A. J., Rippin, D. M., and Siegert, M. J. (2013). Evidence from ice shelves for channelized meltwater flow beneath the Antarctic Ice Sheet. *Nat. Geosci.*, 6(11):945–948.

Lee, V., Cornford, S. L., and Payne, A. J. (2015). Initialization of an ice-sheet model for present-day Greenland. *Ann. Glaciol.*, 56(70):129–140.

Lemos, A., Shepherd, A., McMillan, M., and Hogg, A. (2018). Seasonal variations in the flow of land-terminating glaciers in central-west greenland using sentinel-1 imagery. *Remote Sensing*, 10(12):1878.

Lepp, A., Simkins, L., Anderson, J., Clark, R., Wellner, J., Hillenbrand, C., Smith, J., Lehrmann, A., Totten, R., Larter, R., et al. (2022). Sedimentary signatures of persistent subglacial meltwater drainage from thwaites glacier, antarctica. *Frontiers in Earth Science*, 10:863200.

Li, D., Jiang, L., and Huang, R. (2021). Hydrological and kinematic precursors of the 2017 calving event at the petermann glacier in greenland observed from multi-source remote sensing data. *Remote Sensing*, 13(4):591.

Lilien, D. A., Joughin, I., Smith, B., and Gourmelen, N. (2019). Melt at grounding line controls observed and future retreat of smith, pope, and kohler glaciers. *The Cryosphere*, 3(11):2817–2834.

Lliboutry, L. (1958). Glacier mechanics in the perfect plasticity theory. *Journal of Glaciology*, 3(23):162–169.

Lliboutry, L. (1968). General theory of subglacial cavitation and sliding of temperate glaciers. *Journal of Glaciology*, 7(49):21–58.

Lu, P., Li, Z., Cheng, B., and Leppäranta, M. (2011). A parameterization of the ice-ocean drag coefficient. *Journal of Geophysical Research: Oceans*, 116(C7).

Luckman, A. and Murray, T. (2005). Seasonal variation in velocity before retreat of Jakobshavn Isbræ, Greenland. *Geophysical Research Letters*, 32(8).

MacAyeal, D. R. (1985). Tidal rectification below the ross ice shelf, antarctica. *Antarctic Research Series*, 43:109–132.

MacAyeal, D. R. (1989). Large-scale ice flow over a viscous basal sediment: Theory and application to Ice Stream B, Antarctica. *J. Geophys. Res.*, 94(B4):4071–4087.

Mankoff, K. D., Solgaard, A., Colgan, W., Ahlstrøm, A. P., Khan, S. A., and Fausto, R. S. (2020). Greenland ice sheet solid ice discharge from 1986 through march 2020. *Earth Syst. Sci. Data*, 12(2):1367–1383.

Marshail, S. J. and Clarke, G. K. (1997). A continuum mixture model of ice stream thermomechanics in the laurentide ice sheet. *Journal of Geophysical Research: Solid Earth*, 102(B9):20–599.

Masson-Delmotte, V., Zhai, P., Pirani, A., Connors, S. L., Péan, C., Berger, S., Caud, N., Chen, Y., Goldfarb, L., Gomis, M., et al. (2021). Contribution of working group i to the sixth assessment report of the intergovernmental panel on climate change. *Climate Change*, 3:31.

McCormack, F. S., Roberts, J. L., Dow, C. F., Stål, T., Halpin, J. A., Reading, A. M., and Siegert, M. J. (2022). Fine-scale geothermal heat flow in antarctica can increase simulated subglacial melt estimates. *Geophysical Research Letters*, 49(15):e2022GL098539.

McPhee, M. G. (1979). The effect of the oceanic boundary layer on the mean drift of pack ice: Application of a simple model. *Journal of Physical Oceanography*, 9(2):388–400.

McPhee, M. G. (1989). Inferring ice/ocean surface roughness from horizontal current measurements. *Journal of Offshore Mechanics and Arctic Engineering*.

Mernild, S. H., Mote, T. L., and Liston, G. E. (2011). Greenland ice sheet surface melt extent and trends: 1960–2010. *Journal of Glaciology*, 57(204):621–628.

Miles, B. W., Stokes, C. R., and Jamieson, S. S. (2018). Velocity increases at cook glacier, east antarctica, linked to ice shelf loss and a subglacial flood event. *The Cryosphere*, 12(10):3123–3136.

Millan, R., Mouginot, J., Derkacheva, A., Rignot, E., Milillo, P., Ciraci, E., Dini, L., and Bjørk, A. (2022). Ongoing grounding line retreat and fracturing initiated at the petermann glacier ice shelf, greenland, after 2016. *The Cryosphere*, 16(7):3021–3031.

Millgate, T., Holland, P. R., Jenkins, A., and Johnson, H. L. (2013). The effect of basal channels on oceanic ice-shelf melting. *Journal of Geophysical Research: Oceans*, 118(12):6951–6964.

Moon, T., Ahlstrøm, A., Goelzer, H., Lipscomb, W., and Nowicki, S. (2018). Rising Oceans Guaranteed: Arctic Land Ice Loss and Sea Level Rise. *Curr. Clim. Change Rep.*, 4(3):211–222.

Moon, T., Joughin, I., and Smith, B. (2015). Seasonal to multiyear variability of glacier surface velocity, terminus position, and sea ice/ice mélange in northwest greenland. *Journal of Geophysical Research: Earth Surface*, 120(5):818–833.

Moon, T., Joughin, I., Smith, B., van den Broeke, M. R., van de Berg, W. J., Noel, B., and Usher, M. (2014). Distinct patterns of seasonal Greenland glacier velocity. *Geophysical Research Letters*, 41(20):7209–7216.

Morlighem, M. (2021). Icebridge bedmachine greenland, version 4. NASA National Snow and Ice Data Center Distributed Active Archive Center.

Morlighem, M., Bondzio, J., Seroussi, H., Rignot, E., Larour, E., Humbert, A., and Rebuffi, S.-A. (2016). Modeling of Store Gletscher's calving dynamics, West Greenland, in response to ocean thermal forcing. *Geophysical Research Letters*, 43(6):2659–2666.

Morlighem, M., Rignot, E., Mouginot, J., Seroussi, H., and Larour, E. (2014). Deeply incised submarine glacial valleys beneath the Greenland Ice Sheet. *Nat. Sci.*, 7(6):418–422.

Morlighem, M., Rignot, E., Seroussi, H., Larour, E., Ben Dhia, H., and Aubry, D. (2010). Spatial patterns of basal drag inferred using control methods from a full-Stokes and simpler models for Pine Island Glacier, West Antarctica. *Geophysical Research Letters*, 37(L14502):1–6.

Morlighem, M., Seroussi, H., Larour, E., and Rignot, E. (2013). Inversion of basal friction in Antarctica using exact and incomplete adjoints of a higher-order model. *J. Geophys. Res.*, 118(3):1746–1753.

Morlighem, M., Williams, C. N., Rignot, E., An, L., Arndt, J. E., Bamber, J. L., Catania, G., Chauché, N., Dowdeswell, J. A., Dorschel, B., Fenty, I., Hogan, K., Howat, I., Hubbard, A., Jakobsson, M., Jordan, T. M., Kjeldsen, K. K., Millan, R., Mayer, L., Mouginot, J., Noël, B. P. Y., O'Cofaigh, C., Palmer, S., Rysgaard, S., Seroussi, H., Siegert, M. J., Slabon, P., Straneo, F., van den Broeke, M. R., Weinrebe, W., Wood, M., and Zinglersen, K. B. (2017). BedMachine v3: Complete bed topography and ocean bathymetry mapping of Greenland from multi-beam echo sounding combined with mass conservation. *Geophysical Research Letters*, 44(21):11,051–11,061.

Morlighem, M., Wood, M., Seroussi, H., Choi, Y., and Rignot, E. (2019). Modeling the response of northwest Greenland to enhanced ocean thermal forcing and subglacial discharge. *The Cryosphere*, 13:723–734.

Motyka, R. J., Truffer, M., Fahnestock, M., Mortensen, J., Rysgaard, S., and Howat, I. (2011). Submarine melting of the 1985 Jakobshavn Isbrae floating tongue and the triggering of the current retreat. *J. Geophys. Res.*, 116:1–17.

Mouginot, J., Rignot, E., Bjørk, A. A., van den Broeke, M., Millan, R., Morlighem, M., Noël, B., Scheuchl, B., and Wood, M. (2019). Forty-six years of greenland ice sheet mass balance from 1972 to 2018. *Proceedings of the National Academy of Sciences*.

Mouginot, J., Rignot, E., Scheuchl, B., Fenty, I., Khazendar, A., Morlighem, M., Buzzi, A., and Paden, J. (2015). Fast retreat of Zachariæ Isstrøm, northeast Greenland. *Science*, 350(6266):1357–1361.

Münchow, A., Falkner, K. K., Melling, H., Rabe, B., and Johnson, H. L. (2011). Ocean warming of nares strait bottom waters. *Oceanography*, 24(3):114.

Münchow, A., Padman, L., and Fricker, H. A. (2014). Interannual changes of the floating ice shelf of Petermann Gletscher, North Greenland, from 2000 to 2012. *Journal of Glaciology*, 60(221):489–499.

Nakayama, Y., Cai, C., and Seroussi, H. (2021). Impact of subglacial freshwater discharge on pine island ice shelf. *Geophysical Research Letters*, 48(18):e2021GL093923.

Nias, I., Cornford, S., and Payne, A. (2018). New mass-conserving bedrock topography for pine island glacier impacts simulated decadal rates of mass loss. *Geophysical Research Letters*, 45(7):3173–3181.

Nick, F. M., Luckman, A., Vieli, A., Van Der Veen, C. J., Van As, D., Van De Wal, R. S. W., Pattyn, F., Hubbard, A. L., and Floricioiu, D. (2012). The response of Petermann Glacier, Greenland, to large calving events, and its future stability in the context of atmospheric and oceanic warming. *Journal of Glaciology*, 58(208):229–239.

Nienow, P. W., Hubbard, A. L., Hubbard, B. P., Chandler, D. M., Mair, D. W. F., Sharp, M. J., and Willis, I. C. (2005). Hydrological controls on diurnal ice flow variability in valley glaciers. *J. Geophys. Res. - Earth Surface*, 110(F4).

Nienow, P. W., Sole, A. J., Slater, D. A., and Cowton, T. R. (2017). Recent Advances in Our Understanding of the Role of Meltwater in the Greenland Ice Sheet System. *Curr. Clim. Change Rep.*, 3:330–344.

Nitsche, F. O., Gohl, K., Larter, R. D., Hillenbrand, C.-D., Kuhn, G., Smith, J., Jacobs, S., Anderson, J., and Jakobsson, M. (2013). Paleo ice flow and subglacial meltwater dynamics in pine island bay, west antarctica. *The Cryosphere*, 7(1):249–262.

Nye, J. F. (1976). Water flow in glaciers: jokulhlaups, tunnels and veins. *Journal of Glaciology*, 17(76):181–207.

O'Neill, B. C., Tebaldi, C., Van Vuuren, D. P., Eyring, V., Friedlingstein, P., Hurtt, G., Knutti, R., Kriegler, E., Lamarque, J.-F., Lowe, J., et al. (2016). The scenario model intercomparison project (scenariomip) for cmip6. *Geoscientific Model Development*, 9(9):3461–3482.

Parizek, B. R. and Alley, R. B. (2004). Implications of increased greenland surface melt under global-warming scenarios: ice-sheet simulations. *Quaternary Science Reviews*, 23(9-10):1013–1027.

Park, J., Gourmelen, N., Shepherd, A., Kim, S., Vaughan, D. G., and Wingham, D. (2013). Sustained retreat of the pine island glacier. *Geophysical Research Letters*, 40(10):2137–2142.

Pelle, T., Morlighem, M., and Bondzio, J. H. (2019). Brief communication: PICOP, a new ocean melt parameterization under ice shelves combining PICO and a plume model. *The Cryosphere*, 13(3):1043–1049.

Pelle, T., Morlighem, M., Nakayama, Y., and Seroussi, H. (2021). Widespread Grounding Line Retreat of Totten Glacier, East Antarctica, Over the 21st Century. *Geophysical Research Letters*, 48(17).

Pritchard, H. D., Arthern, R. J., Vaughan, D. G., and Edwards, L. A. (2009). Extensive dynamic thinning on the margins of the Greenland and Antarctic ice sheets. *Nature*, 461:971–975.

Pritchard, H. D., Ligtenberg, S. R. M., Fricker, H. A., Vaughan, D. G., van den Broeke, M. R., and Padman, L. (2012). Antarctic ice-sheet loss driven by basal melting of ice shelves. *Nature*, 484(7395):502–505.

Prothro, L. O., Majewski, W., Yokoyama, Y., Simkins, L. M., Anderson, J. B., Yamane, M., Miyairi, Y., and Ohkouchi, N. (2020). Timing and pathways of east antarctic ice sheet retreat. *Quaternary Science Reviews*, 230:106166.

Quincey, D., Copland, L., Mayer, C., Bishop, M., Luckman, A., and Belò, M. (2009). Ice velocity and climate variations for baltoro glacier, pakistan. *Journal of Glaciology*, 55(194):1061–1071.

Rathmann, N., Hvidberg, C., Solgaard, A., Grinsted, A., Gudmundsson, G. H., Langen, P. L., Nielsen, K., and Kusk, A. (2017). Highly temporally resolved response to seasonal surface melt of the zachariae and 79n outlet glaciers in northeast greenland. *Geophysical Research Letters*, 44(19):9805–9814.

Reese, R., Albrecht, T., Mengel, M., Asay-Davis, X., and Winkelmann, R. (2018). Antarctic sub-shelf melt rates via pico. *The Cryosphere*, 12(6):1969–1985.

Rignot, E. (1996). Tidal motion, ice velocity and melt rate of petermann gletscher, greenland, measured from radar interferometry. *Journal of Glaciology*, 42(142):476–485.

Rignot, E., An, L., Chauche, N., Morlighem, M., Jeong, S., Wood, M., Mouginot, J., Willis, J. K., Klaucke, I., Weinrebe, W., et al. (2021). Retreat of humboldt gletscher, north greenland, driven by undercutting from a warmer ocean. *Geophysical research letters*, 48(6):e2020GL091342.

Rignot, E., Bamber, J. L., Van Den Broeke, M. R., Davis, C., Li, Y., Van De Berg, W. J., and Van Meijgaard, E. (2008a). Recent antarctic ice mass loss from radar interferometry and regional climate modelling. *Nature geoscience*, 1(2):106–110.

Rignot, E., Box, J. E., Burgess, E., and Hanna, E. (2008b). Mass balance of the Greenland ice sheet from 1958 to 2007. *Geophysical Research Letters*, 35(20):1–5.

Rignot, E., Gogineni, S., Joughin, I., and Krabill, W. (2001). Contribution to the glaciology of northern Greenland from satellite radar interferometry. *J. Geophys. Res.*, 106(D24):34007–34019.

Rignot, E., Kobbes, M., and Velicogna, I. (2010). Rapid submarine melting of the calving faces of west greenland glaciers. *Nature Geoscience*, 3(3):187–191.

Rignot, E., Mouginot, J., Morlighem, M., Seroussi, H., and Scheuchl, B. (2014). Widespread, rapid grounding line retreat of pine island, thwaites, smith, and kohler glaciers, west antarctica, from 1992 to 2011. *Geophysical Research Letters*, 41(10):3502–3509.

Rignot, E., Mouginot, J., Scheuchl, B., Van Den Broeke, M., Van Wessem, M. J., and Morlighem, M. (2019). Four decades of antarctic ice sheet mass balance from 1979–2017. *Proceedings of the National Academy of Sciences*, 116(4):1095–1103.

Rignot, E. and Steffen, K. (2008). Channelized bottom melting and stability of floating ice shelves. *Geophysical Research Letters*, 35(2):1–5.

Rignot, E., Velicogna, I., van den Broeke, M. R., Monaghan, A., and Lenaerts, J. (2011). Acceleration of the contribution of the Greenland and Antarctic ice sheets to sea level rise. *Geophysical Research Letters*, 38:1–5.

Rignot, E., Xu, Y., Menemenlis, D., Mouginot, J., Scheuchl, B., Li, X., Morlighem, M., Seroussi, H., den Broeke, M. v., Fenty, I., et al. (2016). Modeling of ocean-induced ice melt rates of five west greenland glaciers over the past two decades. *Geophysical Research Letters*, 43(12):6374–6382.

Robel, A. A., Wilson, E., and Seroussi, H. (2022). Layered seawater intrusion and melt under grounded ice. *The Cryosphere*, 16(2):451–469.

Roberts, J., Galton-Fenzi, B. K., Paolo, F. S., Donnelly, C., Gwyther, D. E., Padman, L., Young, D., Warner, R., Greenbaum, J., Fricker, H. A., et al. (2018). Ocean forced variability of totten glacier mass loss. *Geological Society, London, Special Publications*, 461(1):175–186.

Robin, G. d. Q., Evans, S., and Bailey, J. T. (1969). Interpretation of radio echo sounding in polar ice sheets. *Philosophical Transactions of the Royal Society of London. Series A, Mathematical and Physical Sciences*, 265(1166):437–505.

Robinson, D. E., Menzies, J., Wellner, J. S., and Clark, R. W. (2021). Subglacial sediment deformation in the ross sea, antarctica. *Quaternary Science Advances*, 4:100029.

Rosenau, R., Schwalbe, E., Maas, H.-G., Baessler, M., and Dietrich, R. (2013). Grounding line migration and high-resolution calving dynamics of jakobshavn isbræ, west greenland. *Journal of Geophysical Research: Earth Surface*, 118(2):382–395.

Röthlisberger, H. (1972). Water pressure in intra-and subglacial channels. *Journal of Glaciology*, 11(62):177–203.

Rückamp, M., Greve, R., and Humbert, A. (2019). Comparative simulations of the evolution of the Greenland ice sheet under simplified Paris Agreement scenarios with the models SICOPOLIS and ISSM. *Polar Science*, 21:14–25.

Scheuchl, B., Mouginot, J., Rignot, E., Morlighem, M., and Khazendar, A. (2016). Grounding line retreat of pope, smith, and kohler glaciers, west antarctica, measured with sentinel-1a radar interferometry data. *Geophysical Research Letters*, 43(16):8572–8579.

Schoof, C. (2005). The effect of cavitation on glacier sliding. *Proc. R. Soc. A*, 461(2055):609–627.

Schoof, C. (2010). Coulomb friction and other sliding laws in a higher-order glacier flow model. *Math. Models Methods Appl. Sci.*, 20(1):157–189.

Schoof, C., Hewitt, I. J., and Werder, M. A. (2012). Flotation and free surface flow in a model for subglacial drainage. Part 1. Distributed drainage. *J. Fluid Mech.*, 702:126–156.

Sergienko, O. V., Goldberg, D. N., and Little, C. M. (2013). Alternative ice shelf equilibria determined by ocean environment. *J. Geophys. Res.*, 118(2):970–981.

Seroussi, H. and Morlighem, M. (2018). Representation of basal melting at the grounding line in ice flow models. *The Cryosphere*, 12:3085–3096.

Seroussi, H., Morlighem, M., Rignot, E., Khazendar, A., Larour, E., and Mouginot, J. (2013). Dependence of century-scale projections of the Greenland ice sheet on its thermal regime. *Journal of Glaciology*, 59(218):1024–1034.

Seroussi, H., Nakayama, Y., Larour, E., Menemenlis, D., Morlighem, M., Rignot, E., and Khazendar, A. (2017). Continued retreat of thwaites glacier, west antarctica, controlled by bed topography and ocean circulation. *Geophysical Research Letters*, 44(12):6191–6199.

Seroussi, H., Nowicki, S., Payne, A. J., Goelzer, H., Lipscomb, W. H., Abe-Ouchi, A., Agosta, C., Albrecht, T., Asay-Davis, X., Barthel, A., et al. (2020). Ismip6 antarctica: a multi-model ensemble of the antarctic ice sheet evolution over the 21st century. *The Cryosphere*, 14(9):3033–3070.

Shean, D. E., Joughin, I. R., Dutrieux, P., Smith, B. E., and Berthier, E. (2019). Ice shelf basal melt rates from a high-resolution digital elevation model (dem) record for pine island glacier, antarctica. *The Cryosphere*, 13(10):2633–2656.

Ship, S., Anderson, J., and Domack, E. (1999). Late pleistocene–holocene retreat of the west antarctic ice-sheet system in the ross sea: part 1—geophysical results. *Geological Society of America Bulletin*, 111(10):1489–1516.

Shirasawa, K. (1986). Water stress and ocean current measurements under first-year sea ice in the canadian arctic. *Journal of Geophysical Research: Oceans*, 91(C12):14305–14316.

Shreve, R. L. (1972). Movement of water in glaciers. *Journal of Glaciology*, 11(62):205–214.

Simkins, L. M., Anderson, J. B., Greenwood, S. L., Gonnermann, H. M., Prothro, L. O., Halberstadt, A. R. W., Stearns, L. A., Pollard, D., and DeConto, R. M. (2017). Anatomy of a meltwater drainage system beneath the ancestral east antarctic ice sheet. *Nature Geoscience*, 10(9):691–697.

Simkins, L. M., Greenwood, S. L., Winsborrow, M. C., Bjarnadóttir, L. R., and Lepp, A. P. (2023). Advances in understanding subglacial meltwater drainage from past ice sheets. *Annals of Glaciology*, pages 1–5.

Smith, L. C., Chu, V. W., Yang, K., Gleason, C. J., Pitcher, L. H., Rennermalm, A. K., Legleiter, C. J., Behar, A. E., Overstreet, B. T., Moustafa, S. E., Tedesco, M., Forster, R. R., LeWinter, A. L., Finnegan, D. C., Sheng, Y., and Balog, J. (2015). Efficient meltwater drainage through supraglacial streams and rivers on the southwest Greenland ice sheet. *Proceedings of the National Academy of Sciences*, 112(4):1001–1006.

Sole, A. J., Mair, D. W. F., Nienow, P. W., Bartholomew, I. D., King, M. A., Burke, M. J., and Joughin, I. (2011). Seasonal speedup of a Greenland marine-terminating outlet glacier forced by surface melt-induced changes in subglacial hydrology. *J. Geophys. Res.*, 116:1–11.

Sommers, A., Rajaram, H., and Morlighem, M. (2018). SHAKTI: Subglacial Hydrology and Kinetic, Transient Interactions v1.0. *Geosci. Model Dev.*, 11(7):2955–2974.

Stearns, L. A., Smith, B. E., and Hamilton, G. S. (2008). Increased flow speed on a large east antarctic outlet glacier caused by subglacial floods. *Nature Geoscience*, 1(12):827–831.

Storrar, R. D., Stokes, C. R., and Evans, D. J. (2014). Increased channelization of subglacial drainage during deglaciation of the laurentide ice sheet. *Geology*, 42(3):239–242.

Straneo, F., Hamilton, G. S., Stearns, L. A., and Sutherland, D. A. (2016). Connecting the Greenland Ice Sheet and the Ocean, a case study of Helheim Glacier and Sermilik Fjord. *Oceanography*, 29(4, SI):34–45.

Sun, S., Pattyn, F., Simon, E., Albrecht, T., Cornford, S., Calov, R., Dumas, C., Gillet-Chaulet, F., Goelzer, H., Golledge, N. R., Greve, R., Hoffman, M., Humbert, A., Kazmierczak, E., Kleiner, T., Leguy, G. R., Lazeroms, W. M. J., Lipscomb, W. H., Martin, D., Morlighem, M., Nowicki, S., Pollard, D., Price, S., Quiquet, A., Seroussi, H., Schlemm, T., Sutter, J., Van De Wal, R. S. W., and Zhang, T. (2020). Antarctic ice sheet response to sudden and sustained ice shelf collapse (ABUMIP). *Journal of Glaciology*, pages 1–14.

Tedesco, M. and Fettweis, X. (2020). Unprecedented atmospheric conditions (1948–2019) drive the 2019 exceptional melting season over the greenland ice sheet. *The Cryosphere*, 14(4):1209–1223.

Tedesco, M., Fettweis, X., Mote, T., Wahr, J., Alexander, P., Box, J. E., and Wouters, B. (2013). Evidence and analysis of 2012 Greenland records from spaceborne observations, a regional climate model and reanalysis data. *The Cryosphere*, 7(2):615–630.

Thøgersen, K., Gilbert, A., Bouchayer, C., and Schuler, T. V. (2021, in press.). Glacier surges controlled by the close interplay between subglacial friction and drainage. *Nature*.

Thoma, M., Jenkins, A., Holland, D., and Jacobs, S. (2008). Modelling Circumpolar Deep Water intrusions on the Amundsen Sea continental shelf, Antarctica. *Geophysical Research Letters*, 35(18):1–6.

Todd, J. and Christoffersen, P. (2014). Are seasonal calving dynamics forced by buttressing from ice mélange or undercutting by melting? Outcomes from full-Stokes simulations of Store Glacier, West Greenland. *The Cryosphere*, 8(6):2353–2365.

Tulaczyk, S., Kamb, W. B., and Engelhardt, H. F. (2000). Basal mechanics of ice stream b, west antarctica: 1. till mechanics. *Journal of Geophysical Research: Solid Earth*, 105(B1):463–481.

Välisuo, I., Vihma, T., Pirazzini, R., and Schäfer, M. (2018). Interannual variability of atmospheric conditions and surface melt in greenland in 2000–2014. *Journal of Geophysical Research: Atmospheres*, 123(18):10–443.

Van den Broeke, M. R., Enderlin, E. M., Howat, I. M., Kuipers Munneke, P., Noël, B. P., Van De Berg, W. J., Van Meijgaard, E., and Wouters, B. (2016). On the recent contribution of the greenland ice sheet to sea level change. *The Cryosphere*, 10(5):1933–1946.

van der Wel, N., Christoffersen, P., and Bougamont, M. (2013). The influence of subglacial hydrology on the flow of kamb ice stream, west antarctica. *Journal of Geophysical Research: Earth Surface*, 118(1):97–110.

Vaughan, D. G., Corr, H. F. J., Bindschadler, R. A., Dutrieux, P., Gudmundsson, G. H., Jenkins, A., Newman, T., Vornberger, P., and Wingham, D. J. (2012). Subglacial melt channels and fracture in the floating part of Pine Island Glacier, Antarctica. *Journal of Geophysical Research: Earth Surface*, 117(F3):1–10.

Vieli, A., Funk, M., and Blatter, H. (2001). Flow dynamics of tidewater glaciers: a numerical modelling approach. *Journal of Glaciology*, 47(159):595–606.

Vieli, A. and Payne, A. J. (2005). Assessing the ability of numerical ice sheet models to simulate grounding line migration. *Journal of Geophysical Research: Earth Surface*, 110(F1):1–18.

Vijay, S., Khan, S. A., Kusk, A., Solgaard, A. M., Moon, T., and Bjork, A. A. (2019). Resolving seasonal ice velocity of 45 greenlandic glaciers with very high temporal details. *Geophysical Research Letters*, 46(3):1485–1495.

Walker, R. T., Dupont, T. K., Parizek, B. R., and Alley, R. B. (2008). Effects of basal-melting distribution on the retreat of ice-shelf grounding lines. *Geophysical Research Letters*, 35(17):1–5.

Washam, P., Nicholls, K. W., Münchow, A., and Padman, L. (2019). Summer surface melt thins petermann gletscher ice shelf by enhancing channelized basal melt. *Journal of Glaciology*, 65(252):662–674.

Watkins, R. H., Bassis, J. N., and Thouless, M. (2021). Roughness of ice shelves is correlated with basal melt rates. *Geophysical Research Letters*, 48(21).

Weertman, J. (1957). On the sliding of glaciers. *Journal of Glaciol.*, 3:33–38.

Wei, W., Blankenship, D. D., Greenbaum, J. S., Gourmelen, N., Dow, C. F., Richter, T. G., Greene, C. A., Young, D. A., Lee, S., Kim, T.-W., Lee, W. S., and Assmann, K. M. (2020). Getz Ice Shelf melt enhanced by freshwater discharge from beneath the West Antarctic Ice Sheet. *The Cryosphere*, 14:1399–1408.

Werder, M. A., Hewitt, I. J., Schoof, C. G., and Flowers, G. E. (2013). Modeling channelized and distributed subglacial drainage in two dimensions. *J. Geophys. Res.*, 118:1–19.

Willis, I. C., Pope, E. L., Gwendolyn, J.-M., Arnold, N. S., and Long, S. (2016). Drainage networks, lakes and water fluxes beneath the antarctic ice sheet. *Annals of Glaciology*, 57(72):96–108.

Wilson, E. A., Wells, A. J., Hewitt, I. J., and Cenedese, C. (2020). The dynamics of a subglacial salt wedge. *Journal of Fluid Mechanics*, 895:A20.

Wilson, N., Straneo, F., and Heimbach, P. (2017). Satellite-derived submarine melt rates and mass balance (2011–2015) for Greenland's largest remaining ice tongues. *The Cryosphere*, 11:2773–2782.

Wood, M., Rignot, E., Fenty, I., An, L., Bjørk, A., van den Broeke, M., Cai, C., Kane, E., Menemenlis, D., Millan, R., et al. (2021). Ocean forcing drives glacier retreat in greenland. *Science Advances*, 7(1):eaba7282.

Wood, M., Rignot, E., Fenty, I., Menemenlis, D., Millan, R., Morlighem, M., Mouginot, J., and Seroussi, H. (2018). Ocean-induced melt triggers glacier retreat in Northwest Greenland. *Geophys. Res. Lett.*, 45(16):8334–8342.

Xie, S., Dixon, T. H., Voytenko, D., Deng, F., and Holland, D. M. (2018). Grounding line migration through the calving season at jakobshavn isbræ, greenland, observed with terrestrial radar interferometry. *The Cryosphere*, 12(4):1387–1400.

Xu, Y., Rignot, E., Fenty, I., Menemenlis, D., and Flexas, M. M. (2013). Subaqueous melting of Store Glacier, west Greenland from three-dimensional, high-resolution numerical modeling and ocean observations. *Geophys. Res. Lett.*, 40(17):4648–4653.

Zwally, H. J., Abdalati, W., Herring, T., Larson, K., Saba, J., and Steffen, K. (2002). Surface Melt-Induced Acceleration of Greenland Ice-Sheet Flow. *Science*, 297(5579):218–222.

Appendix A

Supplemental Information: Seasonal acceleration of Petermann Glacier, Greenland, from changes in subglacial hydrology

To model the effect of subglacial hydrology on the seasonal dynamics of Petermann Glacier, we use the Glacier Drainage System Model (GlaDS) (Werder et al., 2013) implemented within the Ice-sheet and Sea-level System Model (ISSM) (Larour et al., 2012) with one-way coupling. We use GlaDS to calculate an effective pressure seasonal cycle from daily runoff input from the regional climate model, MAR (Modèle Atmosphérique Régional), (Fettweis et al., 2017) and specific datasets from MARv3.9 (Tedesco and Fettweis, 2020). We then force the ice flow model with effective pressure to calculate ice velocity using a regularized coulomb friction law (Gagliardini et al., 2007; Schoof, 2005; Joughin et al., 2019). The following details the model setup for GlaDS and ISSM, and then includes the captions for the video files displaying transient model results.

A.1 GlaDS Hydrology Model Setup

To model Petermann's subglacial hydrology we use a sub-region of the glacier's drainage basin that's roughly 80 km by 80 km. We exclude all floating ice and regions of relatively thin ice, but extend past the equilibrium line altitude to ensure that the full region expected to experience evolving seasonal hydrology is included. We use a mesh composed of 3,265 elements with a resolution ranging between 500 m and 2,000 m in the hydrology model, which is shown in Figure A.1A. Both the hydrology model domain and the ice flow model domain can be seen in Figure A.1B.

BedMachine v3 data are used to define ice geometry in the model (Morlighem et al., 2017). BedMachine v4 is avaliable, but does not vary significantly over our model domain (Figure A.2). ISMIP6 data is used to set sliding velocity (Figure A.3A) and basal melt (Figure A.3B) Goelzer et al. (2018). During model setup, we added an upper limit of 500 m/year to the velocity field to help with numerical stability. After obtaining a stable model setup, we were able to remove the limit on sliding velocity and run the model without encountering convergence issues. The initial hydraulic potential is defined using the model geometry. We take half the overburden pressure (MPa) as the initial hydraulic potential, $\phi_o = 0.5\rho_i g H$. Temperature and initial sheet thickness do not vary spatially, and are -2°C and 0.03 m respectively. Additional parameters required for GlaDS are described in Table A.1 below.

In our initial model setup we worked with two distributions of moulin locations, one with 15 locations (Figure A.4B) and one with 36 (Figure A.4A). Both spanned roughly the same geographical area and had randomly distributed point locations. We chose to continue this work using the larger number of moulins because using a larger number of point sources for meltwater runoff entering the system seemed to help the model with numerical stability. Our model could be improved by using satellite images to identify locations for point sources of runoff, and then integrating the runoff over the area surrounding each moulin separately instead of evenly dividing the total runoff integrated over the full model domain among a somewhat arbitrarily chosen number of moulin locations. This is something that will be considered in future work, but was outside of the scope of this paper. We ran several simulations to test the sensitivity of our model to the method by which melt is injected to the bed. The results of these simulations can be seen in section 5 of the supplemental document. In general, our model results did not seem particularly sensitive to how we chose to introduce meltwater runoff, however, this choice continued to impact numerical stability.

BedMachine v3 provides the ice geometry necessary in the model parameterization, including the glacier bed elevation. However, we found it necessary, again for numerical stability, to smooth the bed topography before conducting transient simulations. Rather than smooth the bed across the full model domain, we used the Matlab-based software, TopoToolBox, to isolate the areas in the bed topography where pooling would occur based on hydraulic potential. The bed was raised in these specific areas but was left unaltered elsewhere. Figure A.5A shows the bed elevation below sea-level provided by BedMachine v3, and Figure A.5B shows the difference between the bed elevation used to calculate hydrology and BedMachine. Notably, there are several deep depressions along Petermann's main trunk of fast flowing ice where the bed elevation changes several hundred meters over a relatively short distance, which is difficult for the model to resolve. We raised the bed in these locations by a maximum of 115 m, which preserved the bulk of the bed topography but allowed the model to run without convergence issues.

We use the same meltwater runoff forcing in all of the hydrology simulations run. Notable dates from the integrated time-series of runoff over the three year time period for which we compare model velocity to observations can be seen in Table A.2. We use these dates to show and discuss the results from various GlaDS simulations. All hydrology model simulations in the sensitivity tests are run for 4 years, from 2015 to the end of 2018. We tested to see if one year is long enough for the model to spin up by comparing results to a longer run that

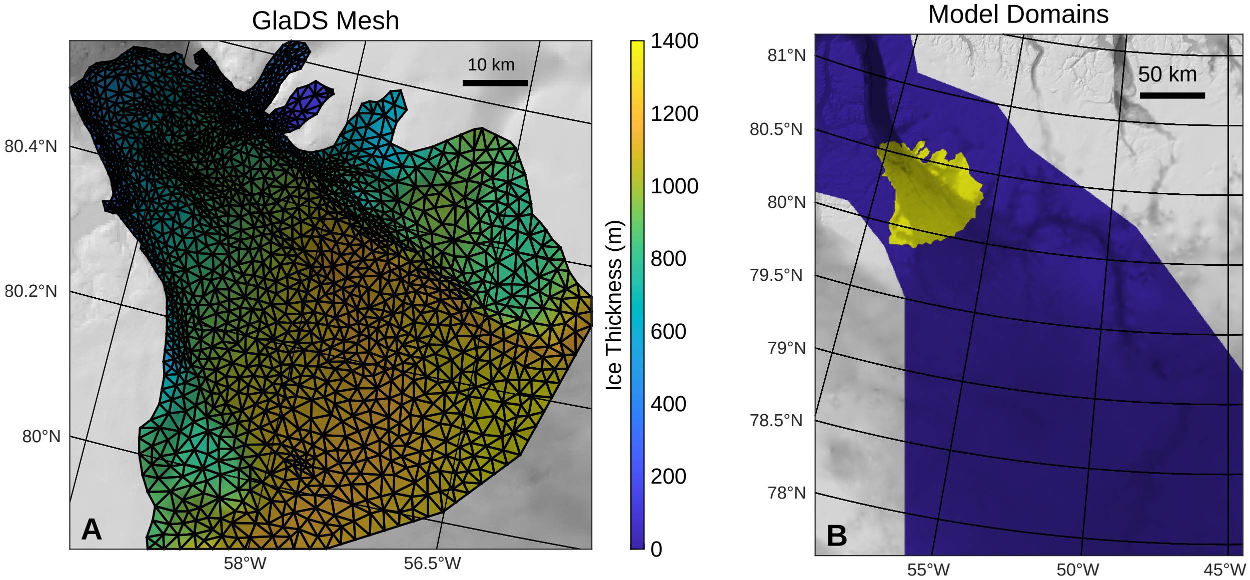

Figure A.1: (A) Model domain for the Glacier Drainage System Model (GlaDS) and (B) extent of the model domains overlain on a Hillshade image of bed elevation. The ice flow model domain is blue and GlaDS model domain is yellow. Mesh resolution is varied based on ice surface velocity.

was allowed to spin up for 8 years using the same hydrology parameters as are used in the main results. Figure A.6 shows the effective pressure results compared between the 4 year run and the 11 year run. No significant difference was found.

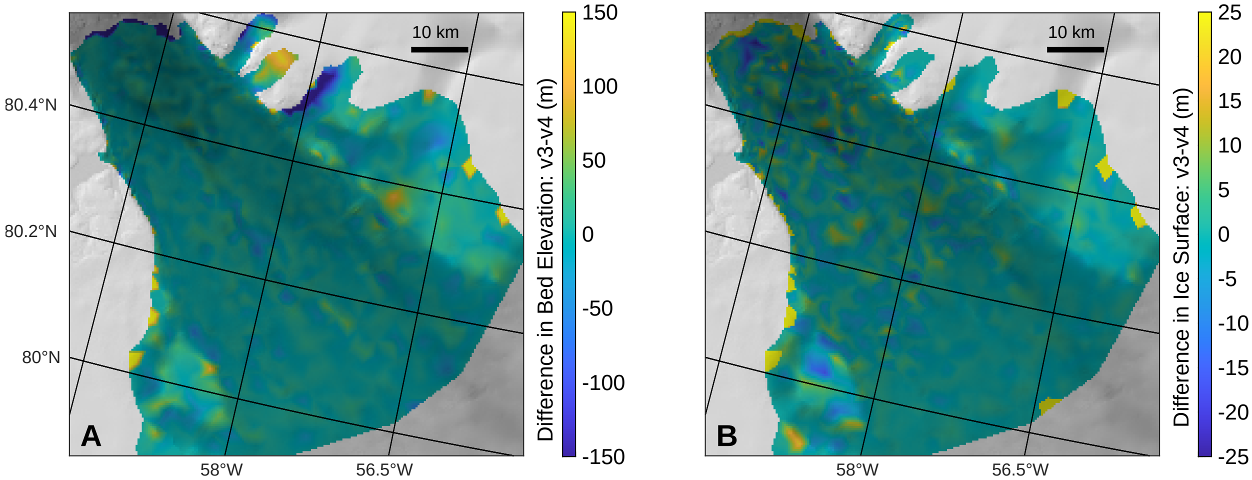

Figure A.2: (A) Differences in bed elevation and (B) surface elevation between bedMachine v3 and bedMachine v4. Note that the offset near the grounding line is the result of a shift in grounding line position from small differences in hydrostatic equilibrium, not a > 150 m shift in bed elevation. Maximum and minimum differences in bed elevation are 431 m and -533 m respectively. Maximum and minimum differences in surface elevation are 1245 m and -25 m, respectively. All of the larger adjustments in surface elevation are along the edges of the hydrology model domain, where the ice is the thickest. Generally, the largest changes occur where we see large gradients.

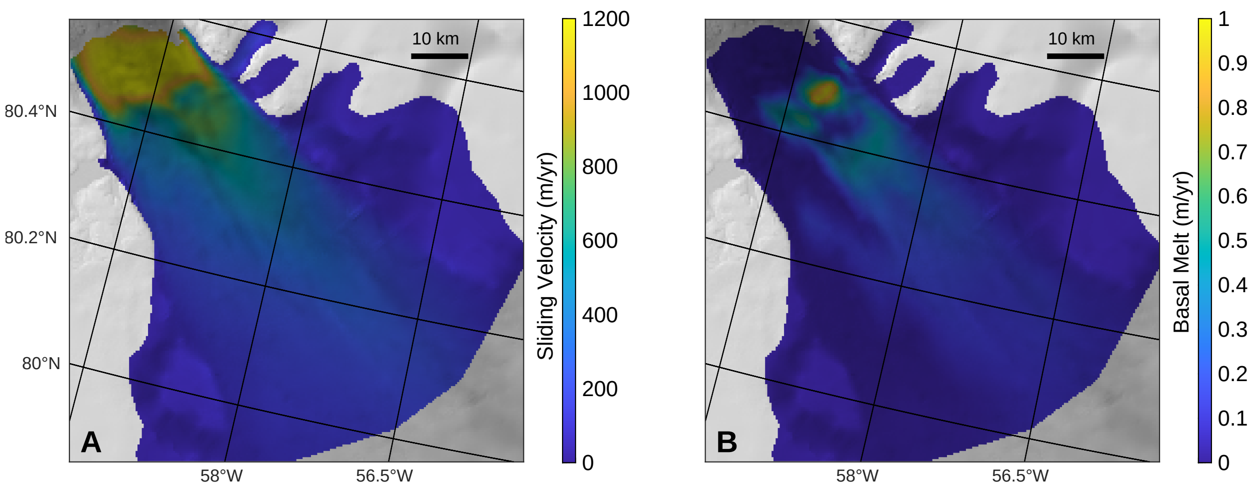

Figure A.3: (A) Basal sliding velocity and (B) basal melt rates used by GlaDS to calculate subglacial hydrology. Sliding velocity and basal melt values were obtained from ISMIP6 data Goelzer et al. (2018).

Table A.1: GlaDS Model Parameters

Symbol	Description	Value	Units
e_v	Englacial void ratio	10^{-5}	-
c_t	Pressure melt coefficient	7.5×10^{-8}	K Pa^{-1}
L	Latent heat of fusion	3.34×10^{5}	J kg^{-1}
A	Ice flow constant	2.5×10^{-25}	Pa^{n} s^{-1}
n	Glen's flow constant	3	-
g	Gravitational acceleration	9.81	m s^{-2}
h_r	Bedrock bump height	0.1	m
l_r	Cavity spacing	2.0	m
k_s	Sheet conductivity	0.02	m$^{7/2}$ kg$^{-1/2}$
k_c	Channel conductivity	0.2	m$^{3/2}$ kg$^{-1/2}$

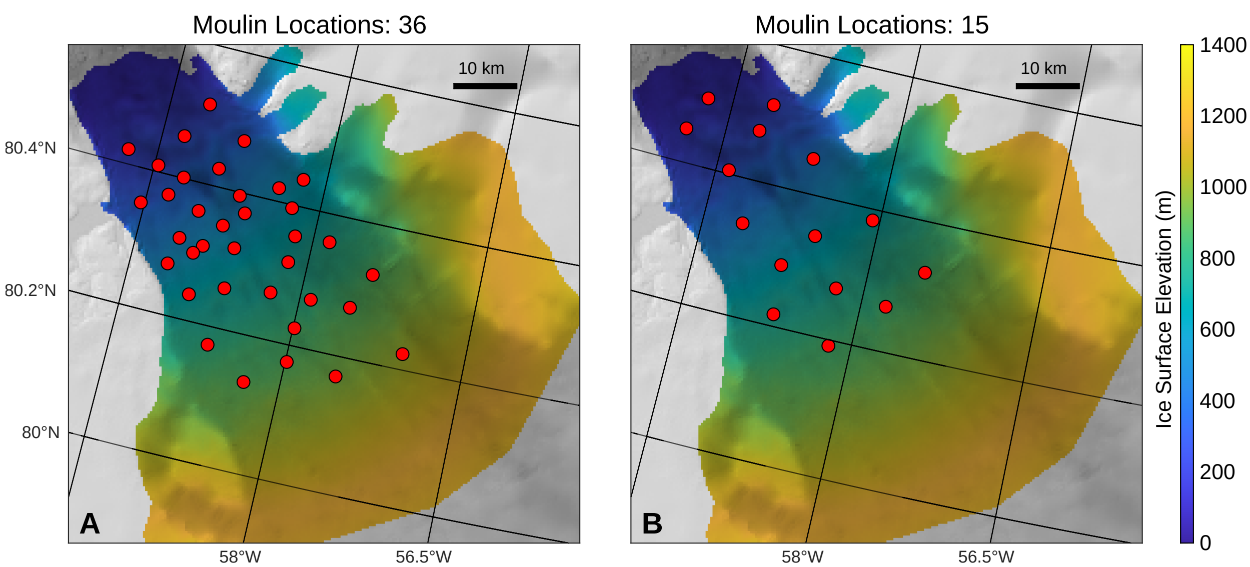

Figure A.4: Two configurations of moulin locations (red circles) mapped over surface elevation; (A) one with 36 moulins, and (B) the other with 15 moulins. We use the 36 moulin configuration in all simulations unless otherwise stated. The 15 moulin configuration is used to test model sensitivity to melt injection. Moulins act as point sources for meltwater runoff to reach the glacier bed. We choose random locations at or below the 900 m surface ice elevation contour and at least 5 km away from the grounding line.

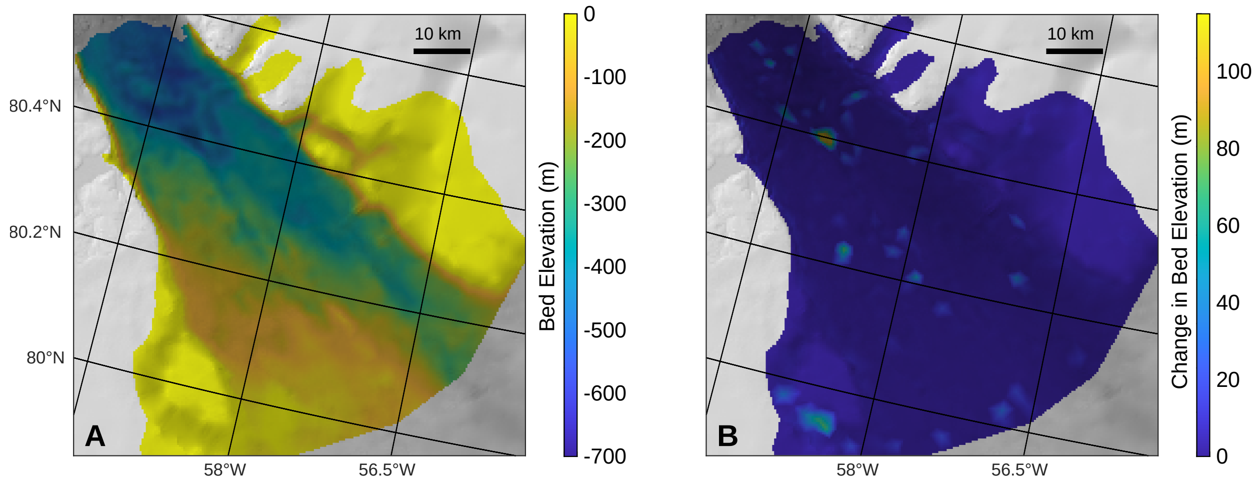

Figure A.5: (A) Adjusted bed elevation after smoothing was applied, and (B) the difference between the adjusted bed and BedMachine glacier base values. TopoToolBox was used to target specific regions that were causing numerical instability rather using spatial averaging across the full model domain. Most of the model domain remained unaltered, while the bed is raised in pockets of the topography that exhibit sharp decreases in elevation and would cause substantial pooling in the model.

Table A.2: Characterization of melt season for the 3 years examined in this study. The volume flux of melt water runoff integrated over the full hydrology modeling domain is listed for notable dates. All runoff values are in units of m^3/s.

	2016		2017		2018	
	Date	Runoff	Date	Runoff	Date	Runoff
1st day > 1 m^3/s	June 5th	1.622	June 8th	1.033	June 10th	1.289
1st day > 100 m^3/s	June 11th	113.74	June 15th	120.871	June 19th	130.054
Maximum	July 19th	1038.08	Aug 1st	715.191	Aug 7th	452.107
1st day < 100 m^3/s	Aug 12th	91.997	Aug 15th	99.042	Aug 21st	82.282
1st day < 1 m^3/s	Sept 8th	0.8705	Aug 29th	0.389	Sept 4th	0.917
	2016		2017		2018	
Minimum N	July 12th		Aug 1st		Aug 8th	

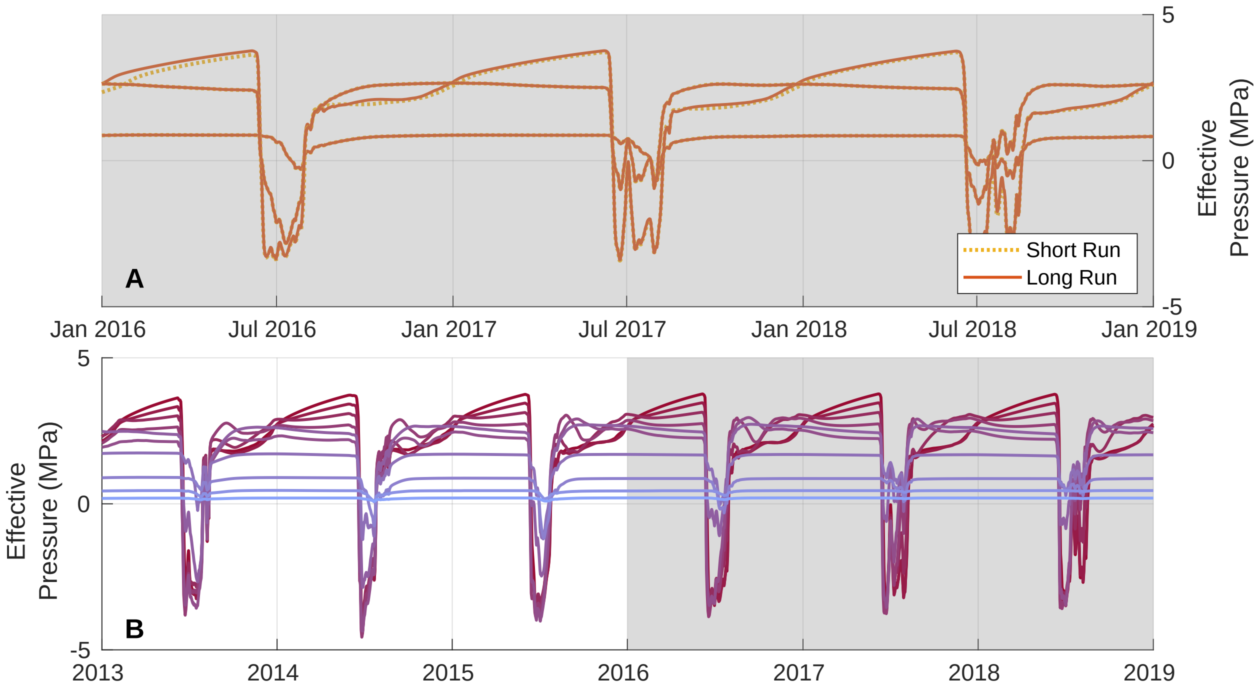

Figure A.6: Comparison of GlaDS effective pressure results obtained from simulations when the model spins up for different lengths of time (A), and effective pressure results at various points for the last 6 years of the long run (B), which starts in 2008. We do not see a significant difference in corresponding results when we allow longer than 1 year for model spin up.

A.2 Ice Sheet Model Setup

We use ISSM (Larour et al., 2012) to model seasonal acceleration driven by varying effective pressure. We use a different mesh to model velocity than we used to model the evolution of subglacial hydrology for Petermann. Figure A.1B shows the extent of the two model domains. The ice flow model domain includes Petermann's floating ice tongue and the fjord side walls, which were excluded for the hydrology model. The domain also extends approximately to the ice divide. We use the Shelfy Stream Approximation to calculate ice flow (MacAyeal, 1989). The mesh resolution varies based on the initial velocity field between 500 m to a maximum of 7,500 m, and has a total of about 15,000 elements. Elements that are within the smaller hydrology model domain have a maximum size of 2,000 m.

We use a double inversion of rheology over floating ice and basal friction under grounded ice with a regularized coulomb friction law (Gagliardini et al., 2007; Schoof, 2005; Joughin et al., 2019) to initialize the ice flow model. In the model inversion, the ice viscosity and friction coefficient are tuned to minimize error between the modeled and observed surface velocities. We isolated the floating ice within approximately 3 km of the fjord side walls and imposed an upper limit of 3.735 $\times 10^8 Pas^{-1/3}$ on the rheology factor B of this region. Doing so gave us a better fit to observations, and is justified under the assumption that this region is highly damaged. Cracks and damage are not represented in this model through other means. Figure A.7A shows the final result of the inversion for rheology on Petermann's ice tongue. We use a constant ice rheology, $B = 1.6824 \times 10^8 Pas^{-1/3}$ over the grounded ice which corresponds to an ice temperature of $-15°$C. The inversion results for the friction coefficient are shown over the full ice flow model domain in Figure A.7B. All floating ice has an forced friction coefficient of zero.

We use a regularized coulomb friction law (Schoof, 2005; Gagliardini et al., 2007) to incorporate time-dependent effective pressure into the ice flow model. We also experimented with

Budd's law (Budd et al., 1979; Bindschadler, 1983), where basal shear stress, τ_b, increases with both increasing basal velocity, u_b, and effective pressure, N. Budd's law is commonly used in ice flow models (e.g. Åkesson et al. (2021); Cornford et al. (2020)), but does not have an upper bound, and basal drag may reach arbitrarily high values. When we use Budd's law in our flow model, we do not get a very good initial fit to observations. During transient simulations using Budd friction we find smaller than expected velocities on grounded ice where the hydrology model predicts small effective pressure values and larger than expected velocities on floating ice where friction is zero but ice accelerates due to upstream changes in N. The Budd friction law produced a model that was extremely sensitive to changes in effective pressure on grounded ice, and required increasing the lower limit on effective pressure to 20% of overburden pressure to produce an acceleration of the correct magnitude near the grounding line. 10 km upstream of the grounding line modeled velocity was consistently too slow year round. An upper limit on τ_b/N, which prevents τ_b from becoming arbitrarily large when basal sliding increases (Iken, 1981), is included in the regularized coulomb friction law (Schoof, 2005; Gagliardini et al., 2007). We obtain a significantly better match with the observations when using a regularized coulomb friction compared to using Budd's law.

Regularized coulomb friction law:

$$\boldsymbol{\tau}_b = -\frac{C_S^2 \left|\boldsymbol{v}_b\right|^{m-1} \boldsymbol{v}_b}{\left(1 + \left|\boldsymbol{v}_b\right| \left(\frac{C_S^2}{C_{\max} N}\right)^{\frac{1}{m}}\right)^{m}}, \tag{A.1}$$

where $\boldsymbol{\tau}_b$ is basal shear stress, C_S is a friction parameter, $\boldsymbol{v}_b$ is the basal velocity, $C_{\max}$ is an upper limit on $\boldsymbol{\tau}_b/N$ known as Iken's bound, and $m = 1/n$ where $n = 3$ is the Glen's flow law exponent. We take $C_{\max} = 0.8$ everywhere in the ice flow domain.

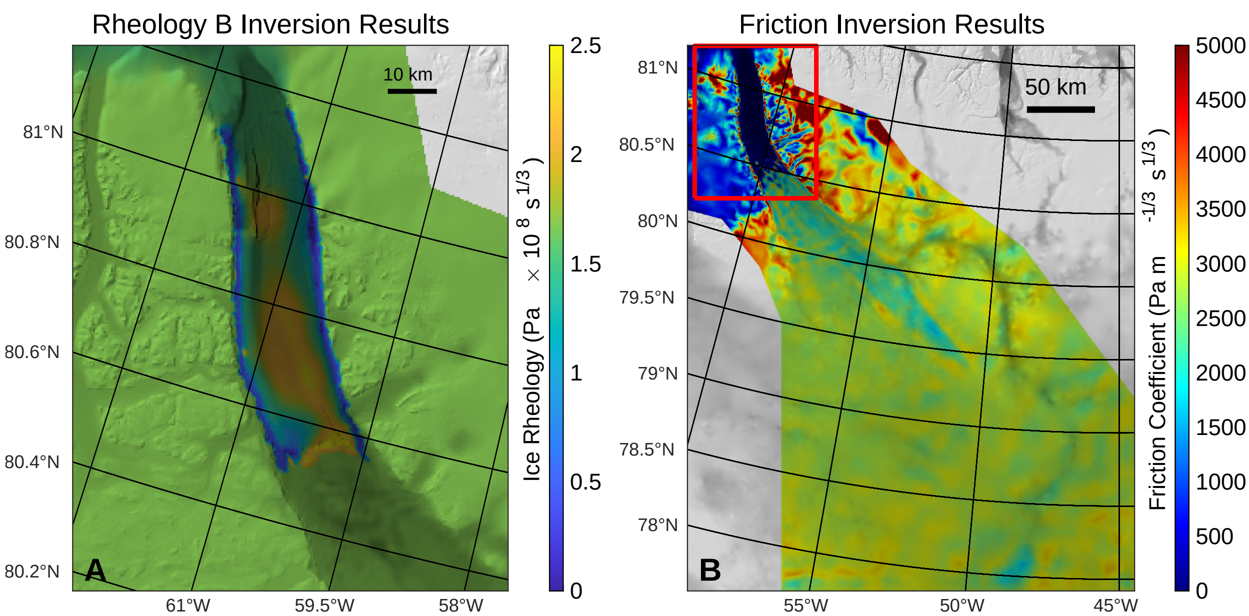

Figure A.7: (A) Ice rheology factor (B) and (B) basal friction coefficient calculated in a double inversion. Rheology is held constant over grounded ice. Floating ice along the fjord side walls was isolated and had a smaller maximum viscosity imposed during the inversion which allowed a better fit to surface velocity observations. Friction coefficient results from the double inversion. A regularized coulomb friction law was used with winter effective pressure from GlaDS during the inversion. A lower limit of 6% ice overburden pressure was imposed on effective pressure.

A.3 Results

The pattern of effective pressure mirrors that of integrated meltwater runoff (see Figure 3 in the main text). When runoff increases, effective pressure decreases across the hydrology model domain. Spikes in runoff are reflected in the modeled effective pressure. Changes in glacier speed in turn mirror the pattern in effective pressure (Figure 3C). Results from the hydrology model simulation are used to create daily effective pressure maps spanning the ice flow model domain, which force the ice flow simulation.

A.3.1 Effective pressure limit

Average daily values of the GlaDS output are used where the hydrology model domain overlaps the ice flow model domain. Outside of the hydrology model domain we calculate effective pressure as $N = \rho_i g H + \rho_w g z$ for grounded ice where $z < 0$, corresponding to regions where the bed is below sea-level, and we set $N = 0$ for floating ice where we assume hydrostatic equilibrium and zero basal friction. When $z > 0$, we approximate effective pressure as ice overburden pressure, $H = \rho_i g H$. We set a lower limit on N, where $N \geq 0.06\rho_i g H$. Figure A.8 shows the timing and spatial extent of the effective pressure limit implementation. We came to this value by doing a sensitivity test on a range of different values (Figure A.9). Changing the limit on effective pressure altered the magnitude of ice velocity, but did not significantly change the timing at which seasonal acceleration is initiated or how long it lasted. Baseline velocity also remained relatively consistent regardless of the choice of limit. We therefore chose the effective pressure limit to best match the magnitude of acceleration seen in our observations. Figure A.9 shows the velocity results at the grounding line for varying effective pressure limits ranging between 5 and 8% of ice overburden pressure. Results from this study use a limit of 6% of ice overburden pressure. When a lower limit of zero is used, we get velocities that are impossibly large.

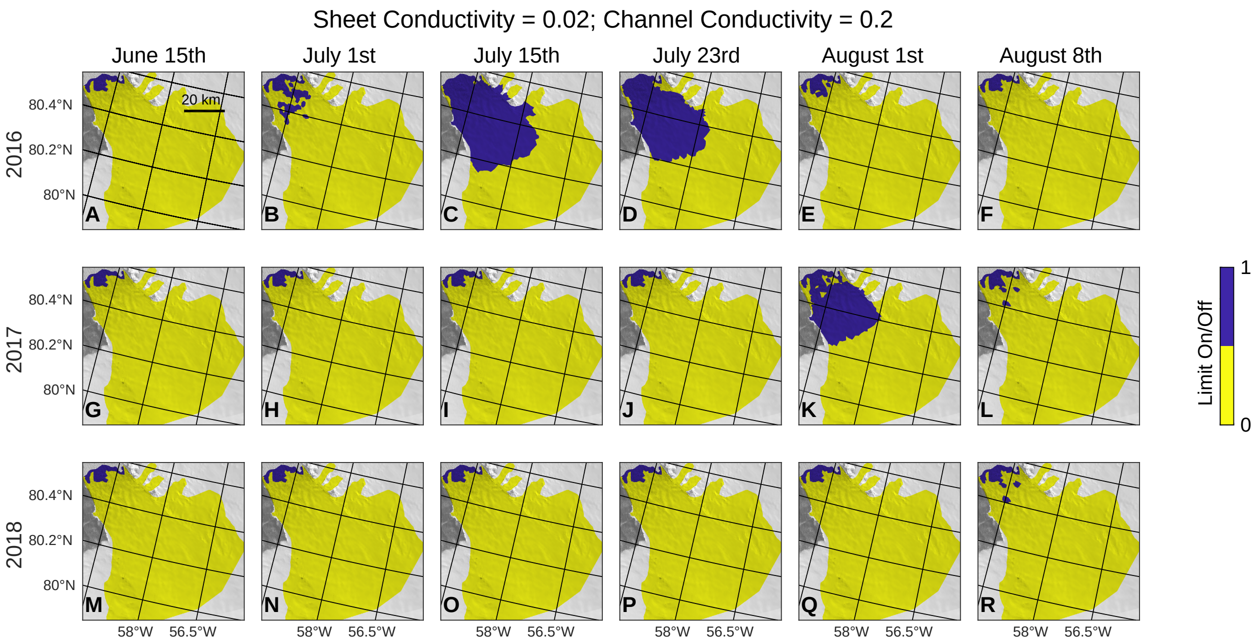

Figure A.8: (A-F) The region of the modeling domain over which the lower limit on effective pressure is implemented in 2016, (G-L) in 2017, (M-R) and in 2018. We use a geometry dependent, spatially variable limit of $N_{lim} = 0.06 \times P_{ice}$, where P_{ice} is the ice overburden pressure. In 2016, there are 34.83 days where at least one additional node in the hydrology model domain where N_{lim} is used, as compared to winter steady state where N_{lim} is only on near the grounding line. In 2017, this drops to 19.42 days, and in 2018 it is further reduced to 4.75 days. See Table 3 for comparison to additional GlaDS simulations.

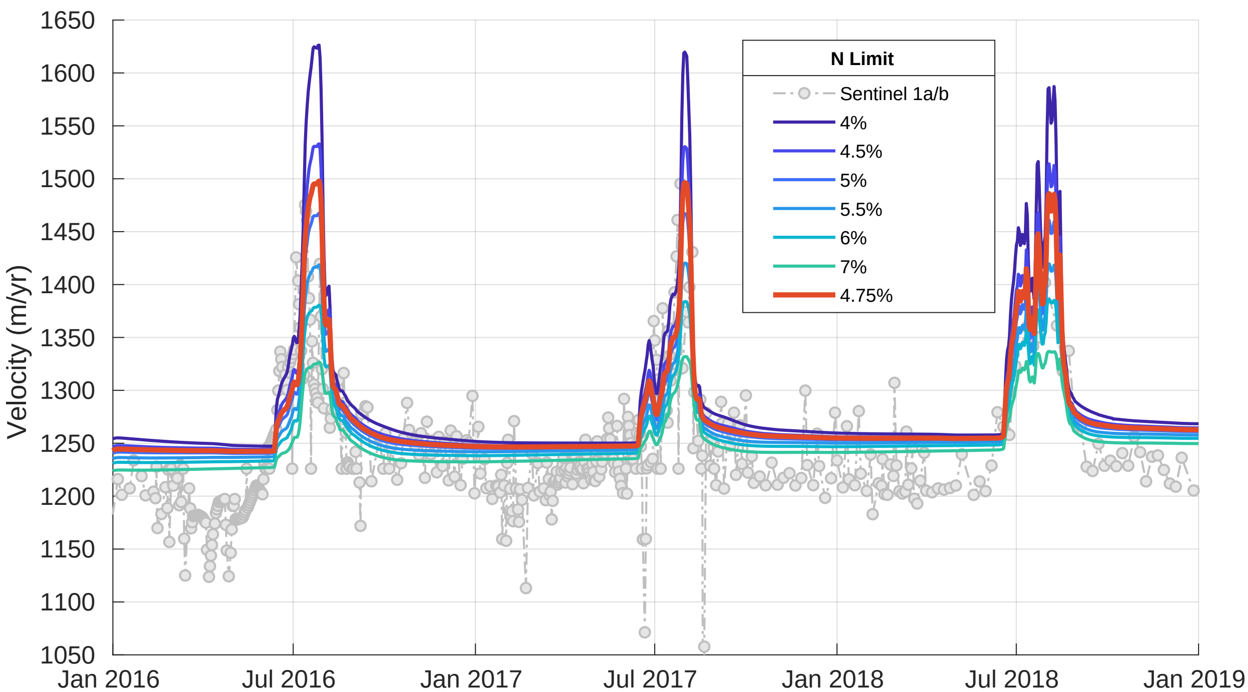

Figure A.9: Modeled ice velocity at the grounding line calculated with various different lower limits set on effective pressure. Effective pressure limits are defined as a percentage of ice overburden pressure. For this work, we chose to use a limit of 6% overburden as that yielded a seasonal acceleration which matched observations best in terms of magnitude.

A.3.2 Spatial velocity results

We find a good fit between modeled velocity to observations over a large region of the ice flow model domain. In the main text of this work we compare our results to observations at a point just upstream of the grounding line (Lat: 80°33'12.96", Lon: -59°52'36.48") and along a central flow line. We chose this point because it is grounded and it clearly shows a strong seasonal signal in our observations.

Observations show a large seasonal accelerations on floating ice within 20 km of the grounding line, about half of the Petermann's ice shelf. There are large swings (>300 m/yr) in velocity closer to the ice front, comparable to the magnitude of seasonal acceleration observed elsewhere on the ice shelf. However, these oscillations occur year round. This seems to indicate that near the ice front, there are other forcings which dominate that have not been incorporated into our hydrology forced ice flow model setup. The signal is visible on grounded ice within ~10 km of the grounding line in 2018 and nearly 20 km in 2016-2017, when the total runoff was larger than that of 2018. The seasonal signal damps in data with decreasing surface velocity and increased distance to the grounding line.

Our model matches observations on floating ice well within ~15 km of the grounding line (See A.10). Further downstream of this point our model oscillations in ice velocity become so large that any seasonal signal would be overwritten. Our model predicts a strong seasonal acceleration for the full ice shelf (see Movie S2) with no shorter time scale oscillations. On grounded ice, our baseline modeled velocity decreases and the magnitude of seasonal acceleration damps with distance to the grounding line (Figure A.11), both of which are observed trends in our data. However, our model continues to predict a small, but distinct, seasonal signal much farther upstream than is visible in observations. Even 45 km upstream of the grounding line the model predicts a 50 m/yr speedup in 2016 (465 m/yr baseline speed), which is not seen in observations.

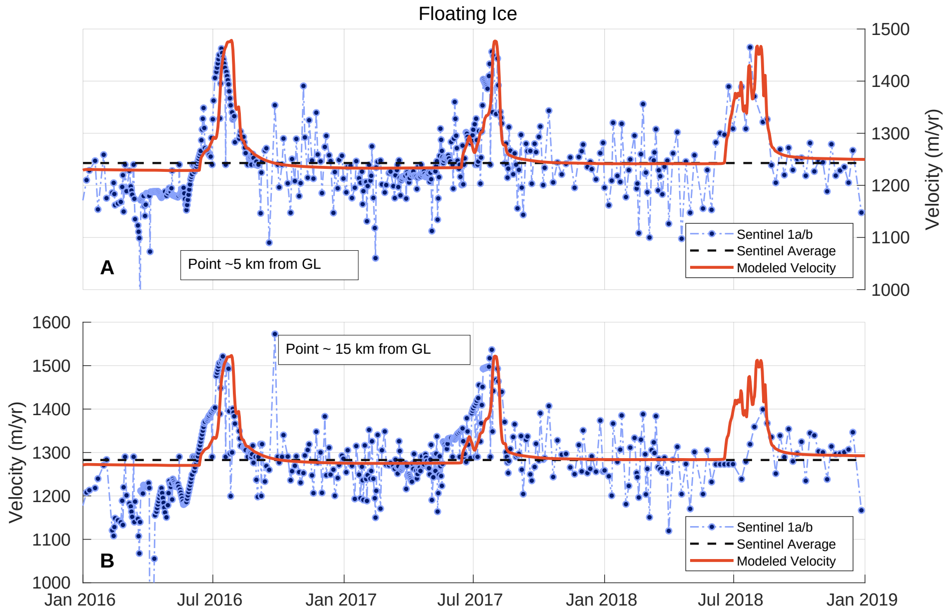

Figure A.10: (A) Point comparisons between modeled velocity results and observations on Petermann's ice shelf 5 km (Lat: 80°35'57.04", Lon: -60°2'28.68"), (B) 10 km (Lat: 80°37'18.84", Long: -60°15'40.32"), and (C) 15 km (Lat: 80°38'57.84", Lon: -60°25'59.88) downstream from the grounding line.

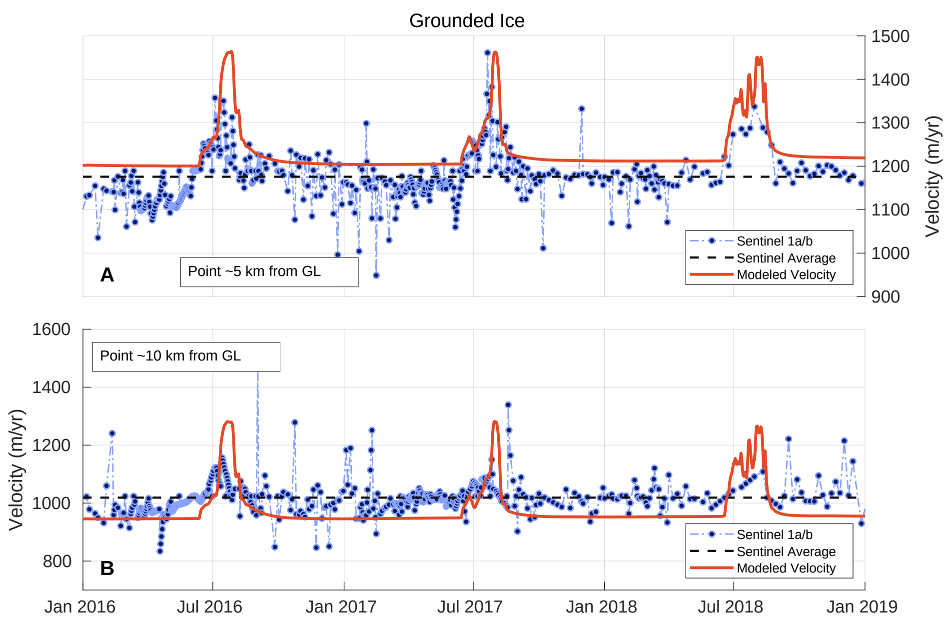

Figure A.11: (A) Point comparisons between modeled velocity and observations on grounded ice 5 km (Lat: 80°32'0.24", Lon: -59°38'49.2"), (B) 10 km(Lat: 80°29'48.84", Lon: -59°24'58.68"), and (C) 15 km (Lat: 80°27'59.04", Lon: -59°15'50.76") upstream of the grounding line.

A.4 GlaDS Sensitivity Tests

A.4.1 Sheet and channel conductivities

We test a range of different values for two GlaDS parameters to tune the hydrology model: sheet conductivity ($m^{7/2}kg^{-1/2}$) and channel conductivity ($m^{3/2}kg^{-1/2}$). Sheet conductivity controls how quickly water is able to move through the model domain via inefficient distributed flow through the hydraulic sheet, and channel conductivity controls how quickly subglacial channels are able to grow and connect to form an efficient drainage network. The default values for these parameters are 0.001 $m^{7/2}kg^{-1/2}$ for sheet conductivity and 0.05 $m^{3/2}kg^{-1/2}$ for channel conductivity. We ran GlaDS using the default parameters, and the results from that simulation can be seen in A.12. Water is not able to quickly drain the system via sheet flow or through the development of a channel network, and as a result effective pressure is negative for the bulk of the melt season. This requires the activation of the effective pressure limit over a large portion of the model domain, and for most of the melt season all three years (Figure A.13A-R). The resulting seasonal acceleration can be seen in Figure A.13S.

Increasing both conductivity parameters decreases the magnitude of the response to meltwater runoff entering the system (Figures A.14-A.16). Hydraulic potential increases in response to the injection of meltwater to the bed as water pressure increases, which decreases effective pressure. When sheet conductivity is small (Figure A.13), water does not quickly leave the system and water pressure continues to increase while more meltwater enters the system as the melt season progresses. The result of this is that hydraulic potential spikes and remains high for the duration of the melt season causing large negative values to be obtained for effective pressure. When sheet conductivity is larger (Figures A.14 & A.15), water is able to quickly drain the system, and we do not see as large of an increase in hydraulic potential. This prevents effective pressure from reaching such large negative values. We see a similar relationship with channel conductivity. When channel conductivity is small (Figures A.13 & A.15), the channel network is not able to quickly develop and efficiently remove water from the system. When we increased the channel conductivity (Figure A.15 vs. A.16), effective pressure is larger, and we can see that the the area over which the effective pressure limit is needed is smaller and the magnitude of modeled acceleration decreases for all three years. The number of days that the limit is used is also reduced by increasing channel conductivity (Table S3). In the low melt year, 2018, effective pressure remains positive for the full melt season in all of the simulations reported in Table S3 except for the one which uses default parameter values for both sheet and channel conductivity.

Table S3 lists the variation in the length of time that the effective pressure limit is used and the maximum percent of model nodes that it is applied to for various model simulations from our analysis of the parameter space. Each simulation contains a region close to the grounding line where the effective pressure limit is used year round due to modeled water pressures continuously remaining around 98% of overburden. Adjusting the effective pressure in this region has a minimal impact on results. We therefore exclude it when counting the length of time each year that the model uses the limit. However, if even one additional node has the limit activated for at any point during the year, we count that as a day when the limit is on. Our hydrology mesh is not uniform, and element size varies substantially based on the gradient in ice surface velocity and proximity to the grounding line. In regions where velocity changes rapidly and with reduced distance to the grounding line we have smaller element sizes, and thus more nodes per unit area. As a result, the percentage of nodes should not be taken to be equivalent to percentage of model area. We include this value for comparative purposes, so that the relative portion of model domain which uses the effective pressure limit can be compared between simulations.

The shape of the summer velocity increase matches the runoff time series well, but the magnitudes do not match for all three years (Figure 3C in the main document). Runoff was highest in 2016 and lowest in 2018, with 2017 falling in between (Figure 3A, Table S2). We see a sizeable change in the magnitude of the modeled ice acceleration that follows the same pattern of runoff. However, in our model the variation in peak summer velocity is much larger than what is observed in satellite data, where the peak velocity in 2018 is 100 m/yr less than the previous two years which have a maximum observed velocity of 1,500 m/yr. In our model results, peak summer speed is 1520 m/yr in 2016, 1480 m/yr in 2017, and 1,300 m/yr in 2018. Most of our simulations predict a dependence of peak summer velocity on magnitude of runoff (ex: Figure A.14), which suggests that there may be a physical connection between peak runoff and magnitude of acceleration for Petermann. However, some of the simulations in our sensitivity tests show a much smaller variation in peak speed that is more aligned with the magnitude of speedup seen in observations (Figures A.15 & A.16). The simulations which match the magnitude of acceleration best for all three years are also those which use a smaller value for sheet conductivity, and consequentially require the lower limit on effective pressure to take effect for a longer period of time and over a larger portion of the model domain (See Table S3). These runs are able to better match peak speed for all three years because effective pressure is reduced over a large portion of the domain very quickly with the injection of runoff to the bed. However, without water easily flushing out of the system, effective pressure values continue to decrease to physically unrealistic values over an extensive region as the melt season progresses, necessitating the application of an effective pressure limit for the bulk of the melt season. Without the use of the limit, velocities reach unrealistically large values (Figure A.9). In simulations where sheet conductivity is larger (Figure A.14), allowing for water to move through the subglacial hydrologic system rapidly, the application of the effective pressure limit is reduced both in terms of length of time and spatial extent, but maximum speed in the low melt year, 2018, is under-predicted (Figure A.14S). This is a limitation of our model, and requires further exploration to explain that is beyond the scope of this work.

Table A.3: Length of time (days) and the percentage of hydrology model nodes (% of total) which have the lower limit on effective pressure (6% of ice overburden pressure) turned on for GlaDS simulations using a range of parameter values for sheet conductivity ($m^{7/2}kg^{-1/2}$) and channel conductivity ($m^{3/2}kg^{-1/2}$).

Conductivity		2016		2017		2018	
Sheet	Channel	Days	% of Nodes	Days	% of Nodes	Days	% of Nodes
Default parameter values							
0.001	0.05	85.75	63.18	83.17	61.86	73.85	58.07
Different sheet and channel conductivity							
Increasing sheet conductivity							
0.005	0.2	42.75	61.06	49.17	52.04	53.08	39.86
0.025	0.2	32.08	42.45	10.17	21.37	0	0
0.04	0.2	22.42	25.67	4.25	0.52	0	0
Increasing channel conductivity							
0.015	0.05	40.5	55.54	39.67	47.04	40.08	25.45
0.015	0.1	38.41	54.8	36.42	45.38	30.67	19.18
0.015	0.2	39.17	53.88	31.17	39.98	25.25	9.94
Different moulin configurations							
36 moulins							
0.02	0.2	34.83	48.54	19.42	31.02	4.75	0.4
15 moulins							
0.02	0.2	34.25	43.42	11.85	22.29	2.25	0.11
0 moulins							
0.02	0.2	33.91	56.92	11	16.94	0	0
Increased sliding velocity							
0.02	0.2	34.75	48.25	19	30.33	4.5	0.34

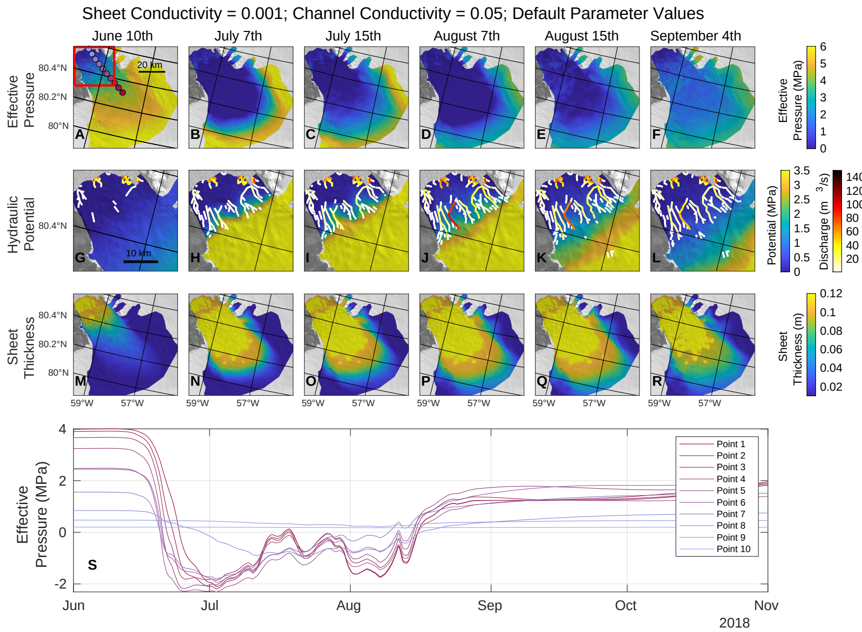

Figure A.12: Results from GlaDS simulation where we use the default parameter values. In this run sheet conductivity is 0.001 $m^{7/2}kg^{-1/2}$ and channel conductivity is 0.05 $m^{3/2}kg^{-1/2}$. Results from the ice flow model using these effective pressures are in A.13S.

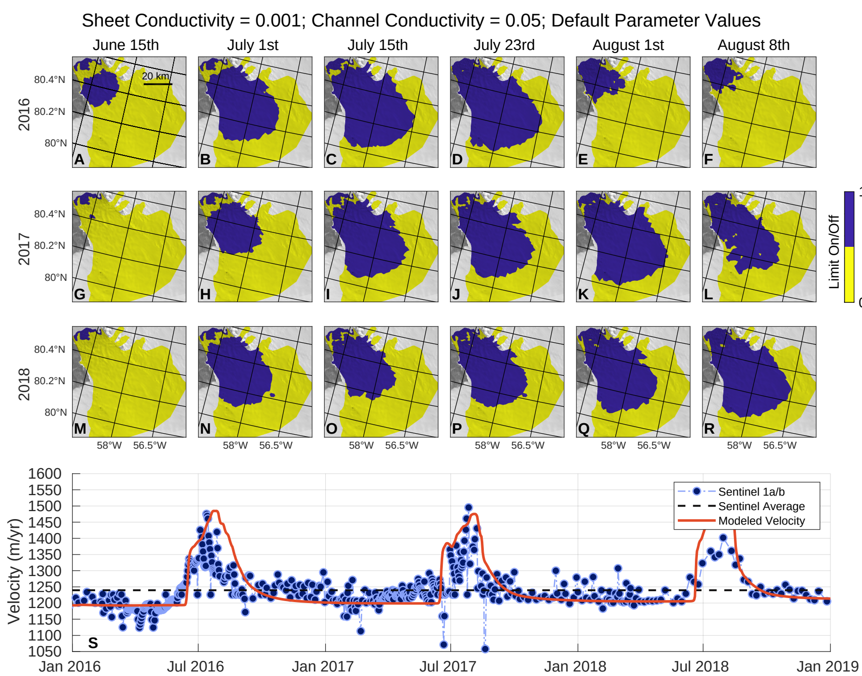

Figure A.13: (A-R) Regions where the lower limit on effective pressure of 6% of ice overburden pressure is applied during the ice flow simulation. Effective pressure calculated by GlaDS in these regions often have large negative values that are sustained for the bulk of the melt season. (S) Results from ice flow model using effective pressure from a GlaDS hydrology simulation using default parameter values. Sheet conductivity for this run is 0.001 $m^{7/2}kg^{-1/2}$ and channel conductivity is 0.05 $m^{3/2}kg^{-1/2}$.

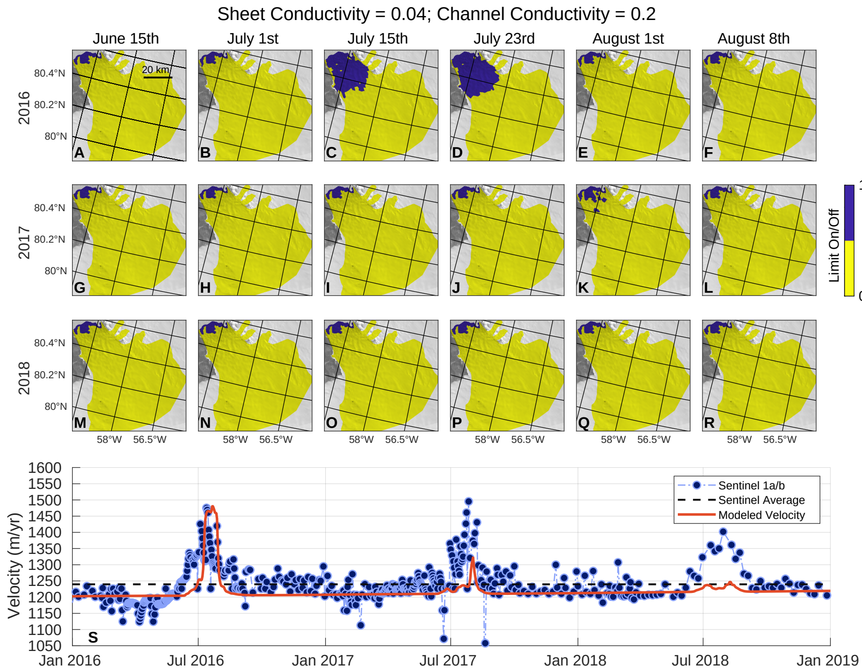

Figure A.14: (A-R) Regions where the lower limit on effective pressure of 6% of ice overburden pressure is applied during the ice flow simulation when sheet conductivity is 0.04 $m^{7/2}kg^{-1/2}$ and channel conductivity is 0.2 $m^{3/2}kg^{-1/2}$, and (S) modeled ice velocity results.

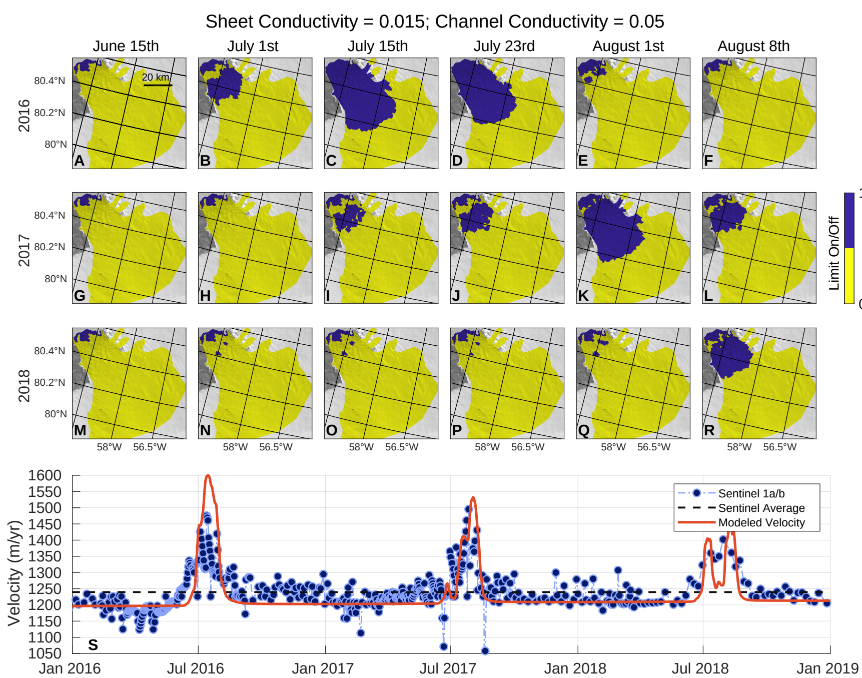

Figure A.15: (A-R) Regions where the lower limit on effective pressure is applied and (S) results from the ice flow model using effective pressure GlaDS results from a simulation that uses parameter values of 0.015 $m^{7/2}kg^{-1/2}$ for sheet conductivity and 0.05 $m^{3/2}kg^{-1/2}$ for channel conductivity.

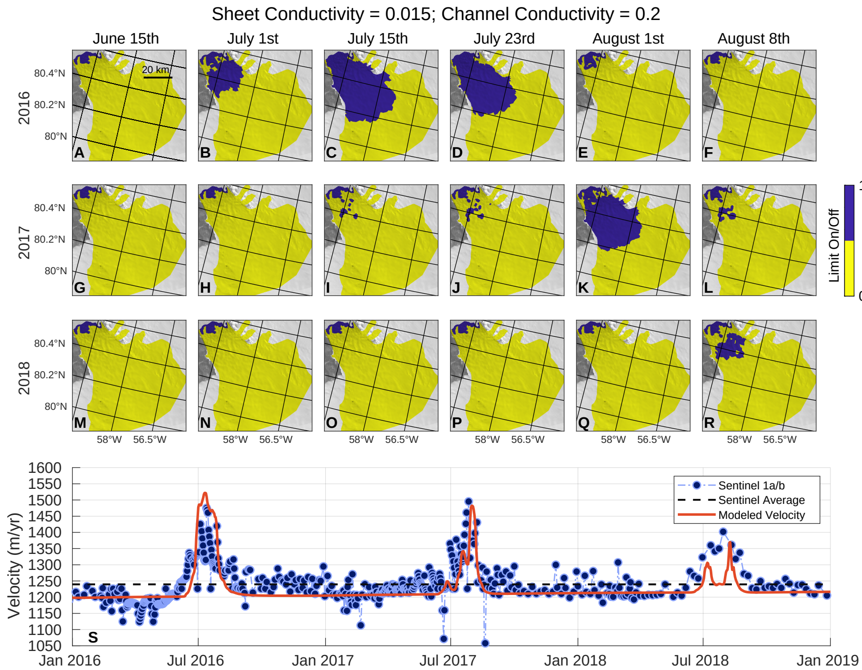

Figure A.16: (A-R) Regions where the lower limit on effective pressure is applied, and (S) results from the ice flow model using effective pressure GlaDS results from a simulation that uses parameter values of 0.015 $m^{7/2}kg^{-1/2}$ for sheet conductivity and 0.2 $m^{3/2}kg^{-1/2}$ for channel conductivity.

A.4.2 Enhanced basal sliding

We cannot currently test the impact of the negative feedback loop between ice velocity and effective pressure due to the one way coupling between subglacial hydrology and ice dynamics in our model. This is a limitation discussed in the main document. However, we wanted to examine if increased sliding velocity might help to reduce the dependency on the lower limit on effective pressure. To that end, we have conducted a hydrology simulation where we uniformly increase the sliding velocity obtained from ISMIP6 data (Figure A.3A) by 15%, which corresponds to the peak summertime velocity observed in our data. This is likely to produce a more exaggerated change than would actually be obtained by using a fully coupled model configuration, as we would not expect to see sliding velocity increase across the full hydrology model domain from changes in effective pressure. Even so, increasing the sliding velocity did not produce substantially different results from other simulations using

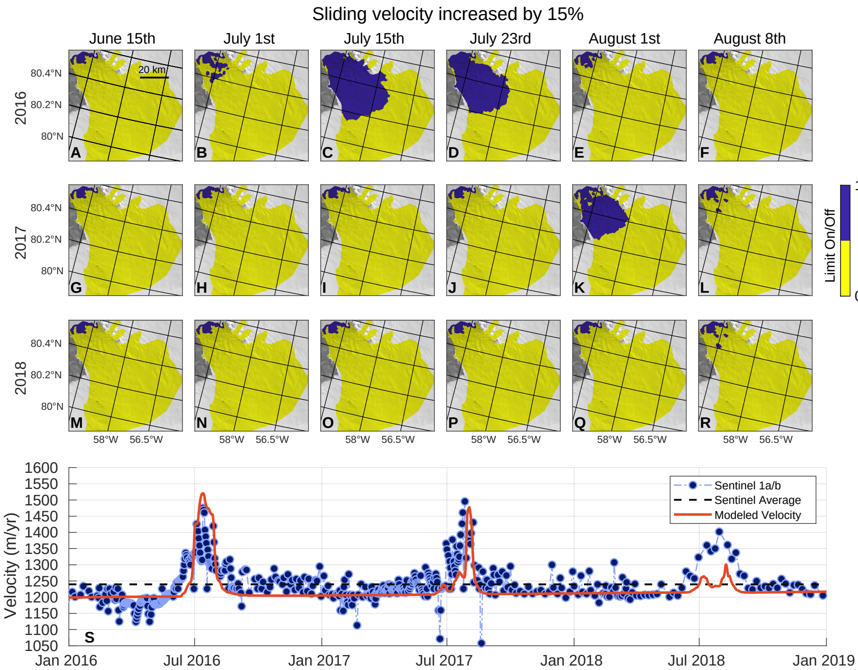

Figure A.17: (A-R) Regions where the lower limit on effective pressure of 6% of ice overburden pressure is applied during the ice flow simulation, and (S) modeled ice velocity results. Effective pressure used to obtain these results was calculated from a GlaDS simulation which used 0.02 $m^{7/2}kg^{-1/2}$ for sheet conductivity, 0.2 $m^{3/2}kg^{-1/2}$ for channel conductivity, and had sliding velocity uniformly increased by 15% compared to ISMIP6 data (A.3A.

the same hydrology parameter values. Results from this simulation can be seen in Figure A.17. It does not substantially diminish the use of the effective pressure limit (See Table S3), although we do see a slight decrease in the number of days the limit is used in each year (by less than one day) and a slight decrease in the number of nodes the limit is applied to (by less than one percent).

A.4.3 Methods of meltwater injection to the bed

We ran additional simulations to examine the sensitivity of our model to the method by which meltwater runoff is introduced using three different methods to inject runoff to the bed: two simulations that use moulins to transport integrated melt to the bed as point sources, and one where melt is sent directly to the bed with the same spatial distribution as the surface melt. We use the 36 moulin configuration in the main document, and in all simulations unless specified otherwise. For the 15 moulin configuration, locations are not in the same positions as the configuration discussed in the main text, they do occupy the same sub-region of the hydrology domain. In the third simulation, melt is injected directly to bed without being routed through moulins. We find that although there are some differences in the details of the GlaDS results, the overall pattern is consistent across all three simulations. When effective pressure results are then used to force the ice flow model, the computed velocities are very similar for all three simulations.

All simulations required the use of lower limit on effective pressure. Figures A.18S and A.19S show the time-series at a Point 10 (Lat: 80°33'12.96", Lon: -59°52'36.48") when the limit is set to 6% of over burden pressure, which was the value found to produce the best match to observations when using 36 moulins to inject runoff to the bed. Both of these simulations use a value of 0.02 $m^{7/2}kg^{-1/2}$ for sheet conductivity and 0.2 $m^{3/2}kg^{-1/2}$ for channel conductivity. Reducing the number of moulins used had the impact of lowering the peak summer velocity in the low melt year, 2018. When meltwater runoff is sent directly to the bed without the use of any moulins we see a summer speed up of only about 50 m/yr as opposed to 100 m/yr when we use 36 moulins to transport runoff to the bed (Figure A.19S). In this simulation, the effective pressure limit is never utilized in 2018, except for the region in the immediate vicinity of the grounding line. However, in 2016, the effective pressure limit is still required for 34 days and over 57% of nodes. When we use 36 moulins, the limit is also needed for 34 days in 2016 and is applied to a maximum of 48.5% of nodes. Reducing the number of moulins did not have the same impact on the reliance of the effective pressure limit from one year to the next. We chose to continue using the 36 moulin configuration because it produced the largest acceleration in 2018, and did not significantly increase the use of the effective pressure limit.

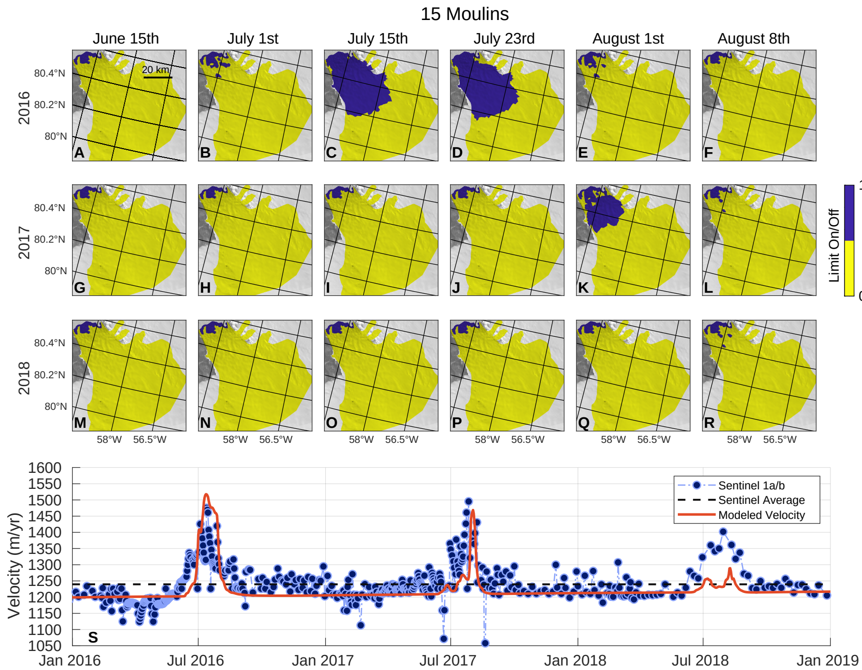

Figure A.18: (A-R) Regions where the lower limit on effective pressure is applied during the ice flow simulation, and (S) the modeled ice velocity results. The GlaDS simulation used 15 moulins to transport melt water runoff to the bed, and parameter values of 0.02 $m^{7/2}kg^{-1/2}$ for sheet conductivity and 0.2 $m^{3/2}kg^{-1/2}$ for channel conductivity.

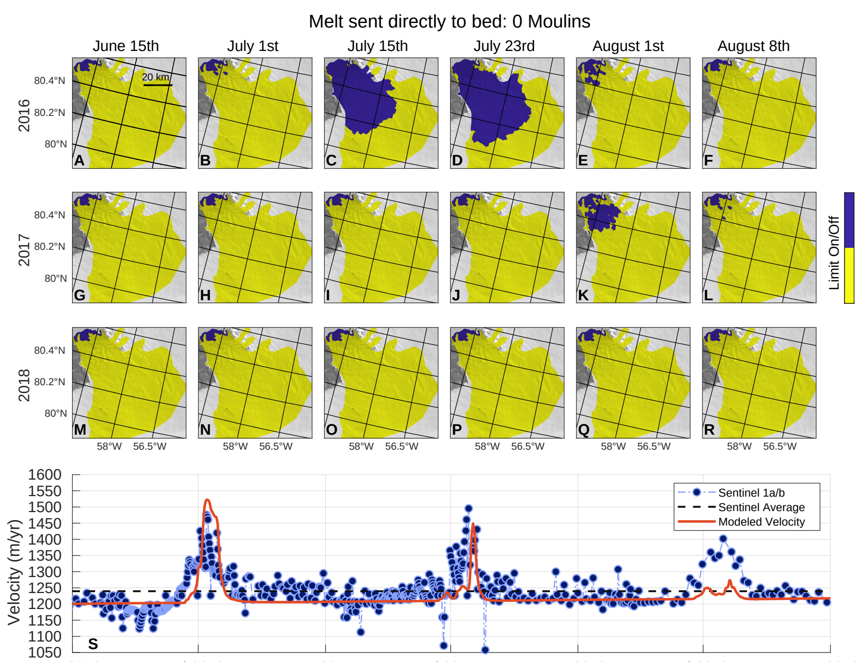

Figure A.19: (A-R) Regions where the lower limit on effective pressure is applied during the ice flow simulation, and (S) the modeled ice velocity results. The GlaDS simulation had meltwater runoff sent directly to the bed, and used parameter values of 0.02 $m^{7/2}kg^{-1/2}$ for sheet conductivity and 0.2 $m^{3/2}kg^{-1/2}$ for channel conductivity.

A.5 Other possible explanations for seasonal ice acceleration

In addition to running simulations to test the sensitivity of GlaDS to the choices of parameter values and the method by which meltwater runoff is transported to the bed, we also looked at two other physical mechanisms that might produce seasonality in ice velocity other than subglacial hydrology. We set up simulations in the ice flow model to see if buttressing or enhanced basal melt under the ice shelf could produce a seasonal speedup close to what we see in the satellite data. To examine buttressing, we take a time-series of observed ice velocity on the ice shelf from the satellite data and use it to constrain the velocity at the ice front. This forces the modeled velocity to match observations along the ice front so that velocity at the front has an imposed seasonal cycle. In this simulation, we do not use evolving effective pressure from GlaDS, but we do still use the same long term winter average of GlaDS effective pressure in the friction inversion so that the initial state of the ice flow model is the same in this simulation as it is in the simulation presented in our main results. We run the model for 12 years using a 1 day time-step, which is consistent with all previous simulations. Modeled velocity at the grounding line from this simulation can be seen in Figure A.20. We do see a seasonal cycle of velocity in the ice within roughly 15 km of the ice front, but the signal does not propagate through the full ice shelf, and it damps quickly with distance from the ice front. Only small undulations can be seen near the grounding line, as opposed to the 15% increase in velocity that is seen in the data. In the portion of the ice shelf where we do see seasonal acceleration in this model simulation, we actually do not see an obvious seasonality in observations. There are large swings in ice velocity close to the ice front in the data, but they occur year round, and do not seem to change in duration or magnitude in the summer. As such, it seems unlikely that buttressing from seasonal sea-ice alone can produce the seasonal patterns in velocity that are observed.

To examine seasonal basal melt under the ice shelf, we use the melt rates published by Cai et al. (2017). The authors report 3 months of enhanced melt rates as compared to the winter baseline melt rate of 27 m/yr. In June the melt rate under Petermann's ice shelf increases to 38 m/yr, then in July it reaches its peak summer melt rate of 85 m/yr, and remains relatively elevated in August at 75 m/yr. Since the reported values are monthly averages, we apply them in our model at the midpoint of the month, with the winter melt rate of 27 m/yr applied from September to May each year. ISSM linearly interpolates at each time-step between the assigned values, so the enhanced basal melt is applied for 3 months in total, but is above 50 m/yr for roughly 9 weeks. We set the deep water elevation at -250 m, so that these enhanced melt rates are applied to all floating ice that is deeper than 250 m below sea level. The shallow water melt rate is set to 10 m/yr and is constant in time. ISSM linearly interpolates with depth between the deep water melt rate and the shallow water melt rate. We ran this simulation for 12 years with a 1 day time-step, and compare the last 3 years of the simulation to our observations. Results from this simulation can be seen in Figure A.21. Imposing a seasonal cycle in the basal melt rates did not produce any seasonality in velocity, although we do see a small sustained speedup between years that was not present in other simulations.

Neither of buttressing nor enhanced basal melt under the ice shelf were able to produce a visible seasonal cycle near the grounding line, where the acceleration is the most prominent in our observations. We feel that this is further evidence that the observed seasonality is likely from seasonal meltwater runoff changing the basal friction. Of the three physical mechanisms, hydrology was the only the only one which caused a substantial speedup in the summer over the general region where we observe seasonal acceleration on Petermann. When we use effective pressure calculated by GlaDS to force the ice flow model, we also get a seasonal signal that is generally the right shape and occurs at the correct time as compared to observations. While the model is not a prefect representation of reality for Petermann, we feel that it does a good job of showing that subglacial hydrology is capable of producing

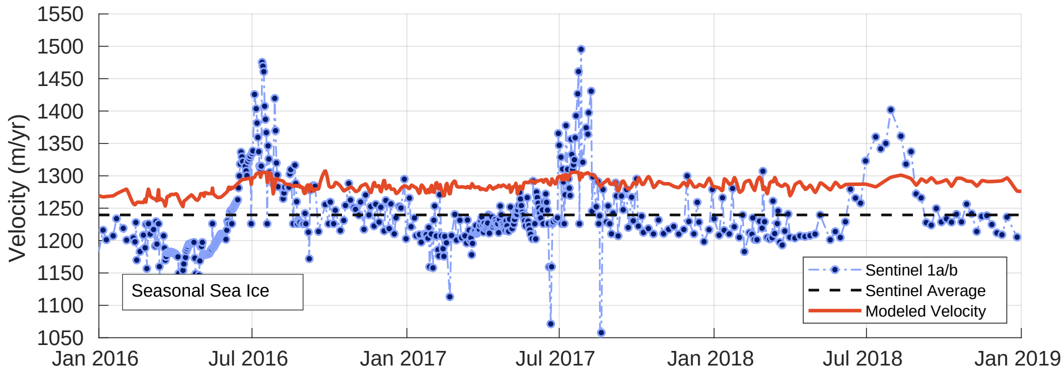

Figure A.20: Ice flow model velocity results when we fix the ice front velocity using satellite observations to represent seasonal forcing from sea ice buttressing.

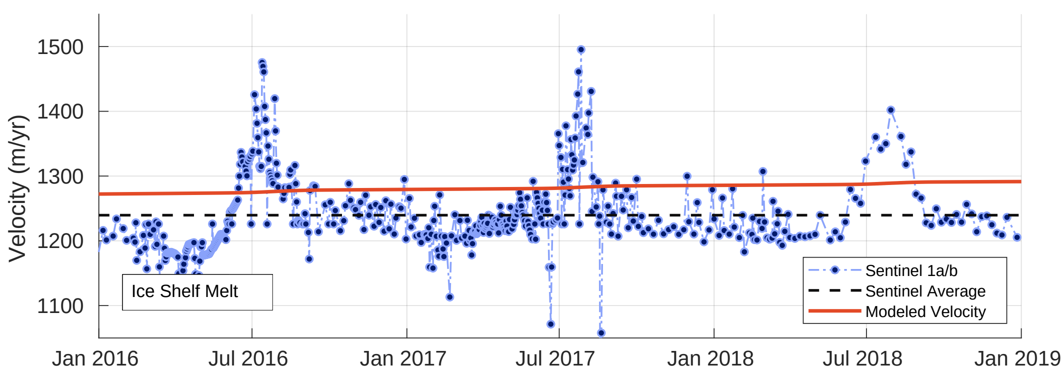

Figure A.21: Ice flow model velocity results when we apply seasonal basal melt to the ice shelf from enhanced thermal ocean forcing.

the type of seasonality observed as a proof of concept.

Appendix B

Supplemental Information: Modeled sea water intrusion in the observed grounding zone of Petermann Glacier causes extensive retreat

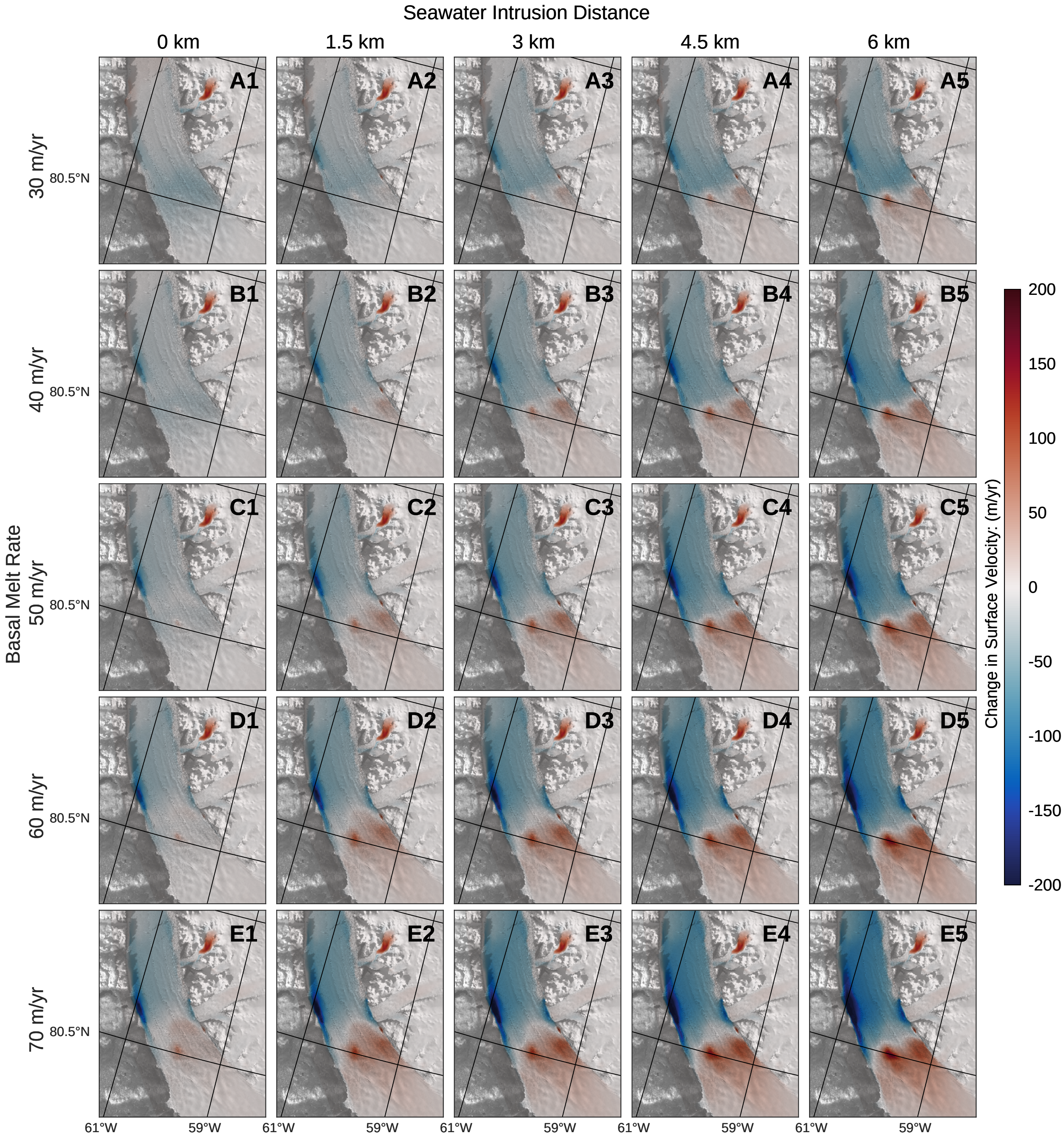

Figure B.1: Change in ice surface velocity from 2010 to 2022 for model simulations with various maximum basal melt rates and a range of seawater intrusion distances. Positive values are associated with ice acceleration (red shading) over the course of the simulation, and negative values are associated with a reduction in speed (blue shading).

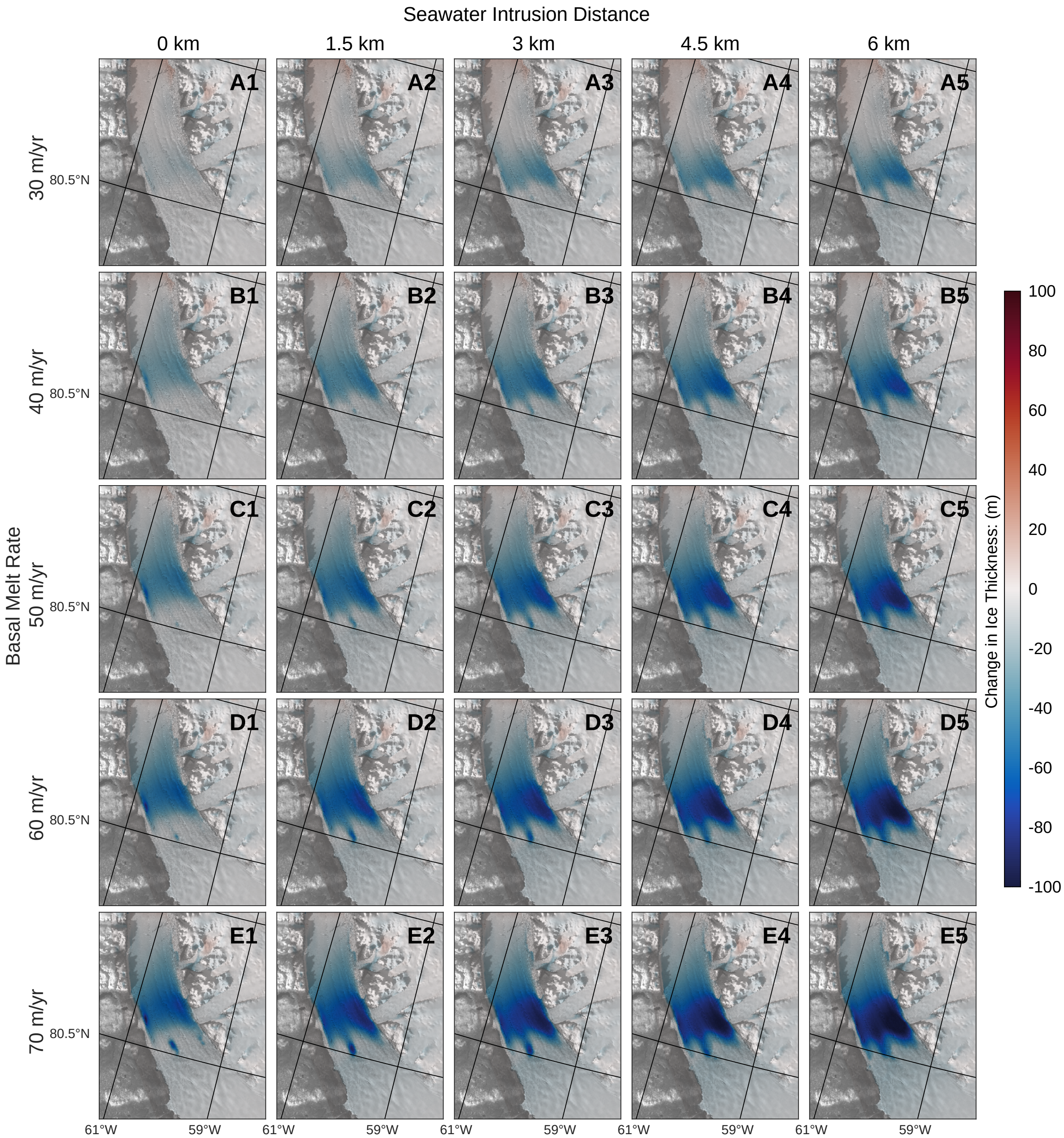

Figure B.2: Change in ice thickness from 2010 to 2021, corresponding to data availability, for model simulations with various maximum basal melt rates and a range of seawater intrusion distances. Positive values indicate increased ice thickness (red shading) towards the end of model simulations, and negative values indicate thinning (blue shading).

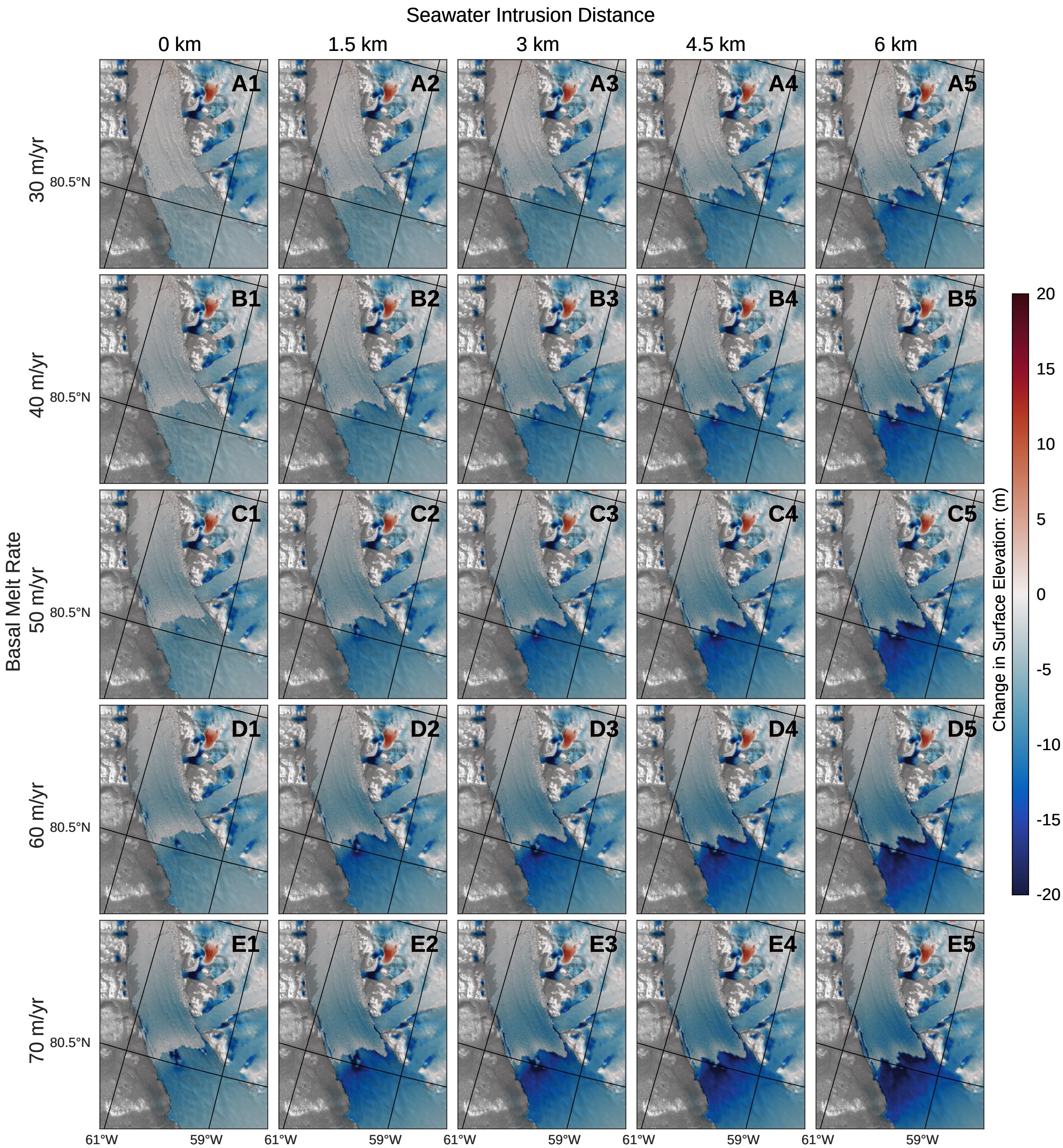

Figure B.3: Change in ice surface elevation from 2010 to 2021, for model simulations with various maximum basal melt rates and a range of seawater intrusion distances. Positive values indicate higher ice surfaces towards the end of the model simulation (red shading), and negative values indicate a lowering of the ice surface (blue shading). Note that SMB model forcing is equivalent across all simulations.